The Key Laboratory of Weak Light Nonlinear Photonics,
Ministry of Education

Annual Report 2020

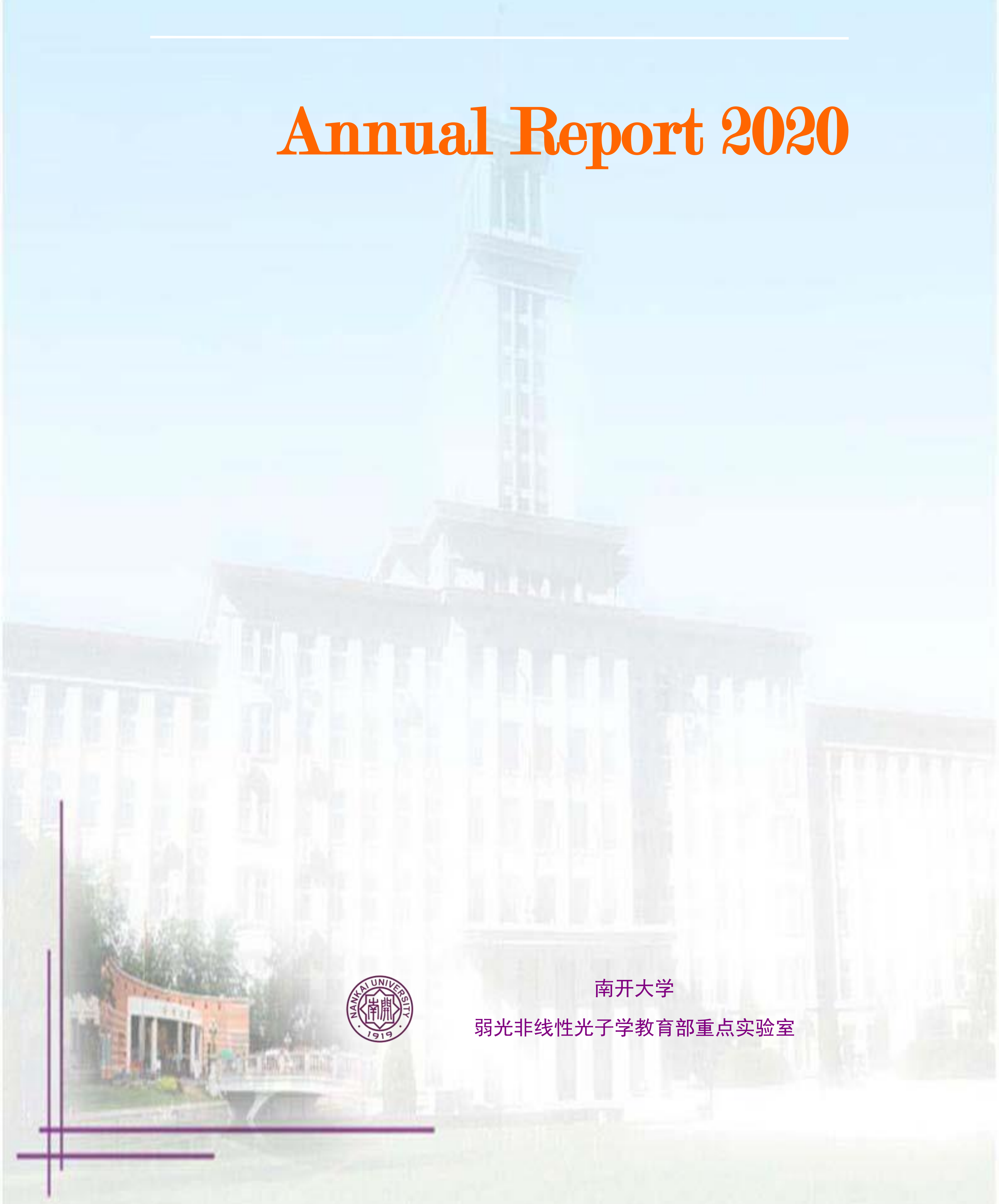

南开大学

弱光非线性光子学教育部重点实验室

目　录/Contents

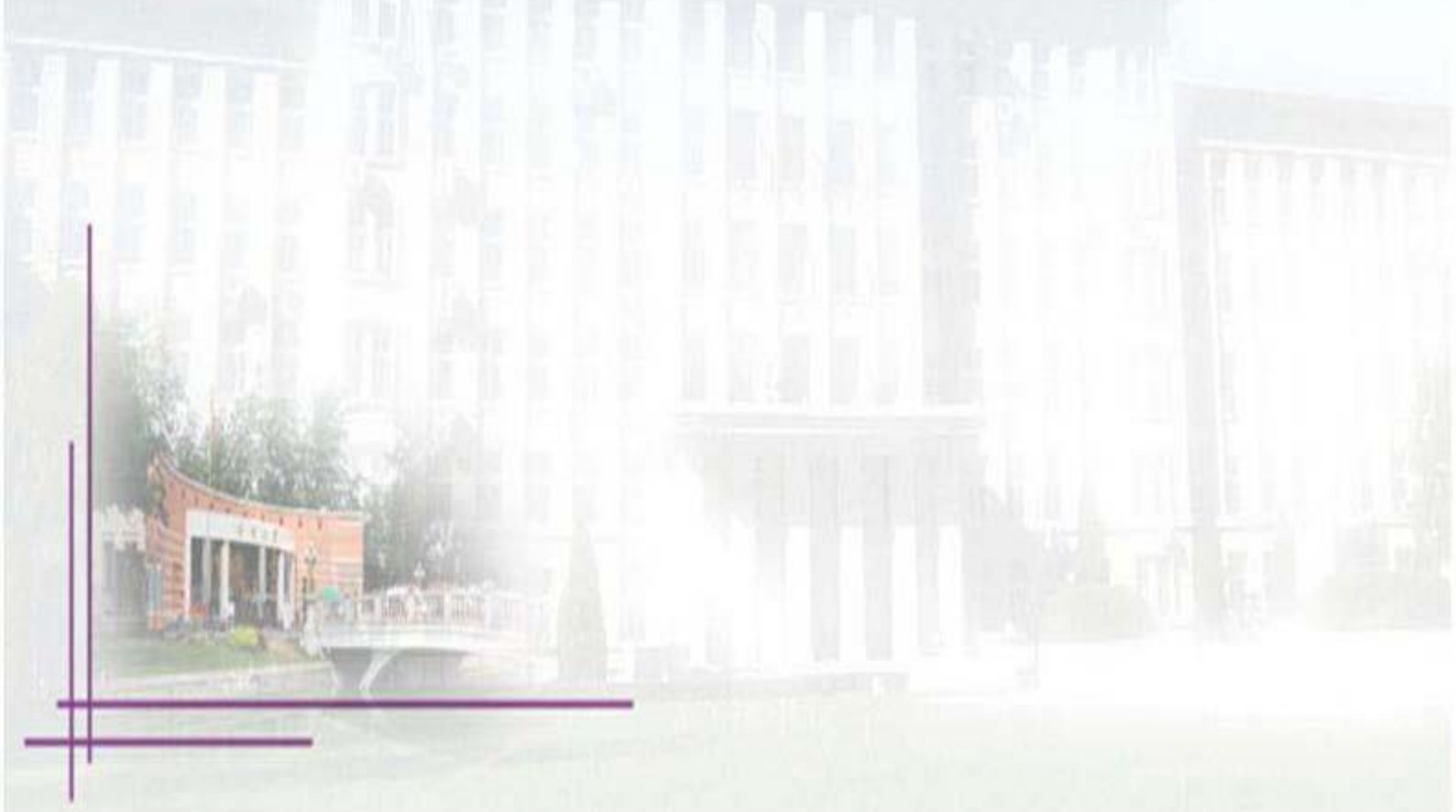

人员结构/Organization

实验室主任/Director

张国权 教 授

实验室副主任/Deputy Directors

刘智波 教 授

李勇男 教 授

学术秘书/Academical Secretary

禹宣伊 副教授

研究方向负责人/Research Group Leaders

弱光非线性及量子相干光学	许京军 教 授
非线性物理与光子技术	田建国 教 授
非线性光子学材料及先进制备技术	孔勇发 教 授
光场调控及其应用	王慧田 教 授
光谱表征及传感技术	宋 峰 教 授

学术委员会/Academic Committee

主 任/Chairman

李树深 院 士 （中国科学院半导体研究所）

委 员/ Committee Members

薛其坤	院 士	（清华大学）
孙昌璞	院 士	（中国工程物理研究院北京计算科学研究中心）
龚旗煌	院 士	（北京大学）
陆 卫	研究员	（中国科学院上海技术物理研究所）
资 剑	教 授	（复旦大学）
申德振	研究员	（中国科学院长春光学精密机械与物理研究所）
曾和平	教 授	（华东师范大学）
童利民	教 授	（浙江大学）
王雪华	教 授	（中山大学）
陈 峰	教 授	（山东大学）
田建国	教 授	（南开大学）
王慧田	教 授	（南开大学）
许京军	教 授	（南开大学）
张国权	教 授	（南开大学）

外籍学术顾问委员

Yuri Kivshar	院 士	澳大利亚国立大学
D. Kip	教 授	德国 Clausthal 工业大学
L. Hessenlink	教 授	美国斯坦福大学物理系
R. A. Rupp	教 授	奥地利维也纳大学实验物理所
T. Volk	教 授	俄罗斯国家晶体研究所
Y. Tomita	教 授	日本电气通信大学
K. A. Nelson	教 授	美国麻省理工学院

杰出人才/Intelligent Staff

教育部“长江奖励计划”特聘教授

许京军（1999） 王慧田（1999） 陈志刚（2006）

国家杰出青年基金获得者

许京军（1998） 田建国（2001） 王慧田（2003） 李宝会（2009）
陈树琪（2019） 周向锋（2020）

教育部“长江学者奖励计划”青年学者

陈树琪（2019）

国家优秀青年基金获得者

宋道红（2019） 胡毅（2020）

教育部“优秀青年教师资助计划”入选者

张国权（2002） 宋峰（2003）

教育部“跨世纪优秀人才培养计划”入选者

许京军（1998） 田建国（2000） 孙骞（2001） 孔勇发（2002）

教育部“新世纪优秀人才支持计划”入选者

张国权（2004） 宋峰（2004） 臧维平（2005） 李宝会（2005）
孙甲明（2007） 张心正（2008） 刘智波（2009） 陈璟（2009）
顾兵（2010） 楼慈波（2010） 张天浩（2011） 武莉（2011）
周向锋（2012） 陈树琪（2013） 孙军（2013）

首批新世纪百千万人才工程国家级人选

田建国（2004）

国家海外青年学者合作研究基金获得者

陈志刚（2005）

“天津市授衔专家”称号获得者

许京军（2005） 田建国（2005）

天津市杰出青年科学基金获得者

陈树琪（2018） 周向锋（2018） 付学文（2020）

天津市青年拔尖人才

任梦昕（2019）

天津市创新人才推进计划青年科技优秀人才

蔡　卫（2018）　　任梦昕（2019）　　董　校（2020）

教育部“长江学者和创新团队发展计划”创新团队基金资助

弱光非线性光子学重点实验室人员名录/Name List

研究人员/Scientific Staff（53 人）

许京军　王慧田　田建国　陈志刚　张国权　孔勇发　孙骞　宋智　宋峰　臧维平
李宝会　姚江宏　赵丽娟　曹亚安　张天浩　李玉栋　徐晓轩　张心正　周文远　邢晓东
禹宣伊　余华　吴强　孙同庆　武莉　高峰　刘智波　李祖斌　薄方　齐继伟
叶青　潘雷霆　蔡卫　陈树琪　宋道红　孙军　陈璟　李勇男　刘宏德　王斌
皮彪　任梦昕　涂成厚　周向锋　胡毅　鄢小卿　程化　杨帆　付学文　罗维维
董校　张玲（兼）　刘士国（兼）　Romano A. Rupp

技术人员/Technical Staff（4 人）

张玲　刘士国　兀伟　郑大怀

行政人员/Administrative Staff（3 人）

刘烨　李威　唐柏权

博士生/Ph.D Students（152 人）

白宇星　边达民　曹力元　柴若衡　陈慧敏　陈烈裕　陈胜垚　陈祥　陈子禹　程佳琪
戴凡　董浩　樊江　冯源　符显辉　付钰婷　高博锋　高晓莉　高晓梅　耿广州
龚圣超　顾志东　郭浩玮　郭宇翱　韩小芳　郝永鑫　何新玲　贺瑜　侯晶钰　侯梦迪
胡禹俊　胡志婵　黄凯程　黄凯旋　黄宁宁　黄双印　黄松　霍唱福　贾笛　贾鹏博
贾子熙　江晓洁　江欣达　姜小强　姜一凡　焦跃健　进晓荣　靳春艳　雷思弘　黎晓峰
李智　李德康　李登辉　李含飞　李瀚博　李丽　李三兵　李文灿　李小宽　李星业
李志轩　李致力　刘慧　刘灿　刘芳　刘汉雄　刘甲琛　刘建基　刘思宇　刘秀英
刘洋　刘瑶瑶　刘勇良　刘志瑶　卢瑶　罗强　马继娜　马军军　玛地娜　裴雨苗
齐文荣　钱月照　秦娟　桑旭　石召君　史德坤　宋立敏　宋少清　苏宝旺　孙若轩
王超　王海平　王佳艺　王珂　王敏　王强　王日德　王烁琳　王苏云　王维维
王钰　王云龙　王兆远　王志远　王周祥　文虹镜　翁晓基　吴佳坪　吴婧　伍浩
夏士齐　谢飞　谢俊芳　谢雨卿　邢福临　熊浩　徐晓丹　许恩泽　燕文超　杨渤
杨晨　杨佳心　杨建宇　喻彬　詹亦飞　张娅　张迪　张冠林　张弘智　张景雪
张康　张莉　张路　张妮　张盼　张平　张茹　张旭光　张雪静　张亚卿
张煜晨　张跃变　赵侨　赵宏阳　赵梦丹　赵艺　赵泽家　钟阳　周冬旭　周旭
Adnan Khan　Faheem Hassan

硕士生/M.S. Students（217 人）

安亚文　白璐　薄莹雷　边达民　曹博弢　曹翰　曹家欣　曹金泽　曹雷　曹孟尧
车颖　陈栋铭　陈桂林　陈嘉鑫　陈思捷　陈相宇　程麒麟　迟春霞　崔慧琳　崔健
崔芮铭　崔扬君　单益东　党可欣　邓颖　丁海芮　董浩天　董瑞　董艳艳　董卓尧
杜海红　杜浩晴　杜魁瑶　杜宣臻　范春慧　范友静　符显辉　甘绪凡　高静怡　高日翔
高申一　葛天昊　弓楠　郭婵　郭丽娟　郭敏　郭琴琴　韩道博　郝泽霖　何欢
何慧霞　侯喜哲　胡浩　胡慧敏　胡梦媛　胡晓洋　胡月　胡祯　化梦梦　黄露露
黄荣　黄筱钦　黄意博　黄裕　黄转转　纪一涵　靳瑞宁　靳一鸣　康倩倩　康倩倩
康舒婷　孔君　冷荣　李彩芬　李记伟　李佳欣　李金泽　李景　李玲　李美立
李梦羽　李腾飞　李晓荣　李颖　李羽　李圆慧　梁丹丹　梁菁　梁亦豪　梁永胜
刘锦锦　刘俊芳　刘莉娜　刘庆　刘时康　刘鑫　刘旭山　刘雪婷　刘瑶瑶　刘颖博
刘泽文　娄宗帅　罗荣辉　马蕊　马若斌　马文锦　孟生轲　苗慧　莫旻斐　聂海霞
牛彬雯　裴维维　彭晨　齐嘉琳　钱豆豆　任怡洁　邵震　申子媛　石肇基　宋冠廷
宋筱　宋晏玮　宋祎杰　孙文倩　孙悦欣　孙泽鹏　孙治国　台玉可　田倩倩　汪海军

汪梁 王晓 王好南 王浩 王钧谦 王琳 王楠 王瑞 王素钰 王新
王新格 王旭英 王艳春 王艺驰 王俞萱 王昭 王子范 蔚莹琪 温蕊 吴佳琪
吴娟 吴肖 伍泓锦 武兵 夏正聪 谢俊芳 谢语晨 徐畅 徐睿 徐帅
徐西坦 徐笑言 许海洁 薛邦达 颜欣龙 杨东浩 杨国文 杨贺 杨世茹 杨硕
杨娓茹 于殿强 于洪 于世旺 于溪 余莹凤 岳鑫欣 詹晶谚 张海涵 张洪爽
张嘉伟 张蕾 张利 张令龙 张平 张倩南 张文杰 张喜林 张馨元 张雪岩
张亚辉 张亚卿 张宇琦 张玉洁 张毓哲 张月颖 张中正 张子晴 赵茜 赵晨成
赵大平 赵雅丽 赵艺 郑晓晨 郑秀燕 郑忠翔 郑忠忠 周天寒 周娅玲 周郅璨
朱梦红 朱砚涵 朱章航 祝冬兰 祝志茂 庄玉辉 Imad Iqbal

承担主要课题/Projects under Researching

序号	项目名称	项目来源	起止时间	负责人
1	新型线性和非线性人工微结构及器件(2016YFA0301102)	科技部重点专项	2016.06-2021.05	田建国
2	具有拓扑特性的空间光场产生、调控及与微结构相互作用（项目首席）(2017YFA0303800)	国家重点研发计划	2017.07-2022.06	陈志刚
3	激光器工程化与清洗应用中的关键技术(2017YFB0405105)	国家重点研发计划	2017.07-2020.12	宋　峰
4	具有拓扑特性的光量子态与量子效应(2017YFA0303803)	国家重点研发计划	2017.07-2022.06	许京军
5	铌酸锂薄膜光子结构中的非线性效应与频率梳应用(2019YFA0705003)	国家重点研发计划	2019.12-2024.11	薄　方
6	铜锌锡硫薄膜材料微纳结构与缺陷工程(2018YFE0202402)	国家重点研发计划	2019.08-2022.07	武　莉
7	多场调控下拓扑自旋结构的超快动力学研究(2020YFA0309300)	国家重点研发计划	2020.12-2025.11	付学文
8	西部典型缺水地区农村供水排水一体化技术及应用示范(2016YFC0400700)	国家重点研发计划（子任务）	2016.07-2020.12	徐晓轩
9	内窥型 OCT 设备环状模体研制及关键参数计量检测方法的研究(2016YFF0201005)	国家重点研发计划（子课题）	2016.07-2020.12	叶　青
10	人工微结构中的光/声拓扑性质研究(2017YFA0305100)	国家重点研发计划青年项目（子任务）	2017.01-2021.12	任梦昕

序号	项 目 名 称	项 目 来 源	起止时间	负责人
11	介电常数的空间不均匀性对聚电解质体系行为的影响(G20190002001)	科技部“高端外国专家引进计划”项目	2020.01-2021.12	李宝会
12	拓扑光子结构中的线性与非线性光传输(9-14)	科技部国际合作项目	2020.05-2021.11	陈志刚
13	高通量高分辨病理切片扫描(31527801)	国家重大科研仪器研制项目	2016.01-2021.12	周文远
14	光场的超衍射、超聚束效应及其应用(91750204)	国家自然科学基金重大研究计划重点项目	2018.01-2021.12	张国权
15	基于人工微结构的手性精准构筑及其应用(91856101)	国家重大研究计划	2019.01-2021.12	陈树琪
16	光学 XXXX 设计及制造技术研究(2019xxxx)	军委科技委项目基础加强计划	2020.01-2024.12	薄 方
17	渐变***的激光特性研究与构型设计	军委科技委项目基础加强计划	2019.12-2023.12	宋 峰
18	少层人工微结构光场调控物理(11925403)	国家自然科学基金杰出青年科学基金	2020.01-2024.12	陈树琪
19	狄拉克微结构中的光传输与新物理(11922408)	国家自然科学基金优秀青年科学基金	2020.01-2022.12	宋道红
20	空域分形光场的调控、新效应及其潜在应用(11534006)	国家自然科学基金重点项目	2016.01-2020.12	王慧田
21	铌酸锂晶体微腔中的非线性过程与调控研究(11734009)	国家自然科学基金重点项目（子任务）	2018.01-2022.12	薄 方

序号	项　目　名　称	项 目 来 源	起止时间	负责人
22	聚电解质体系中的涨落/关联效应：模拟和理论研究(21829301)	国家自然科学基金海外及港澳学者合作研究基金(延续项目)	2019.01-2022.12	李宝会/ 王　强
23	低维硼的结构预测及性质研究(11674176)	国家自然科学基金面上项目	2017.01-2020.12	周向锋
24	稀土包覆金属纳米核壳结构掺杂液晶的发光调控(11674183)	国家自然科学基金面上项目	2017.01-2020.12	宋　峰
25	基于铌酸锂微盘腔的窄带宽可调谐宣布式单光子源(11674181)	国家自然科学基金面上项目	2017.01-2020.12	薄　方
26	基于铌酸锂芯片的量子光源(11674184)	国家自然科学基金面上项目	2017.01-2020.12	李勇男
27	聚合物手性液晶无序微纳复合材料中的光子局域化及随机激射研究(11674182)	国家自然科学基金面上项目	2017.01-2020.12	张心正
28	抗光损伤铌酸锂晶体与体光生伏打效应的研究(11674179)	国家自然科学基金面上项目	2017.01-2020.12	孔勇发
29	光诱导蜂窝型光子晶格中与赝自旋相关涡旋现象的研究(11674180)	国家自然科学基金面上项目	2017.01-2020.12	宋道红
30	基于二维材料折射率传感的新型光热成像和光声成像研究(11774184)	国家自然科学基金面上项目	2018.01-2021.12	刘智波
31	基于飞秒直写介电微纳结构的光场调控及应用研究(11774183)	国家自然科学基金面上项目	2018.01-2021.12	涂成厚
32	基于微纳共振复合材料的非线性偏振调控效应及其应用研究(61775106)	国家自然科学基金面上项目	2018.01-2021.12	任梦昕

序号	项 目 名 称	项 目 来 源	起止时间	负责人
33	锂基中子探测闪烁共晶的设计、制备及性能表征(11775120)	国家自然科学基金面上项目	2018.01-2021.12	杨 帆
34	纳米尺度铌酸锂的载流子输运和光电性能研究(11774182)	国家自然科学基金面上项目	2018.01-2021.12	张国权
35	嵌段共聚物自组装多孔形态的形成机理研究(21774066)	国家自然科学基金面上项目	2018.01-2021.12	李宝会
36	特殊晶场环境下二价锰离子的非常规获得及反常发光的机理研究(11774187)	国家自然科学基金面上项目	2018.01-2021.12	武 莉
37	线性和非线性多功能超表面光场调控及应用(11774186)	国家自然科学基金面上项目	2018.01-2021.12	程 化
38	紫外波段铝表面等离激元的阴极荧光光谱研究(11774185)	国家自然科学基金面上项目	2018.01-2021.12	蔡 卫
39	基于超分辨成像技术的人红细胞骨架及膜蛋白 CD47 特性的研究(11874231)	国家自然科学基金面上项目	2019.01-2022.12	潘雷霆
40	大面积亚微米手性、赝手性金属微结构光学活性及非对称传输的研究(11874229)	国家自然科学基金面上项目	2019.01-2022.12	齐继伟
41	La 系钙钛矿型光催化材料能带结构精准调控和还原 CO2 机理研究(21872073)	国家自然科学基金面上项目	2019.01-2022.12	曹亚安
42	飞秒激光构造铌酸锂表面平整微纳结构及其重掺杂机理研究(11874227)	国家自然科学基金面上项目	2019.01-2022.12	姚江宏
43	基于宇称-时间对称的量子仿真及其光场调控应用(11874228)	国家自然科学基金面上项目	2019.01-2022.12	陈 璟

序号	项目名称	项目来源	起止时间	负责人
44	碱金属硼化合物的结构预测与高压合成(11874224)	国家自然科学基金面上项目	2019.01-2022.12	周向锋
45	超高时空分辨研究梯度应变对二维材料能量载流子动力学的调制作用(11974191)	国家自然科学基金面上项目	2020.01-2023.12	付学文
46	光伏有机小分子/二维材料异质结构的光电性能研究(11974190)	国家自然科学基金面上项目	2020.01-2023.12	田建国
47	基于少层超表面层间作用的光场联合调控研究(11974193)	国家自然科学基金面上项目	2020.01-2023.12	程化
48	宽光谱、低电压高增益的飞秒激光过饱和掺杂硅光电探测器的研究(11974192)	国家自然科学基金面上项目	2020.01-2023.12	吴强
49	不同工艺制备的低掺镁近化学计量比铌酸锂晶体缺陷结构及其对性能的影响研究(61705059)	国家自然科学基金面上项目（联合申请）	2018.01-2020.12	孙军
50	太赫兹声子极化激元与微结构作用的高时间分辨定量成像研究(61705013)	国家自然科学基金青年基金	2018.01-2020.12	吴强
51	快响应掺铋铌酸锂晶体及其实时动态全息 3D 显示的研究(61705116)	国家自然科学基金青年基金	2018.01-2020.12	郑大怀
52	高压下预测新型水合二氢离子[H4O]2+(21803033)	国家自然科学基金青年基金	2019.01-2021.12	董校
53	聚焦离子束在介质材料微纳加工中光学损伤与修复的理论及关键工艺研究(11904182)	国家自然科学基金青年基金	2020.01-2022.12	兀伟
54	超表面光场自旋选择多维联合调控研究(11904181)	国家自然科学基金青年基金	2020.01-2022.12	李占成
55	各向异性超表面光场联合调控超分辨成像研究(11904183)	国家自然科学基金青年基金	2020.01-2022.12	刘文玮

序号	项目名称	项目来源	起止时间	负责人
56	新型光场调控物理及应用(9175000)	国家自然科学基金	2018.01-2020.12	许京军
57	硼烯的生长表征及性质	天津市自然科学基金杰出青年科学基金	2017.10-2021.09	周向锋
58	基于少层人工微结构的光场调控物理及其应用(18JCJQJC45700)	天津市自然科学基金杰出青年科学基金	2018.10-2021.12	陈树琪
59	梯度应变调控下卤化钙钛矿材料载流子动力学的超高时空分辨研究(20JCJQJC00210)	天津市自然科学基金杰出青年科学基金	2020.10-2024.09	付学文
60	天津市青年拔尖人才推进计划	天津市青年拔尖人才推进计划	2019.01-2022.12	任梦昕
61	天津市青年人才托举工程（第二批）(TJSQNTJ-2018-18)	天津市科协	2019.01-2021.12	董校
62	紫外光激发的金属纳米结构增强发光的单一基质白光 LED 荧光材料(17JCZDJC37800)	天津市自然科学基金重点项目	2017.04-2020.03	宋峰
63	层间转角可控二维材料及其光电性能研究(18JCZDJC30400)	天津市自然科学基金重点项目	2018.04-2021.03	刘智波
64	光电功能半导体材料挠曲光伏效应的载流子动力学机制研究(20JCZDJC00560)	天津市自然科学基金重点项目	2020.04-2023.03	付学文
65	基于飞秒光聚合的新型液晶定向技术及其在矢量光场产生中的应用(17JCYBJC16700)	天津市自然科学基金面上项目	2017.03-2020.03	张心正
66	深紫外非线性光学磷酸盐功能晶体的设计、生长和构效关系研究(17JCYBJC17800)	天津市自然科学基金面上项目	2017.04-2020.03	孙同庆
67	硬 X 射线成像用高分辨碘化铯闪烁屏研制(18JCYBJC17800)	天津市自然科学基金面上项目	2018.04-2021.03	杨帆

序号	项目名称	项目来源	起止时间	负责人
68	基于缺陷调控构筑新型磷酸盐基力致发光材料(19JCYBJC17600)	天津市自然科学基金面上项目	2019.04-2022.03	武莉
69	氢气水合物在极端条件下的超离子化行为研究(20JCYBJC01530)	天津市自然科学基金面上项目	2020.04-2023.03	董校
70	基于超分辨成像技术和光刻图案化技术的细胞骨架调控机制的研究(18JCQNJC02000)	天津市自然科学基金青年项目	2018.04-2021.03	潘雷霆
71	基于石墨烯等离激元的中红外结构光场研究(18JCQNJC02100)	天津市自然科学基金青年项目	2018.04-2021.03	蔡卫
72	层状半导体 ReS2 和 ReSe2 沿 c 轴方向上的稳态和瞬态光谱研究(19JCQNJC01800)	天津市自然科学基金青年项目	2019.04-2022.03	鄢小卿
73	人工微结构光场调控物理及超分辨成像研究(BX20180148)	博士后创新人才支持计划	2018.09-2020.06	刘文玮
74	基于人工微结构的光场调控物理及光场计算(2018M640229)	博士后基金面上项目	2018.09-2020.06	刘文玮
75	基于少层超表面的光场多维度联合调控及其应用研究(2018M640224)	博士后基金面上项目	2018.09-2021.06	李占成
76	三维声学微结构的拓扑赝自旋态研究(2020M680850)	博士后基金面上项目	2020.07-2022.07	谢博阳
77	基于超表面的微腔光场调控及其应用(2020M680851)	博士后基金面上项目	2020.07-2023.07	张跃变
78	锡单质在高压下的电子行为和状态方程研究	实验室开放课题	2020.07-2022.06	董校
79	SiC 光导半导体器件中高光利用率的数值模拟(SKL2019KF03)	实验室开放课题	2020.01-2020.12	宋峰

序号	项目名称	项目来源	起止时间	负责人
80	基于飞秒激光直写的玻璃材料精准加工成型技术的基本问题研究(SYSJJ2019-09)	实验室开放课题	2019.01-2020.12	涂成厚
81	环保节能职能家居产品新技术开发(2017079)	横向课题	2017.04-2020.04	姚江宏
82	《铌酸锂电光调Q晶体规范》标准编制(2019021)	横向课题	2018.01-2020.11	孙军
83	3英寸氧化镓单晶衬底及外延工艺研究(2019296)	横向课题	2018.04-2021.12	刘士国、孙军
84	车载GPS定位终端(2019007)	横向课题	2018.12-2021.12	王斌
85	YAG:Yb晶体闪烁发光与辐照损伤的模型与测试(2019136)	横向课题	2019.02-2020.10	杨帆
86	光学级掺镁铌酸锂晶体的研制(2019132)	横向课题	2019.04-2022.12	孙军、张玲
87	硒化镉晶体的研制(2019109)	横向课题	2019.05-2020.12	孙军、张玲
88	微小金刚石刀具FIB刻蚀加工研究(2019201)	横向课题	2019.06-2020.05	兀伟
89	皮肤烧伤的热传导模拟数值计算模型软件及其仪器的开发(2019327)	横向课题	2019.09-2020.06	徐晓轩
90	光纤分布式传感优化及应用(2019281)	横向课题	2019.09-2021.08	高峰
91	3英寸β-Ga2O3单晶导模法生长设备研究(2019286)	横向课题	2019.09-2021.12	刘士国、孙军

序号	项　目　名　称	项 目 来 源	起止时间	负责人
92	黑硅探测器加工(2019417)	横向课题	2019.10-2020.12	吴　强
93	城市尺度下污染突发事件中基于关联寻因模型下的数据处理(2020136)	横向课题	2019.11-2020.06	徐晓轩
94	高速光学扫描系统的研究(2019413)	横向课题	2019.11-2020.11	叶　青
95	智能时代复杂社会多元化时空数据处理	横向课题	2019.12-2020.06	徐晓轩
96	纳米微柱加工(2020221)	横向课题	2020.01-2020.12	兀　伟
97	超短脉冲激光与硅材料相互作用的物理机理(SKLLIM1903)	横向课题	2020.01-2021.12	吴　强
98	表面增强光谱传感在关节积液中的应用研究(2020266)	横向课题	2020.05-2021.04	王　斌
99	纳米微结构聚焦离子束加工2020(2020389)	横向课题	2020.07-2020.12	兀　伟
100	***数据分析软件(2020317)	横向课题	2020.07-2021.02	徐晓轩
101	皮肤热传导及烧伤程度的计算模拟模型研究	横向课题	2020.07-2022.06	徐晓轩
102	液晶电光样品的研发(2020290)	横向课题	2020.10-2023.09	张心正
103	铌酸锂晶体微盘加工(2020432)	横向课题	2020.11-2021.01	张国权

序号	项目名称	项目来源	起止时间	负责人
104	近红外波段表面增强散射光谱实验研究(2020449)	横向课题	2020.11-2021.02	王斌
105	基于树莓派平台的机器视觉光谱传感模组研发(2020346)	横向课题	2020.12-2021.06	王斌
106	稀土配合物晶体结构分析(2020105)	横向课题	2020.12-2021.06	叶青
107	利用阴极荧光光谱实现等离激元超分辨的研究	南开大学百名青年学科带头人培养计划	2015.01-2020.12	蔡卫
108	等离激元耦合体系中非线性旋光效应对光波偏振的调控研究	南开大学百名青年学科带头人培养计划	2016.01-2021.12	任梦昕
109	基于超分辨光学成像技术的红细胞衰老机制和骨架特性的研究	南开大学百名青年学科带头人培养计划	2019.01-2024.12	潘雷霆
110	硼体系中出现的新型准粒子	南开大学百名青年学科带头人培养计划	2018.01-2020.12	董校
111	新型拓扑特性空间光场的产生与调控(63201004)	基本科研业务费	2020.01-2020.12	蔡卫
112	多功能少层超表面及其应用(63201009)	基本科研业务费	2020.01-2020.12	陈树琪
113	新型光子学材料中新效应及可调光子学微结构器件的研究(63201007)	基本科研业务费	2020.01-2020.12	胡毅
114	弱光非线性光子学效应及其应用(63201003)	基本科研业务费	2020.01-2020.12	任梦昕
115	稀土柔性材料发光性能调控(63201014)	基本科研业务费	2020.01-2020.12	宋峰

序号	项目名称	项目来源	起止时间	负责人
116	铜锌锡硫薄膜太阳电池效率提升的基础研究(63201010)	基本科研业务费	2020.01-2020.12	武　莉
117	折射率色散全自动测量仪的研发(63201012)	基本科研业务费	2020.01-2020.12	叶　青

仪器设备平台/Facilities

仪器设备名称	规格型号	购置时间
聚焦离子束电子显微镜	nanolab 600i	2014.06
分子速外延生长炉	Compact 21T	2003.12
扫描探针显微镜	Nonoscope IIIa	2006.04
激光显微竟拉曼光谱仪	inVia	2009.09
近场扫描光学显微镜系统	MV4000	2009.09
飞秒激光器系统	Legend Elite clsp	2010.03
散射式近场光学显微镜	neaSNOM	2015.04
荧光光谱仪	FSP920	2008.12
研磨抛光系统		2003.12
多轴激光并行直写光刻系统	Microlab 4A-100	2012.04
磁控溅射薄膜沉积系统	KJLC-LAB18	2010.09
激光器工作站	899-29	2005.11
飞秒激光器	VF-T2S	2000.09
时间分辨光谱及瞬态吸收光谱系统		2002.06
飞秒倍频系统		2002.06
显微拉曼光谱仪	MKI2000	1998.01
激光分子束外延系统	LMBE450A	2006.05
钛宝石激光器系统	PRO-FIKXP	2010.03
准分子激光器	COMPexPro205	2009.06
原子力显微镜	MULTZMDE V	2010.03
全自动宽带调谐飞秒激光器	UltraII	2012.12
傅立叶变换红外光谱仪	VERTEX 70	2014.12
连续钛宝石激光器	SolsTis 4000S BRF XF	2015.09
显微弱光探测系统		2008.04
大功率超快激光器	Mai Tai HP	2016.01
显微镜	TI-E	2014.09
服务器	HS21	2009.07
无液氦低温光学恒温器	4106-510	2016.05
超精细多功能无液氦低温光学恒温器	4200-520N	2015.01
皮秒激光器	PY61	2003.12
高脉冲固体激光器	EMPPWER 30-220	2009.01
光谱仪	iHR550	2010.07
倒置显微镜	Axio OpeseverA1	2009.01
纳微结构光耦合测试仪	AP-SA25L003-CM	2014.01
超连续谱光纤激光器	EXR-15	2013.12
高温综合热分析仪	SETSYS Evo	2014.01
氩离子激光器系统	Innova 308C	2007.01
荧光光谱仪	FluoroLog-3	2014.06
氩离子激光器	Inno1a 92-0C-A6	2008.07
纳秒激光器	Panther OPO	2003.12
高级倒置显微镜	TiU	2013.01

仪器设备名称	规格型号	购置时间
光谱型成像椭偏仪	Nanofilm_EP4SE	2017.09
原子力显微镜	MFP-3D Infinity	2017.10
超窄线宽可调谐环形激光器	Matisse 2 DX	2017.11
倒置研究型显微镜	Ti-U	2017.09
高性能计算服务器	X240M5	2017.03
半导体参数测试仪	4200A-SCS	2017.06
倒置研究型显微镜	Ti-E	2017.11
超快激光脉冲整形器	MIIPS-HD	2017.12
超连续谱光纤激光器	EXR-20	2017.06
扫描共聚焦拉曼与多场联用系统	alpha300RAS	2018
X 射线衍射仪	D8 ADVANCE	2018
飞秒激光器	RegA-9000	2018
光学真空镀膜机	STAR-800IR	2018
超连续谱光纤激光器	WL-SC-400-15	2018
连续可调激光器	C-WAVE	2019
超导单光子探测系统	TCOPRS-CCR-SW-85	2019
高分辨率光谱仪	Kymera 328i	2019
工业级 SLA 3D 打印机	Lite600HD-B	2019
连续可调谐半导体激光器	DLC CTL 950	2019
连续可调谐半导体激光器	DLC CTL 1470	2019
高分辨率光谱仪	SR-303I-B-SIL	2019
近红外探测器	C12741-03	2019
瞬态荧光拉曼光谱仪	LabRAM Odyssey	2020
透射电镜原位气体样品杆	Atmosphere 210	2020
透射电镜原位液体样品杆	Poseidon Select	2020
透射电镜原位加热样品杆	Fusion Select	2020
透射电镜原位双倾探针电学测量系统	X-Nano	2020
高精度时间相关单光子探测系统	PicoHarp 300	2020
可编程处理器	WS-010000A-C-S-1-AA-01	2020
网络分析仪	E5061B-3L3	2020

注：除开放基金外，所有仪器设备均为有偿使用

研究工作报告/Scientific Report

弱光非线性及量子相干光学/ Weak Light Nonlinear Optics and Quantum Coherent Optics

负责人：许京军

2020 年度本方向主要在拓扑光子学、等离激元光子学、线性和非线性光场调控及其应用、生物光子学以及新型光电子材料与器件应用等领域取得了系列进展。具体如下：

1. 拓扑光子学

材料的拓扑性质是来自于动量空间的能带结构，并且通常由拓扑不变量“陈数”来描述。涡旋光是实空间具有相位奇点的新颖空间结构光场，具有拓扑特性和轨道角动量，也是目前光学研究中的前沿热点。探究这两种不同空间拓扑结构之间的内禀关联性对于深入理解不同领域的拓扑物理现象具有重要意义。我们实验观测并理论证明了赝自旋涡旋拓扑荷的转换与狄拉克点拓扑特性相关，揭示了动量与实空间拓扑转换的普适规律。我们以赝自旋为 S=1/2 和赝自旋 S=1 的狄拉克光子晶格为平台，实验上利用赝自旋涡旋光激发狄拉克点附近的模式，实验观测和理论证明了赝自旋涡旋拓扑荷转换的数目正好等于动量空间狄拉克点贝里相位的绕数，该拓扑荷转换过程由狄拉克点的拓扑特性决定。理论结果证明赝自旋涡旋拓扑荷的转化规律不仅可以推广到任意整数或半整数的赝自旋体系，而且，对于具有三维动量空间的拓扑奇点，比如具有三维外尔点的体系也同样适用。这证实了拓扑转换从动量空间到实空间的映射规律的普适性。该工作不仅为深入理解拓扑物理现象提供了一个新的视角，而且对凝聚态物理、冷原子物理等其它领域中相关拓扑现象的研究具有重要借鉴意义。

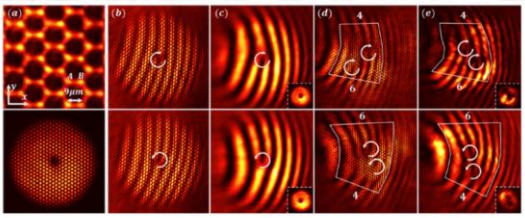

图 1. 赝自旋-1/2 的光子石墨烯中涡旋光拓扑转换的实验结果。

Fig. 1 Experimental results of topological charge conversion in pseudospin-1/2 photonic grapheme.

Topological properties of materials are typically presented in momentum space. Here, we demonstrate a universal mapping of topological singularities from momentum to real space. By exciting Dirac-like cones in photonic honeycomb (pseudospin-1/2) and Lieb (pseudospin-1) lattices with vortex beams of topological charge l, optimally aligned with a given pseudospin state s, we directly observe topological charge conversion that follows the rule l→l + 2s. Although the mapping is observed in photonic lattices where pseudospin-orbit interaction takes place, we generalize the theory to show it is the nontrivial Berry phase winding that accounts for the conversion which persists even in systems where angular momentum is not conserved, unveiling its topological origin. Our results have direct impact on other branches of physics and material sciences beyond the 2D photonic platform: equivalent mapping occurs for 3D topological singularities such as Dirac-Weyl synthetic monopoles, achievable in mechanical, acoustic, or ultracold atomic systems, and even with electron beams.

拓扑光子学的主要研究集中在线性的光学结构中，而非线性效应的引入为拓扑光子学带来了更多新颖的物理现象。我们基于一维 SSH 拓扑光子晶格，实验和理论上研究了光与拓扑光学微结构的非线性相互作用，发现了非线性导致的体态模式向拓扑界面态模式的耦合，并构建出了普适的非线性模式耦合的理论框架（图 2）。我们以一维光诱导 SSH 光子晶格为平台，实验上发现在

拓扑非平庸的光子结构中，非线性能够实现体态和拓扑边界态以及界面态之间的耦合。我们提出了非线性拓扑系统下模式耦合的新理论，并成功地解释了相关实验结果。本工作提出的非线性与拓扑结构相互作用的理论框架具有普适意义，也能够为其它高维的光学系统，乃至光学以外其它非线性拓扑体系的相关研究提供理论借鉴。

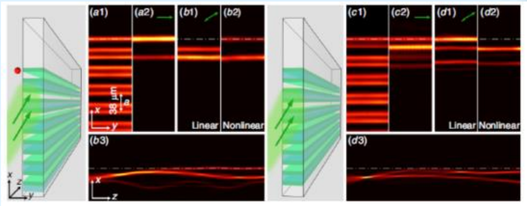

图 2. 拓扑非平庸(左)和平庸(右)的 SSH 晶格中非线性耦合边界态的实验结果。

Fig. 2 Observation of nonlinearity-induced coupling to edge states in topological nontrivial(left) and trivial (right) SSH photonic lattices.

The flourishing of topological photonics in the last decade was achieved mainly due to developments in linear topological photonic structures. However, when nonlinearity is introduced, many intriguing questions arise. For example, are there universal fingerprints of the underlying topology when modes are coupled by nonlinearity, and what can happen to topological invariants during nonlinear propagation? To explore these questions, we experimentally demonstrate nonlinearity-induced coupling of light into topologically protected edge states using a photonic platform and develop a general theoretical framework for interpreting the mode-coupling dynamics in nonlinear topological systems. Performed on laser-written photonic Su-Schrieffer-Heeger lattices, our experiments show the nonlinear coupling of light into a nontrivial edge or interface defect channel that is otherwise not permissible due to topological protection. Our theory explains all the observations well. Furthermore, we introduce the concepts of inherited and emergent nonlinear topological phenomena as well as a protocol capable of revealing the interplay of nonlinearity and topology. These concepts are applicable to other nonlinear topological systems, both in higher dimensions and beyond our photonic platform.

平带体系已涉及到物理学的诸多领域，从电子系统到超冷原子气体，从人工超构材料到光子器件的设计。尤其是在光子学领域，利用平带体系来实现光场调控的可能应用非常广泛，包括光子传感器、光信号处理及图像传输、非线性光学元件和微型激光器等。平带与拓扑这两个概念的有机结合，使得平带光子系统和拓扑光子学的相关研究迎来了极为快速的发展。通常情况下，材料的拓扑性质来自于动量空间的拓扑保护。我们从理论和实验两方面研究了非传统环形平带模式与实空间拓扑保护的关联。虽然这些非传统的环形平带模在理论上被预言，对理解平带系统的基本物理中起着关键作用，但由于对周期边界条件的苛刻要求等原因，在传统材料中很难实现。我们以二维 Kagome 晶格为起点，设计了环形的 Corbino 有限光子晶格结构（见图 3(a)），并利用低功率连续激光直写的方法在非线性晶体中诱导出这样的光子晶格（见图 3(b)），从而首次直接实验观察到了与实空间拓扑特性相关的不可压缩环形态（见图 3(c1)），并实验证明了与非平凡平带环形态相关的边界模式的鲁棒性。通过对不可压缩环形态的直接观测和严格分析表明，环形 Kagome 光子晶格在动量空间中具有平带能带触点，而这些非常规的平带环形态的展现与 Bloch 函数存在奇点有关，由晶格的实空间拓扑特性决定。该研究结果对于理解拓扑平带以及强关联系统的有趣物理现象具有重要意义。该工作发表于研究工作发表在[Phys. Rev. Lett. 124, 183901(2020)]上。

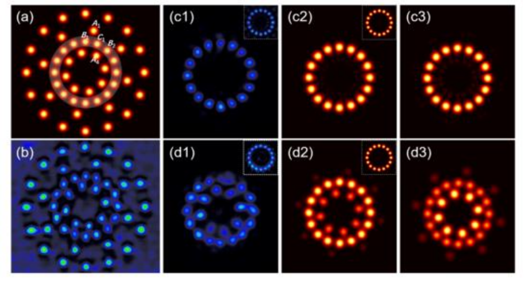

图3. Corbino-Kagome晶格中的非传统的环形平带模直接观测的实验和理论结果。

Fig. 3 Direct Observation of unconventional flatband loop states in Corbino-Kagome photonic lattices.

Flat band systems have been realized and widely studied in a variety of physical systems, ranging from photonic waveguide arrays to synthetic atomic lattices, and from metamaterials to cavity polaritons. The intersection of flat band physics and topology may lead to new physical phenomena and potential novel applications. Topological properties of lattices are typically revealed in momentum space using concepts such as the Chern number. Here, we study unconventional loop states, namely, the noncontractible loop states (NLSs) and robust boundary modes, mediated by nontrivial topology in real space. While such states play a key role in understanding fundamental physics of flatband systems, their experimental observation has been hampered because of the challenge in realizing desired boundary conditions. Using a laser-writing technique, we optically establish photonic kagome lattices with both an open boundary by properly truncating the lattice, and a periodic boundary by shaping the lattice into a Corbino geometry. We thereby demonstrate the robust boundary modes winding around the entire edge of the open lattice and, more directly, the NLSs winding in a closed loop akin to that in a torus. We prove that the NLSs due to real-space topology persist in ideal Corbino-shaped kagome lattices of arbitrary size. Our results could be of great importance for our understanding of the singular flatbands and the intriguing physics phenomenon applicable for strongly interacting systems.

平带系统代表一种具有至少一条无色散能带的周期性晶格，在凝聚态到激子极化子、超冷原子和光学等不同物理分支中都引起了极大的兴趣。在光学中，光子晶格提供了一个可调控的平台，来探索与最初提出的固态物理有关模型有趣的平带现象。在这项工作中，我们利用连续激光直写技术，在非线性晶体的体内建立了有限尺寸的超蜂窝晶格（sHCL)。更重要的是，我们实验观察到了具有特定边界的超蜂窝晶格中的两种平带线态(“直”线和“锯齿”线)，由于某些平带系统的实空间拓扑性质，这些平带态无法通过常规的平带CLSs的叠加得到。事实上，超蜂窝晶格中特有的“锯齿”线态与之前在Kagome和Lieb晶格中观察到的平带线态是不同的。我们的工作不仅揭示了这些有趣的平带状态，而且为在一个新型平台上探索平带和狄拉克物理带来了新的可能性，因为超蜂窝晶格代表的是一种费米电子(自旋 1/2)和玻色子(自旋 1)狄拉克点共存的理想系统。

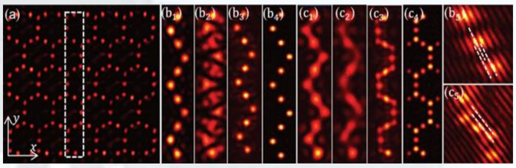

图4. 超蜂窝光子晶格中锯齿形线态的实验证明。

Fig. 4 Experimental demonstration of photonic sHCL and a flatband Zigzag line state.

Flatband systems, periodic lattices hosting at least one completely dispersionless energy band, have attracted enormous interest in different branches of physics ranging from condensed matter to exciton polaritons, ultracold atoms and optics. In optics, photonic lattices provide a promising platform to explore intriguing flatband phenomena associated with the lattice models originally proposed in solid state physics. In this work, by employing a cw-laser writing technique, we establish a finite-sized sHCL in the bulk of a nonlinear crystal. More importantly, we experimentally observe two types of line states (the “straight” and “zigzag” lines) in the sHCL with tailored boundaries which cannot be obtained by superposition of conventional flatband CLSs because they arise from real-space topological property of certain flatband systems. In fact, the zigzag-line states, unique to the sHCL, are in contradistinction with those previously observed in the Kagome and Lieb lattices. Our work not only reveals these intriguing flatband states, but also brings about new possibilities to explore both flatband and Dirac physics in one platform, as the sHCL represents an ideal system where fermionic (spin-1/2) and bosonic (spin-1) Dirac points coexist.

2. 等离激元光子学

近年来，基于超材料设计的等离激元诱导透明（PIT）器件由于其具有简单的实现条件和灵活的设计引起了研究者们的广泛兴趣，各种基于超材料的 PIT 结构被相继提出。然而大部分的 PIT 结构都是由金属材料构成，只能通过改变器件的结构、尺寸或者嵌入其他可调谐材料等办法来实现动态调谐，因此在实际应用中实现对等离激元诱导透明窗口的动态调谐是很困难的。之前的大部分石墨烯等离激元诱导透明结构都是由彼此分离的单元构成，为了对分离的石墨烯结构进行电调谐需要对其添加复杂的金属连接网，这极大地增加了器件制备的难度与成本，并且会很大程度上削弱器件的共振特性。此外，许多 PIT 超材料结构所展现出的透射谱特性为单频带，即只有一个诱导透明窗口，而且诱导透明窗口的最大透射率较低、带宽较窄，这限制了 PIT 器件的实际应用。我们根据“和田湖”拓扑结构提出一种全新的可电调谐的三栅极多功能石墨烯超表面，具有宽带、大调谐范围的太赫兹石墨烯等离激元诱导透明窗口，并对其进行了数值研究。我们设计的连续石墨烯结构比采用离散石墨烯结构在样品制备和调控过程中的存在明显优势。由于石墨烯偶极子和单极子天线之间的相消干涉，在透射谱中观察到了明显的单透明窗口和双透明窗口。进一步的研究表明，通过调控石墨烯中的费米能级，可以动态控制透明峰的光谱位置和谱线。我们通过控制费米能级实现了器件的多功能性和高带宽。对比之前的在一个平面上的由离散石墨烯构成的 PIT 结构，我们还可以通过控制费米能级来实现器件工作频段的整体移动，这一点在实际应用中具有很大的优势。我们实现了群折射率的主动调控，其最大值高达 819。所设计的结构用于制作太赫兹折射率传感器时，其折射率灵敏度高达 1.224THz/RIU。我们展示了我们设计的超表面在太赫兹带阻滤波器、太赫兹折射率传感器、近场上的光开关、慢光器件等领域巨大的潜在应用价值，为之后可调石墨烯超表面超材料的设计提供了非常有意义的指导。

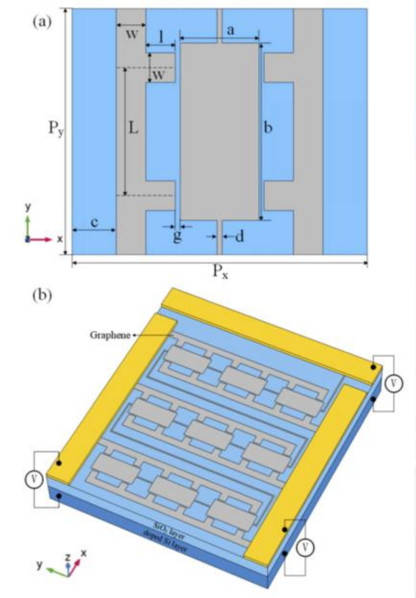

图 13. (a) 原胞结构示意图; (b) 三栅石墨烯超材料（TGGM）器件整体结构示意图。

Fig. 13 (a) Schematic diagram of a unit cell; (b) Schematic diagram of the overall structure of the TGGM device.

Many plasmon-induced transparency (PIT) metamaterials previously reported had limited functions. Their tunabilities were realized by complex discrete structures, which greatly increased the difficulty and cost of device fabrication and adversely affected their resonance characteristics. It is an open question to adjust the Fermi levels of many graphene patterns with only a few in-plane electrodes. We propose and numerically study a novel electrically tunable and multifunctional trigate graphene metamaterial (TGGM) based on the concept of “Lakes of Wada”. Benefiting from the trigate regulation, our proposed TGGM turns out to exhibit excellent characteristics, that can not only be used for terahertz band-stop filter, terahertz refractive index sensor, near-field optical switch, slow-light device, but also for double PIT window metamaterial with broad transparency windows and large tunable frequency range.

铝等离激元在紫外-可见波段具有优良的等离激元响应，精确理解铝纳米结构的等离激元响应对于设计基于铝的等离激元器件，如紫外的表面增强拉曼散射和辐射控制等具有重要意义。在该工作中，我们利用阴极荧光光谱技术对铝-介质-铝等离激元圆盘腔进行了研究，证实了铝等离激元实现光场的高度局域。研究结果表明在 240 纳米直径的圆盘腔中，电磁场能局域在约 105nm^3 的模式体积中。该研究为金属-介质-金属腔用于研究强光-物质相互的研究提供了可能。

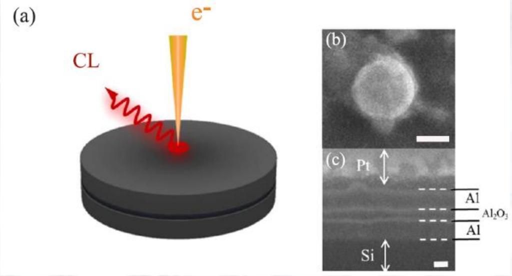

图 14. 蓝光量子点与铝金属-介质-金属腔的强耦合。

Fig. 14 (a) Schematic demonstration of the coupled system. (b) 52°Tilted view of a SEM image of a circular MIM resonator with D = 300 nm. Scale bar is 80 nm. (c) SEM image of the cross-section of the MIM resonator. (d) CL spectrum of CdZnS/ZnS QDs that are spin coated on bare Al film. (e) CL spectrum of an Al–CuInZnSe/ZnS QDs–Al disk resonator. (f) CL spectrum of an Al–CdZnS/ZnS QDs–Al circular resonator.

Aluminum (Al) processes excellent plasmon response from the ultraviolet (UV) to visible spectrum. Understanding of the deep sub-wavelength plasmon response of Al nanostructures is essential for the Al-based plasmon device design, such as UV surface-enhanced resonance Raman scattering and emission control of emitters. In this work, by using cathodoluminescence, the plasmonic properties of Al metal–insulator–metal (MIM) disk nanocavities are investigated. The resonant breathing modes rather than edge modes are resolved by the CL spectra and real space mode patterns, which are in good agreement with the electromagnetic calculations. Moreover, the dispersion behavior of plasmon modes of the MIM cavity can be traced back to the propagating plasmon modes in an Al MIM slab, which shows that the electromagnetic fields are strongly confined in the cavities. Furthermore, a mode volume as small as 1.1×105 nm^3 is obtained for the 240 nm diameter cavity, demonstrating these MIM resonators to be ideal candidates for studies of strong plasmon-matter interactions.

由于等离激元的高度场局域，量子点激子与等离激元的室温强耦合得以实现，为量子信息体系、超低功率的光开关等领域提供了基础。在该工作中，我们基于阴极荧光光谱技术，实现了 CdZnS/ZnS 蓝光量子点激子与铝金属-介质-金属圆盘腔的强耦合，该强耦合利用的是局域电子束激发的成键呼吸模式，而不是传统的远场光激发的等离激元模式。同时，利用电子束对激元模式的超分辨成像能力，实现了强耦合模式的实空间超分辨成像。该研究不但将强耦合的频率拓展到了蓝光区域，而且证实自由电子束在探索量子模式方面的潜在应用。

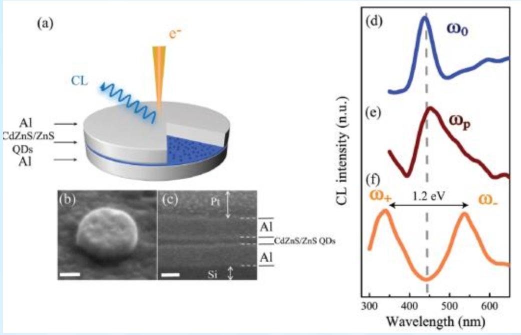

图 15. 铝-三氧化二铝-铝等离激元腔模式的阴极荧光光谱探测图。

Fig. 15 (a) The schematic illustration of Al–Al_2O_3–Al cavity. The cavity was excited by an electron beam and CL spectra are obtained. (b) SEM image of the circular MIM resonator with D=280nm in top view. Scale bar is 140 nm. (c) SEM image of the cross section of MIM cavity shows that the middle layer Al_2O_3 is sandwiched between two Al layers.

Strong coupling originating from excitons of quantum dots and plasmons in nanocavities can be realized at room temperature due to the large electromagnetic field enhancement of plasmons, offering building blocks for quantum information systems, ultralow-power switches and lasers. However, most of the current strong coupling effects were realized by the interaction between excitons and far-field light excited bright plasmon modes in the visible range. Beyond that, there is still a lack of direct imaging of polariton modes at the nanoscale. In this work, by using cathodoluminescence, ultrastrong coupling with Rabi splitting exceeding 1 eV between bonding breathing plasmons of aluminum (Al) metal–insulator–metal (MIM) cavities and excited states of CdZnS/ZnS quantum dots was observed in the near-ultraviolet (UV) spectrum. Further, the hybridization of the QDs excitons and bonding breathing plasmonic modes is verified by deep-subwavelength images of polaritonic modes in real-space. Analytic analysis based on the coupled oscillator model and full-wave electromagnetic simulations is consistent with our experimental results. Our work not only indicates the great potential of electron excited plasmon modes for strong coupling applications, but also extends the polaritonic frequency to the UV range with Al nanocavities.

相变是广泛存在于自然界中的一类突变现象，它为人们调控材料性质提供了重要的手段。近年来，超构材料作为一种新型的人工微纳结构材料，展现出众多天然材料所不具有的、新奇的力、热、光、电、磁等特性，迅速成为研究的前沿热点，并已表现出极大的应用价值。本年度，我们发展了新的晶格耦合手性振子模型，在理论上预测并在实验上验证了人工超构材料中手性旋光相变效应的存在。该研究结果对新型微纳偏振光学元件的设计，以及高灵敏全光开关的研发提供了新的思路，为开启新型人工相变超构材料及其特性调控的研究奠定了理论与实验基础。【Phys. Rev. Lett., 125, 237401 (2020)】。

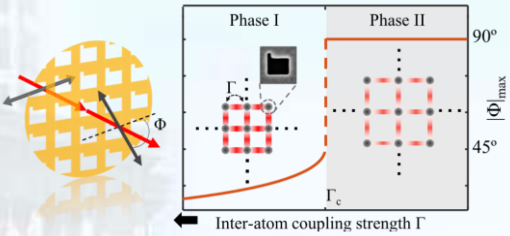

图 16. 人工超构材料手性旋光相变效应示意图。

Fig. 16 A schematic of the phase transition optical activity in chiral metamaterial.

Phase transition is a kind of phenomenon widely existing in nature. It provides an important means for people to control the properties of materials. In recent years, metamaterials, as a new type of artificial micro-nano structured materials, exhibit novel properties such as force, heat, light, electricity, and magnetism that many natural materials do not have. It has quickly become a frontier research hotspot and shown great application value. This year, we developed a new lattice-coupled chiral oscillator model, theoretically predicted and experimentally verified the existence of the chiral phase transition effect in artificial metamaterials.

The research results provide new ideas for the design of new micro-nano polarization optical elements and the research and development of highly sensitive all-optical switches, and lay a theoretical and experimental foundation for the research on new artificial phase-change metamaterials and their property control.

光学非互易器件是光学回路里必不可少的光学元件之一。随着集成光学的发展，片上集成的小尺度非互易器件，包括片上集成光隔离器、光环形器等，成为了国际上的研究热点问题。这里我们设计了一个简单的片上集成光隔离器，该隔离器由 MIM 波导和填充有磁光材料的盘腔组成。 在这种光隔离器结构中，通过横向自旋-轨道耦合有效地增强了横向磁光效应。对于更小的角模式数 n，增强效果更为显着。基于这种自旋轨道增强的横向磁光效应，可获得高性能的片上集成光隔离器，最大隔离度大于 40 dB，插入损耗约为 2dB。并且横向自旋-轨道能够使得在很宽的波长范围内，磁光效应都很强。此外，我们证明了在相同波长范围内，更小的盘腔将具有更强的横向磁光效应。我们的研究为高度集成磁光器件的实现提供了新的视角。

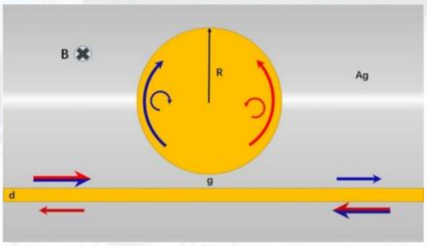

图 21. MIM 波导与盘型腔组成的片上集成光隔离器示意图。

Fig. 21 Schematic diagram of the optical isolator structure composed of a MIM waveguide and a disc cavity.

Optical nonreciprocal devices are one of the indispensable optical components in the optical circuit. With the development of integrated optics, small-scale non-reciprocal devices integrated on-chip, including on-chip integrated optical isolators, optical circulators, etc., have become international research hotspots. Here，a simple on-chip integrated optical isolator composed of a MIM waveguide and a disc cavity filled with magneto-optical material is designed. In this optical isolator structure, the transverse magneto-optical effect is enhanced effectively by the transverse spin-orbit coupling. And the enhancement is more significant for smaller azimuthal mode number n. Based on the enhanced transverse magneto-optical effect, high-performance on-chip integrated optical isolator is obtained, the maximum isolation greater than 40 dB with insert loss about 2dB. The transverse magneto-optical effect keeps strong in a wide wavelength range. Furthermore, it is certified that a smaller cavity will have a stronger transverse magneto-optical effect in the same wavelength range. Our research provides a new perspective for the realization of highly integrated magneto-optical devices.

3. 线性和非线性光场调控及其应用

非傍轴自加速光自被提出以来，在光子学以及许多其他领域得到了广泛的研究。目前大部分研究都集中在二维范畴，这样的光束不可避免会具有聚焦松散的缺点。三维情况下的自加速光在实验上实现时会面临着球差以及振幅调制等诸多问题。在我们的认知范围内，尚未有人能成功实现。在这里，我们首次在实验上实现了三维非傍轴自加速光（图 5）。这些光束是通过在球差补偿系统中对相位调制后的波前进行傅里叶变换得到的。编码的相位信息包含了三维非傍轴自加速光的相位、振幅信息以及附加的球差补偿修正相位信息。这些光束沿着一个圆弧轨迹传输，但是它们展示出了非常复杂的光斑形貌，这些形貌是由在抛物线、扁球面以及长球面坐标系内获得的无衍射解决定的。

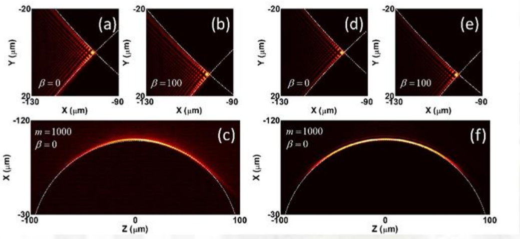

图 5. 抛物线加速光束在不同 值下的实验结果(a-c)和数值模拟结果(d-f)。(a)和(b)为 平面的强度包络图；(c)为(a)光束的传播剖面图；(d-f)对应于(a-c)。白色虚线描绘了焦散线。

Fig. 5. Experimental results (a-c) and numerical simulations (d-f) of parabolic accelerating beams for different values of . (a) and (b) Intensity profiles at plane; (c) propagation of the beam in (a); (d-f) correspond to (a-c). The white dashed lines depict the caustics.

Since non-paraxial accelerating beams (NABs) were conceived, they have been extensively studied in photonics and many other fields. At present, most of the research focuses on their two-dimensional configurations, which inevitably lead to a loose focusing of light. In fact, the three-dimensional (3D) NABs faces lots of difficulties in the experimental realization, such as those associated with spherical aberration and amplitude modulation. So far to our knowledge, no one has been able to successfully produce 3D NABs. Here, we experimentally realize 3D non-paraxial accelerating beams (Fig. 5). They are obtained by Fourier transforming a phase-modulated wave front in an aberration-compensated system. The phase pattern is encoded to include the phase and amplitude modulation for the accelerating beams with additional correction phase for the aberration compensation. These beams propagate along a circular trajectory, but they exhibit rather complex intensity patterns corresponding to the shape-invariant solutions in parabolic, prolate spheroidal and oblate spheroidal coordinate systems.

拉比振荡是受驱动的二能级系统中为人熟知的一种现象。这种现象最早由拉比在核磁共振问题中提出。尽管磁场一般能带来如量子霍尔效应中的手性边界态等典型手性动力学行为，但是人们仍不知道在拉比振荡问题中是否存在手性效应。在本工作中，我们揭示了拉比振荡中相位携带的内在手性。对于相反符号失谐量的外加驱动场，相位和几率幅的演化会表现为镜像对称。这种手性现象可体现在两个由不同初始能级出发的拉比振荡的相干性上，实现受对称保护并且能级依赖的相干长消关系。实验上，我们在可调谐的光子拉比晶格中实现了这种手性效应。我们的结果对受驱动二能级系统的动力学机制带来了更深入的理解。

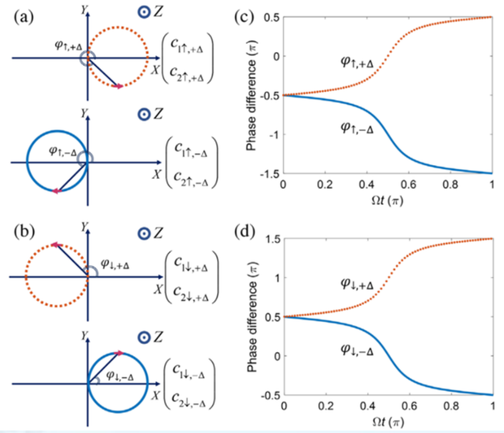

图 6. 从不同能级出发的两个拉比振荡过程的相干关系。(a, b) 两个拉比振荡过程在上下能级的布洛赫矢量方位角的相位差。(c, d) 典型相位差的演化。蓝色实线和红色虚线分别对应负和正失谐量的情形。

Fig. 6 Coherent relationship between two processes of Rabi oscillations initiated from different energy levels. (a, b) duplication of the phase difference between the two Rabi processes at either upper or bottom level in the azimuthal angle of a Bloch vector; (c, d) typical evolution of the phase difference. Blue solid and red dashed lines correspond to the cases of negative and positive detunings, respectively.

Rabi oscillation, originally proposed in nuclear magnetic resonance, is a well-known phenomenon associated with a driven two-level system. Although magnetic fields typically can bring about chirality into unusual phenomena such as chiral edge states in the quantum Hall effect, it is not clear if chirality exists in Rabi oscillations. Here we unveil the intrinsic chirality carried by the phase in a Rabi problem. For opposite detuning of the driving field, the phase evolution of the probability amplitude exhibits a mirror symmetry. Consequently, constructive or destructive interference of two off-resonant Rabi processes under different initial conditions is level dependent and symmetry protected. Experimentally, we demonstrate such features in a photonic setting with adjustable detuning, yet our results may prove pertinent to the study of similar phenomena in other driven two-level systems beyond photonics.

我们在均匀的一维光子晶格中实现了单束类高斯光束的非线性自弯曲传输。该现象的产生是由于光束包含的正常和反常衍射成分在空间上自发分离，二者在非线性作用下实现了同向加速传输。这种同向加速传输描述了类似正质量和负质量物体的两束光之间的共同加速行为。我们探究了光束自弯曲传输过程中入射光束初始动量和非线性强度对传输的影响。进一步实现了部分相干光束的自弯曲传输，并讨论了相干度对加速强度的影响。

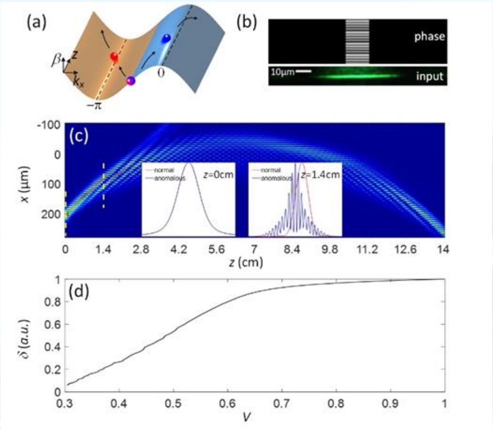

图 7. (a) 光束频谱演化示意图。(b) 实验上产生的类高斯光束和相位模板。(c)光束长距离传输模拟结果（插图表示传输距离为 0 和 1.4 厘米处正常衍射和反常衍射区频谱对应的波包分布）。(d) 不同相干度（*V*）对应的光束质心位移量。

Fig. 7. (a) Schematic spectrum evolution. (b) Phase pattern (upper panel) for generating a Gaussian-like beam (bottom panel). (c) Numerical beam propagation for a longer propagation distance (the insets show the components in the normal and anomalous diffraction regions at $z = 0$ and 1.4 cm). (d) Numerically calculated shift δ of the beam center for various degrees of coherence (characterized by the visibility *V*)

Recently, a new technique of direct reading nonlinear responses was theoretically proposed and further experimentally demonstrated. This approach, replying on one-dimensional Airy beams, manifests some drawbacks. The spreading of this optical field in one direction not only causes a waste of energy, but is also adverse for detecting small samples. Here, we address these issues by extending the mapping technique into two-dimensional (2D) regime via two-dimensional Airy beams. Thanks to the accelerating property of a 2D Airy beam, the nonlinear response of a medium can be spatially mapped in various transverse directions rather than merely along the beam acceleration direction. The most efficient mapping takes place along some particular transverse directions, exhibiting a relevance to the structure of the Airy beam and the type of the nonlinear response.

非线性响应的可视化技术最近被提出并被实验验证。由于依赖一维艾里光束，此方法还存在一些缺陷。该光束沿某一方向延展，不仅会造成能量的浪费，而且不利于探测小尺寸的样品。因此我们将这种方法拓展到了二维情形——即利用二维艾里光场实现了非线性响应的可视化测量。尤为重要的是，我们发现二维艾里光场带来了二维的加速势场，这使得非线性响应的映射不再仅仅沿着加速度的方向，而在其它方向也可实现可视化，并存在一个最佳的可视化角度。我们的结果表明这个最佳角度与艾里光场的结构以及非线性响应的类型都密切相关。

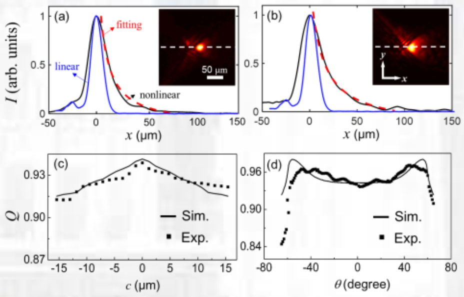

图 8. (a-b)二维艾里光束在弱(a)和强(b)的光折变非线性下的出射实验结果。内插图为对应的光场形貌。沿内插图中白色虚线所示的方向读取出光强分布，并对其右侧进行非线性响应函数的拟合，如图中红色虚线所示。(c,d)沿不同水平方向(c)

和径向(d)分布的光场形貌与光折变响应函数的拟合度。

Fig. 8 (a-b) Measured nonlinear output patterns for a 2D Airy beam under a weak (a) and strong (b) photorefractive nonlinearity. The nonlinear response function (dashed red curves) are used for fitting the right sides of the beam profiles taken along the white dashed lines shown in the corresponding insets. (c,d) The fitting degrees along horizontal (c) and radial (d) directions of the Airy beam.

Recently, a new technique of direct reading nonlinear responses was theoretically proposed and further experimentally demonstrated. This approach, replying on one-dimensional Airy beams, manifests some drawbacks. The spreading of this optical field in one direction not only causes a waste of energy, but is also adverse for detecting small samples. Here, we address these issues by extending the mapping technique into two-dimensional (2D) regime via two-dimensional Airy beams. Thanks to the accelerating property of a 2D Airy beam, the nonlinear response of a medium can be spatially mapped in various transverse directions rather than merely along the beam acceleration direction. The most efficient mapping takes place along some particular transverse directions, exhibiting a relevance to the structure of the Airy beam and the type of the nonlinear response.

设计了相位横向空间关联的啁啾随机相位光栅，对入射激光波前进行调制，获得了双光子聚束峰值为15.38，可见度为92.5%的超聚束光场。研究发现该聚束光场同时具有双光子聚焦效应，其双光子聚束峰半高宽随着光栅狭缝数目的增加而减小。采用腔增强参量下转换过程，通过优化相互作用光束的模式匹配，获得了线宽为 265kHz、光谱亮度为216 pairs/(s·mW·MHz)的606 nm 简并纠缠双光子对。

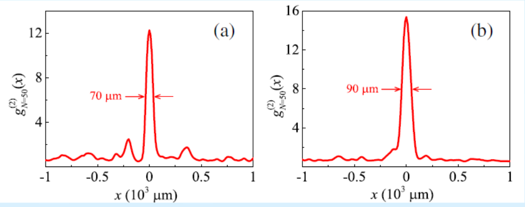

图 22. 基于狭缝数为 N=50 的狭缝宽度啁啾(a)和光栅周期啁啾(b)随机相位光栅的双光子超聚束聚焦效应实验结果。

Fig. 22 Experimental results for the two-photon super-bunched focusing effect through slit-width (a) and greeting-period (b) chirped random-phase greetings with a slit-nmuber N=50.

We desiged a kind of chirped random-phase gratings with spacially correlated phase in the transverse dimension to modulate the wavefront of the incident laser beams, and got super-bunched light fields with a two-photon bunching peak of 15.38 and a high visibility of 92.5%. The super-bunched light fields were also found to be of two-photon focusing effect and the full width at half-maximum of the super-bunched spot decreases significantly with an increase in the greeting slit number. In addition, by employing the cavity-enhanced spontaneous parametric down conversion and optimizing the mode-matching among the interacting beams, we produced an entangled photon-pair source with a bandwidth of 265 kHz at 606 nm and a spectral brightness of 216 pairs/(s·mW·MHz) per longitudinal mode.

通过控制锥形光纤矢量模与回音廊模耦合的夹角，我们成功地实现了回音廊模的Fano线型调控。透过光谱可以在典型的带阻滤波，带通滤波及各种斜率的Fano线型间调控。理论与实验一致性很好。该结构具有结构简单和调控性强的特点。

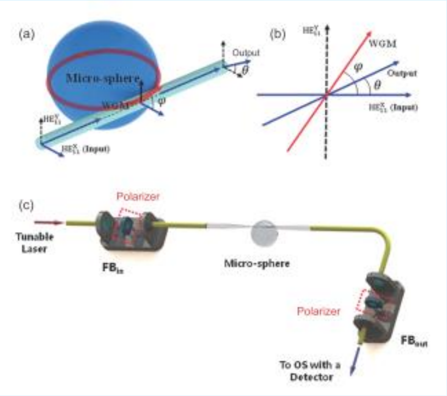

图23. 回音廊模与矢量模构成Fano线型的实验图。(a) 各参与模式的空间关系；(b) 各参与模式的角度关系；(c) 实现Fano线型的实验配置。

Fig. 23 Map of the polarizations of the WGM and modes in the TF, with the corresponding experiment configuration. (a) and (b) are the polarizations maps, and (c) shows the experiment setup.

By the coupling between the vector modes in a tapered fiber and the whispering gallery mode, a Fano-like spectra were demonstrated. The spectra could be optimized between a Lorentz notch, Fano-like spectra and Lorentz peak by changing the angle between the modes. The experimental results were in agreement with the theory. The structure is simple and of good tenability.

4. 生物光子学

细胞间桥是细胞分裂末期在两个子细胞之间形成的胞质连通结构，直径1~2 μm，可介导细胞器、mRNA等物质传递，但其可否、如何介导子细胞间的钙信号通讯仍不清楚。我们基于光刻图案化技术设计了哑铃状图案来操控BV-2小胶质细胞的分裂，最终诱导其子细胞之间形成长度达十几微米、存在时间达数十分钟的细胞间桥。应用微局域机械力刺激其中一个子细胞引发钙升高，随后诱导另一个子细胞发生钙动员，发现细胞间桥既可以介导钙离子自由扩散，也可介导IP_3导致的钙库释放。利用扩散方程对钙离子和IP_3在细胞间桥中的扩散行为以及二者在两个子细胞中的浓度变化进行了数值模拟，理论结果与实验吻合。相关结果为研究细胞有丝分裂现象和钙信号在狭长结构中的传递行为提供了新的实验方案和新思考视角。

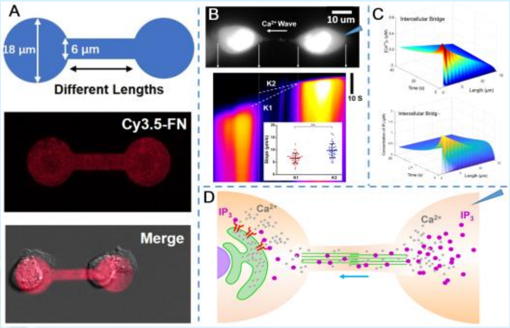

图 9. 基于光刻图案化技术的细胞间桥介导的胞间钙波通讯研究。

Fig. 9 Study of intercellular bridge-mediates Ca^{2+} communications based on photolithography technology.

Intercellular bridges are plasma continuities formed at the end of the cytokinesis process that facilitate intercellular mass transport between the two daughter cells. However, it remains largely unknown how the intercellular bridge mediates Ca^{2+} communication between post-mitotic cells. In the present work, we utilize BV-2 microglial cells planted on dumbbell-shaped micropatterned assemblies to resolve spatiotemporal characteristics of Ca^{2+} signal transfer over the intercellular bridges. With use of such micropatterns considerably longer and more regular intercellular bridges can be obtained than in conventional cell cultures. The initial Ca^{2+} signal is evoked by mechanical stimulation of one of the daughter cells. A considerable time delay is observed between the arrivals of passive Ca^{2+} diffusion and endogenous Ca^{2+} response in the intercellular bridge-connected cell, indicating two different pathways of the Ca^{2+} communication. The observations prove that both, passive Ca^{2+} diffusion and IP_3-mediated endogenous Ca^{2+} response contribute to the Ca^{2+} increase in intercellular bridge-connected cells. Moreover, a simulation model agreed well with the experimental observations. Our work brought a new understanding in Ca^{2+}

signaling mediated by the intercellular bridge during mitosis, as well as proposed an insight into the Ca^{2+} transmission in narrow bounded structures.

超分辨成像技术在生命科学领域发挥着巨大作用，然成像过程往往需要耗费较高的时间和金钱成本。我们利用自主搭建的随机光学重构超分辨显微镜获得细胞微管骨架超分辨图像，然后采用双线性插值降采样法处理得到低分辨率输入图集，再分别使用传统的三次样条插值法和增强型深度超分辨率神经网络进行学习训练，实现低分辨率图像的超分辨重建。结果显示通过深度学习所重建的各种降采样图像效果均优于传统插值法，尤其是二倍降采样重建图像在主观和客观评价指标上可比拟实验获得的微管骨架超分辨图像。基于增强型深度超分辨率神经网络深度学习的细胞骨架图像超分辨重建有望提供一种简捷、有效和高性价比的成像方法，应用于对细胞骨架超微结构的快速预测。

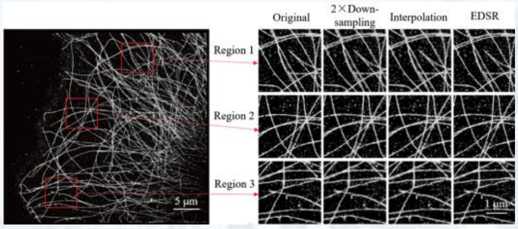

图 10. 基于 EDSR 网络深度学习对二倍降采样细胞微管骨架实验图的超分辨重建。

Fig. 10 Deep-learning-based super-resolved images from twice down-sampling STORM images of microtubule filaments in Cos-7 cells.

Super-resolution microscopy techniques provide unprecedented access to life science research. However, these techniques often require high cost of time and money. Herein, we used the down-sampling images of microtubule filaments obtained from stochastic optical reconstruction microscopy (STORM) by bilinear interpolation as input. We aimed to transform the low-resolution input images into super-resolution ones based on training with an enhanced deep super-resolution (EDSR) neural network. Results showed that the reconstructed microtubule images utilizing deep learning had higher quality than that of traditional cubic spline interpolation method. Especially, the super-resolution images reconstructed from twice down-sampling ones by deep learning exhibited both good subjective and objective evaluation comparable to the original STORM images. Therefore, super-resolution reconstruction of cytoskeleton image via deep learning with EDSR network is expected to provide a concise, potent and cost-effective imaging method, and will be extensively applied in the fast prediction of the delicate cytoskeleton ultrastructure.

5. 新型光电子材料与器件应用

基于柔性应变材料的传感器在智能机器人、健康监测、人体运动检测等领域有着广泛的应用前景。二维材料具有十分优异的电学、机械、热学、光学特性，已经广泛应用于自旋电子、柔性电子、微电子、超透镜、太赫兹、超级电容、传感器等多个领域。与此同时，二维材料具有原子级超薄的厚度和柔韧性，使得人们可以通过弹性应变工程来改变材料的相关结构和机械性质，从而实现调控材料的电子结构性质。我们合成了高质量三元化合物 $SnS_{1.26}Se_{0.76}$ 单晶纳米片，并设计制作了具有可见近红外波段宽光谱响应的柔性光电探测器。该器件在 532nm 激光照射下，具有约 262A/W 的光响应，1.98×10^{11}Jones 的探测率和约 10ms 的光响应时间。自此基础上，我们发展了一种基于 $SnS_{1.26}Se_{0.76}$ 纳米片的电阻式、可重复、高灵敏应变传感器，在 0.9%的低应变范围内具有很好的重复性和线性。通过减小纳米片厚度增加传感器的初始电阻的方式，将此传感器的应变灵敏度提高到 69.7。理论模型和第一性原理计算证实了这种高灵敏度是由应变引起的能隙变宽和态密度降低引起的。

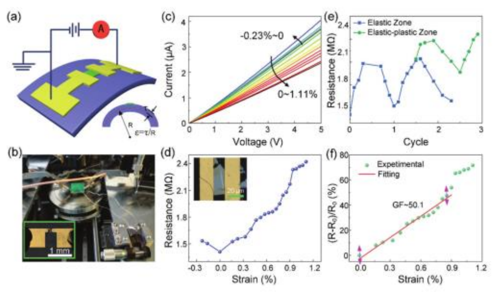

图 11. SnSSe 薄片应力传感器的电学性能测量。

Fig. 11 Electric measurement results of the SnSSe flakes- based strain sensors under bending strain.

Flexible strain-sensitive-material-based sensors are desired owing to their widespread applications in intelligent robots, health monitoring, human motion detection, and other fields. High electrical–mechanical coupling behaviors of 2D materials make them one of the most promising candidates for miniaturized, integrated, and high-resolution strain sensors, motivating to explore the influence of strain-induced band-gap changes on electrical properties of more materials and assess their potential application in strain sensors. Herein, a ternary SnSSe alloy nanosheet-based strain sensor is reported showing an enhanced gauge factor (GF) up to 69.7 and a good reproducibility and linearity within strain of 0.9%. Such sensor holds high-sensitive features under low strain, and demonstrates an improved sensitivity with a decrease in the membrane thickness. The high sensitivity is attributed to widening band gap and density of states reduction induced by strain, as verified by theoretical model and first-principles calculations. These findings show that a sensor with adjustable strain sensitivity might be realized by simply changing the elemental constituents of 2D alloying materials

液晶所具有的光学各向异性、流动性以及对外界激励（温度、电场、压力、磁场等）具有响应等独特性质使液晶器件功能多元化，在电光调控、传感器、激光器等方面有广阔的应用前景，对研发新型液晶器件有重要意义。液晶材料作为一种光学各向异性材料，本身还是一种天然的散射体系，再加上其具有对温度、电场及磁场等外界激励的响应，很适合用于随机激光器的研究和应用。我们制备了无序染料掺杂手性液晶，通过掺杂不同浓度的手性剂控制手性液晶中的选择性反射带光谱位置，使用波长为 532 nm 的纳秒激光器激发样品，分析不同选择性反射带的样品对随机激射的影响，结果显示带边激射的波长会随着选择性反射带的移动而发生变化，而随机激射的发射范围一直在染料荧光峰附近而不会移动。而且选择性反射带与染料荧光峰重叠的样品随机激射阈值更低，如果泵浦光波长正好处于选择性反射带带边，随机激射阈值将进一步降低，这对实现低阈值的随机激射光器具有重要意义。

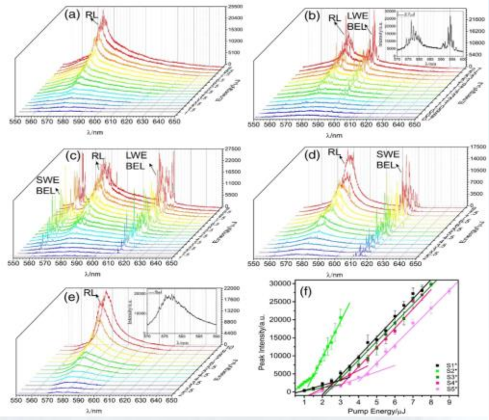

图 12. (a-e)样品 S1*, S2*, S3*, S4*, S5*的发射谱；(f)不同样品中随机激射的峰值光强随泵浦能量的变化。

Fig. 12 Spectra (a)–(e) represent emission for different disordered samples S1*, S2*, S3*, S4*, S5*, respectively. (f) The dependence of the peak intensities of the random lasing on the pump energy for different concentrations of the chiral agent.

Random lasing was experimentally investigated in pyrromethene 597-doped strongly disordered chiral liquid crystals (CLCs) composed of the nematic liquid crystal SLC1717 and the chiral agent CB15. The concentration of the chiral agent tuned the bandgap, and disordered CLC microdomains were achieved by fast quenching of the mixture from the isotropic to the cholesteric phase. Random lasing and band edge lasing were observed synchronously, and their behavior changed with the spectral location of the bandgap. The emission band for band edge lasing shifted with the change of the bandgap, while the emission band for random lasing remained practically constant. The results show that the threshold for random lasing sharply decreases if the CLC selective reflection band overlaps with the fluorescence peak of the dye molecules and if the band edge coincides at the same time with the excitation wavelength.

由于制备简便、高灵敏度和 CMOS 兼容等诸多优势，硅基光电器件展现出诱人的应用前景。然而，由于低响应度以及光电响应在亚带隙波段的急剧衰减，硅基器件的应用目前受到了一定的限制。尽管上述限制可以通过飞秒激光改性而得到部分解决，但是飞秒激光烧蚀带来的表面缺陷和较低的载流子活化率会导致暗电流的急剧上升和窄的光谱响应，这些问题目前还没有得到令人满意的解决方案。我们通过快速热退火和表面氢化钝化的方式，以提高飞秒激光改性后硅基光电探测器的宽光谱高响应度特性，并抑制其暗电流。在最佳条件下，优化后的硅基器件在室温下 20 V 时的亚带隙响应可达 0.80 A/W@1550 nm，其红外响应可与商业锗光电二极管相媲美，并且远高于先前报道的硅光电二极管。此外，优化后的光电探测器具有 400 至 1600 nm 范围的宽光谱响应范围，在 20 V 偏压下，其在 1080 nm 处最大响应度可达 1097.60 A/W，这是目前报道的具有最高响应的硅基光电探测器。同时，飞秒激光改性后合适的后处理过程有效地抑制了器件的暗电流（－5 V 偏压时为 7.8 μA），使该器件展现出非常优异的光电探测能力（在－5 V 偏压时的比探测率为 1.22×10^{14} Jones）。这一结果表明，优化后的飞秒激光改性硅基光电探测器在红外光检测，夜视成像和光纤通信中具有广阔的前景。

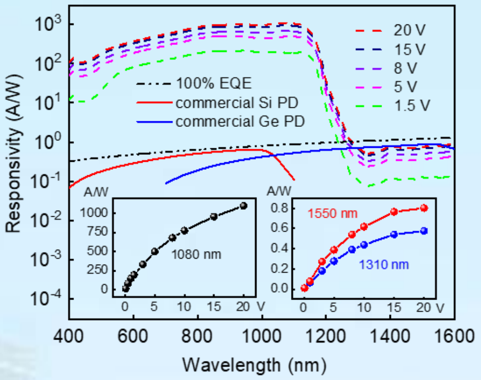

图 18. 黑硅光电探测器在不同反向偏压下的光电响应图，以及与商用硅、锗探测器的对比；黑硅器件在宽光谱范围内的外量子效率高于 100 %；插图为峰值响应度(左)和红外响应度(右)随偏压的变化曲线。

Fig. 18 Responsivities for a b-Si photodetector under different reverse bias voltages and comparison with commercial silicon and germanium photodetectors (PD). External quantum efficiencies (EQEs) over 100% are achieved for a wide waveband. The insets show the peak responsivity (left) and infrared responsivity (right) against bias voltage from 0.1 to 20 V.

表 1. 本文制备的黑硅光电探测器与部分前期报道典型器件的对比。

Table 1. Comparison of the key parameters of b-Si photodetectors reported here and the typical photodetectors reported earlier. waveband. The insets show the peak responsivity (left) and infrared responsivity (right) against bias voltage from 0.1 to 20 V.

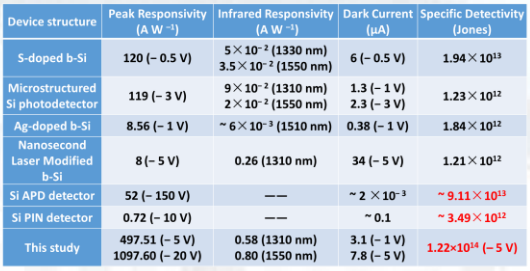

Device structure	Peak Responsivity (A W $^{-1}$)	Infrared Responsivity (A W $^{-1}$)	Dark Current (μA)	Specific Detectivity (Jones)
S-doped b-Si	120 (– 0.5 V)	5×10^{-2} (1330 nm) 3.5×10^{-2} (1550 nm)	6 (– 0.5 V)	1.94×10^{13}
Microstructured Si photodetector	119 (– 3 V)	9×10^{-2} (1310 nm) 2×10^{-2} (1550 nm)	1.3 (– 1 V) 2.3 (– 3 V)	1.23×10^{12}
Ag-doped b-Si	8.56 (– 1 V)	~ 6×10^{-3} (1510 nm)	0.38 (– 1 V)	1.84×10^{12}
Nanosecond Laser Modified b-Si	8 (– 5 V)	0.26 (1310 nm)	34 (– 5 V)	1.21×10^{12}
Si APD detector	52 (– 150 V)	——	~ 2×10^{-3}	~ 9.11×10^{13}
Si PIN detector	0.72 (– 10 V)	——	~ 0.1	~ 3.49×10^{12}
This study	497.51 (– 5 V) 1097.60 (– 20 V)	0.58 (1310 nm) 0.80 (1550 nm)	3.1 (– 1 V) 7.8 (– 5 V)	1.22×10^{14} (– 5 V)

Silicon-based photodetectors show attractive prospects due to their convenient preparation, high detectivity, and CMOS compatibility. However, they are currently limited by low responsivity and sharp decay at sub-bandgap wavelength. Although the aforementioned limitation can be partly solved by femtosecond laser processing, the surface defects and carrier activation rates result in a large dark current and narrow spectral response, which are unsatisfactory. Herein, rapid thermal annealing and hydrogenated surface passivation were introduced to elevate the broad-bandgap responsivity and signal to noise ratio and to suppress the dark current. At optimal conditions, a sub-bandgap responsivity of 0.80 A W–1 for 1550 nm at 20 V at room temperature was obtained, comparable with commercial germanium photodiodes and much higher than previously reported silicon photodiodes. Moreover, the prepared photodetector responded to spectral range from 400 to 1600 nm, with responsivity reaching 1097.60 A W–1 for 1080 nm at 20 V, which is the highest in reported silicon photodetectors. Simultaneously, the device showed competitive detectivity (1.22×10^{14} Jones at –5 V) due to the post-processing procedures and suppressed dark current (7.8 μA at –5 V). The results show great prospects for black silicon in infrared light detection, night vision imaging, and fiber-optic communication.

飞秒激光过饱和掺杂硅（通常又称为黑硅），因其从可见光到近红外波段宽的光谱高吸收和高响应特性，引起了人们的广泛关注。然而，由于黑硅层的不均匀性以及其中存在的大量晶格缺陷，因此，通过目前手段制备出的黑硅器件会不可避免地出现高噪声的缺陷，从而影响器件的综合性能。我们通过与 CMOS 兼容的制造工艺制备出具有横向异质结构的黑硅光电探测器，以此抑制器件的暗电流。横向异质结的结构使得黑硅光电探测器表现出显著的整流特性，在-5 V 偏压下，其暗电流为 783 nA，并且在光照后其在同样偏压下的光电流可以实现大约两到三个数量级的提升，从而表现出灵敏的光子响应度。在-5 V 偏压下，器件在 1080 nm 处的峰值响应度可达 3.23 A/W，对应的外量子效率（EQE）为 371%。凭借低噪声，高信噪比和高灵敏度的特性，这种横向异质结构可以实现黑硅光电探测器与光电子芯片或倒装芯片以及互连等系统的有机结合，在集成电路等领域具有广阔的应用前景。

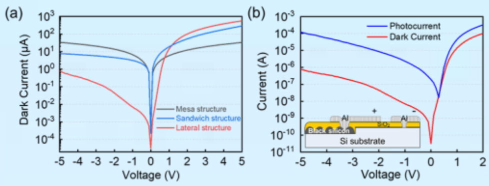

图 19. (a)具有横向结黑硅光电探测器的暗电流（红线），以及与两种垂直结构黑硅光电探测器的对比；以及(b)横向结黑硅光电探测器在按环境中以及在光照条件下的暗电流和光电流的对比。

Fig. 19 (a) Dark current characteristics of the b-Si devices having lateral heterojunction (red line) and two different photodetectors containing vertical heterojunction, and (b) I-V characteristics in the dark (red line) and under illumination (blue line) for the b-Si photodetector having lateral heterojunction.

Femtosecond laser hyperdoped silicon, known commonly as black silicon (b-Si), has attracted substantial interest from various fields due to its high absorptance and responsivity ranging from visible to near-infrared wavelengths. However, due to the non-uniformity of b-Si layer and the lattice defects present in it, the processing technique used presently introduces high noise in devices manufactured using b-Si. In this study, a lateral heterojunction is designed and manufactured at the b-Si and silicon interface to restrain the leakage current. Precisely, the lateral structure could support the b-Si photodetector in suppressing the dark current to 783 nA at a bias of -5 V, quite low in terms of orders of magnitude compared to that for the vertical ones. Simultaneously, the photo-to-dark current ratio of 155 is obtained at the same bias voltage with a pertinent external quantum efficiency (EQE) of 371%. Riding on the advantages of low noise, high signal-to-noise ratio, and high sensitivity, this work shows promising prospects for the application of b-Si-based photodetectors toward large-scale integration in optical-electronics or flip-chip interconnection systems.

尽管过饱和掺杂硅具有出色的红外吸收能力，但它在硅基探测方面的应用仍然面临一些问题。过饱和掺杂的同时，不可避免会有大量缺陷和损伤进入硅中，这会严重地破坏晶格结构。这些缺陷形成了高密度的复合中心，并由此产生了内部漏电流，这大大降低了探测器的响应度并增加了暗电流，使器件整体性能下降。迄今为止，一些研究致力于改善过饱和掺杂硅的结晶度，包括飞秒激光辐照后热退火、离子注入后退火、以及过饱和硫氮共掺。然而，样品中仍然会形成缺陷和位错，从而阻碍了过饱和掺杂的工业化应用。我们报道了一种改进方法，该方法在飞秒激光辐照期间提高硅衬底的温度，可以制造出高响应性的 Te 过饱和掺杂黑硅光电二极管。硅衬底的温度升高，样品表面可以形成具有单晶性过饱和掺杂层的均匀表面微结构，这有助于增强器件的光响应和稳定性。据我们所知，在 700 K 下制备的 n-n+黑硅光电二极管，经过退火后，在 1120 nm 的响应率为 120.6 A/W，这是目前报道过的掺 Te 的硅基光电二极管的最高响应度。不仅如此，在 1300 nm 和 1550 nm 处的带隙响应度分别为 43.9 mA/W 和 56.8 mA/W，而且器件噪声较小，这对于光通信和光互连中硅基器件的应用很有意义。我们的研究为硅基探测器的发展提供了新的思路。

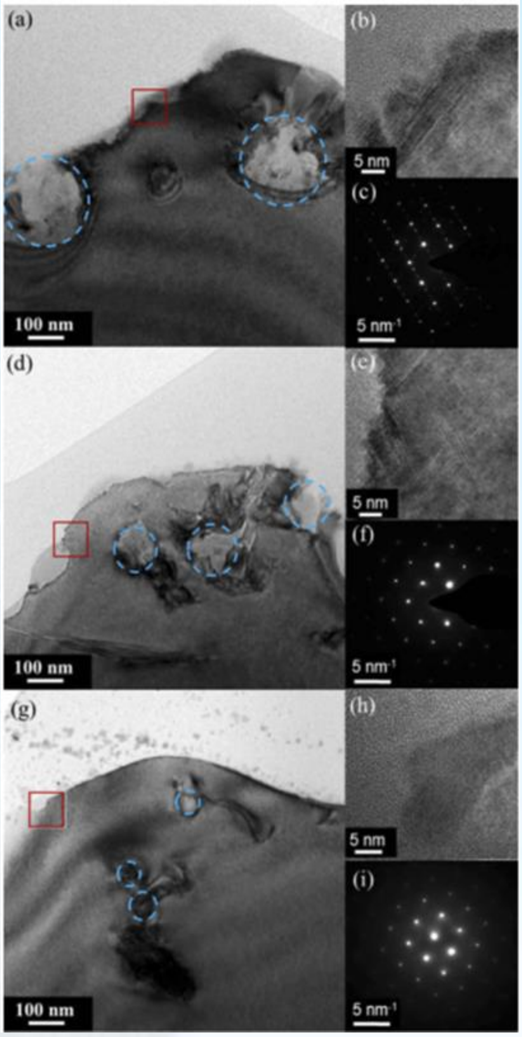

图 20. 不同基底温度(a)-(c)300 K，(d)-(f)500 K，和(g)-(i)700 K 过饱和掺杂硅表面上带有气泡（蓝色虚线圆）的单个熔滴结构的截面 TEM 图像，熔滴边界上的凹坑（红色正方形）的高分辨率 TEM 图像，以及 SAED 图案。

Fig. 20 Overview cross-sectional TEM images of a single droplet on the hyperdoped silicon surface with bubbles (blue dashed round), high-resolution TEM images of a pothole on the droplet boundary (red square), and the SAED pattern of the surface of the Te-hyperdoped silicon at different substrate temperatures: (a)-(c)300 K, (d)-(f)500 K, and (g)-(i)700 K.

Despite the excellent IR absorption, the application of hyperdoped silicon in silicon-based detections still faces some problems. Inevitably, the crystal lattice is extremely damaged by a high concentration of undesirable defects and damages incorporated into the silicon. These defects induce a high density of recombination centers and the resultant internal leakage, which greatly reduce the responsivity and increase the dark current of the device. To date, several studies were devoted to improving the crystallinity of hyperdoped silicon. The approaches included femtosecond laser irradiation followed by thermal annealing, ion implantation followed by proper annealing, and the co-doping of supersaturated nitrogen and sulfur. Nevertheless, defects and dislocations still formed in the sample, thereby hindering the industrialization.

由于光信息处理具有天然的并行优势，光子芯片可实现更快、更安全、更高效的信息处理和传送速度，光计算被认为是最有希望替代电计算的未来技术。但实现光子芯片的首要任务是像操纵电子那样在纳米尺度下上实现光子行为的操控，这依赖于材料的非线性光学效应。为了寻找合适的材料，首先需要对微纳材料非线性张量进行完备测量。但由于微纳材料中光程远小于非线性相干长度，使得现有的技术（如马克条纹法、尖劈法等）难于完成这一任务。为解决该问题，我们发明了一种新型的微纳材料二阶非线性测量技术(PolariSH)，突破了传统技术的限制，成功对于宽光谱波段铌酸锂纳米薄膜二阶非线性系数各张量元的实部与虚部进行完备测量，为铌酸锂微纳非线性研究奠定了参数与技术基础。【Opt. Lett., 45, 145 (2020)】

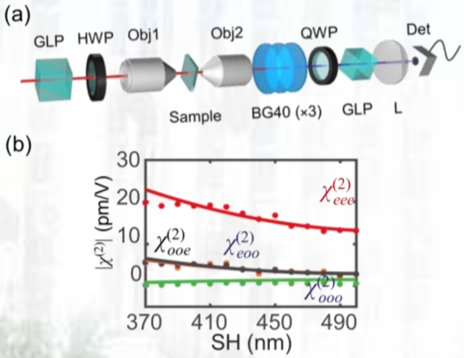

图 17. (a) PolariSH 系统示意图；(b) 铌酸锂二阶非线性张量元。

Fig. 17 (a) A schematic of PolariSH system. (b) Experiemntally measured second-order nonlinear susceptibility elements of lithium niobate.

Since optical information processing has a natural parallel advantage, photonic chips can achieve faster, safer, and more efficient information processing and transmission speed. Optical computing is considered to be the most promising future technology to replace electrical computing. But the primary task of realizing a photonic chip is to realize the manipulation of photon behavior at the nanometer scale like manipulating electrons, which relies on the nonlinear optical effect of the material. In order to find a suitable material, a complete measurement of the nonlinear tensor of micro-nano materials is first required. However, since the optical path in micro-nano materials is much smaller than the nonlinear coherence length, it is difficult for the existing technologies (such as the Mark fringe method and the wedge method) to accomplish this task. In order to solve this problem, we invented a new type of second-order nonlinear measurement technology for micro-nano materials (PolariSH), which overcomes the limitations of traditional technology and successfully measured the tensor elements of the second-order nonlinear coefficients of lithium niobate nano-thin films in a wide spectral range. The complete measurement of the real and imaginary parts of lithium niobate lays a parameter and technical foundation for the researches for the lithium niobate micro/nano devices in future.

我们发展了一种在 LNOI 上制备高精度、复杂畴结构的纳米探针极化工艺，可以实现尺寸小于 100 nm 的畴结构的制备。我们将该工艺应用于周期极化铌酸锂微纳光学器件的制备，结合紫外光刻和离子束刻蚀技术实现了片上单/双周期极化铌酸锂微盘腔的制备。通过双周期极化结构引入的丰富的空间波矢，在周期极化铌酸锂微腔中同时实现了多个非线性过程的准相位匹配。实验上，首次在单周期极化铌酸锂微盘腔中实现了

铌酸锂晶体最大非线性系数 d_{33} 参与的二次谐波转换效应 [Photonics Res. 8, 311-317 (2020)]和基于双周期极化铌酸锂微腔的高次谐波转换效应，其中，二次谐波转换效率最高为 51 %W^{-1} [Opt. Lett. 45, 3353-3356 (2020)]。为新型光源的制备和光通讯等应用奠定了重要基础。

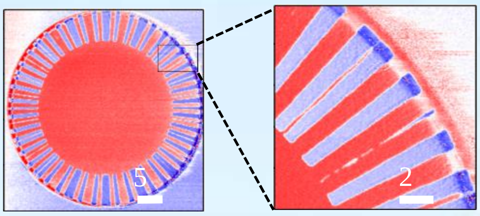

图24. 双周期极化铌酸锂微腔压电力显微镜照片，蓝色区域为极化反转微结构。

Fig. 24 The piezoresponse force microscopy pictures of dual PPLN microstructures, the blue areas represent the areas whose polarization was reversed.

We developed a method to fabricate high-precision and complicated domain patterns on LNOI with the assistance of nano-probs, which allows us to obtain a domain unit down to the scale of 100 nm. Combining with UV light photolithography and reactive ion etching, we applied the aforementioned method to periodically poled lithium niobate (PPLN) micro-structures and fabricate single/dual-period PPLN microdisk resonators. Quasi phase matching conditions for multi frequency conversion processes were achieved in PPLN microdisk resonators simultaneously, benefiting from the abundant wave vectors provided by the micro-structures with dual spatial periods. Second harmonic generation (SHG) using d_{33}, the largest nonlinear coefficient of LN, was achieved in a PPLN micro-disk with a single period for the first time [Photonics Res. 8, 311-317 (2020)]. High order harmonic generations were observed in PPLN microdisks with dual spatial periods, and the highest conversion efficiency of SHG was measured to be 51% W^{-1} [Opt. Lett. 45, 3353-3356 (2020)].

非线性物理与光子技术/ Nonlinear Physics and Photonics Techniques

负责人：田建国

本年度发表论文 18 篇，在非线性物理与光子技术方向主要取得了以下进展：

18 papers have been published in international academic journals. This year, we obtained some important results as following:

(1) 基于外尔超材料的螺旋费米弧与涡旋反射。传统涡旋光束的产生依赖于随空间变化的相位元，如液晶 q 玻片、空间光调制器和超表面，包括 Pancharatna-Berry 相位型超表面，利用亚波长各向异性的相位元在自旋翻转圆偏振态上施加额外的相位。这些器件在实空间中均含有非均匀的图样，因此要求入射光束严格对准相位分布的几何中心。在本工作中，自旋极化的平面电磁波通过光子外尔系统反射，实现了动量空间中的涡旋相位分布。涡旋光的拓扑荷与入射光的偏振态有关，即右旋光入射生成左旋二阶涡旋光，左旋光入射直接转换为右旋光。应用外尔点拓扑性质的这一关键特征来产生涡旋光束，光束可入射到外尔系统表面的任意位置，不需要像传统方法那样进行相位对准，这有效地简化了涡旋光的生成。进一步，我们将外尔超材料和金属平板构成杂化型波导系统，在动量空间中发现了一种新型的螺旋波导模式，这种螺旋形的波导模式是由动量空间中的旋涡相位产生，成为连接不同外尔点的螺旋形费米弧；通过改变工作波长，可以有效地调节费米弧的螺旋线型与螺旋圈数。此研究结果有望推动光子外尔系统在自由空间和波导系统中对电磁波角动量操控的新应用。 [Phys. Rev. Lett. 125, 093904 (2020) (Editors' Suggestion)]

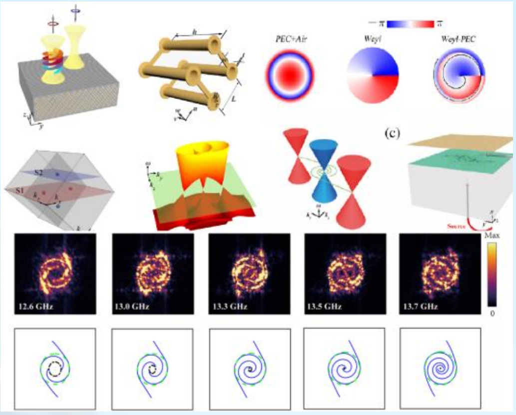

图 1. 三维外尔超材料原理图与实验观察到的螺旋费米弧。

Fig. 1 Schematic diagram of three-dimensional Weyl metamaterials and the experimental results of the spiraling Fermi arcs.

Scatterings and transport in Weyl semimetals have caught growing attention in condensed matter physics, with observables including chiral zero modes and the associated magnetoresistance and chiral magnetic effects. Measurement of electrical conductance is usually performed in these studies, which, however, cannot resolve the momentum of electrons, preventing direct observation of the phase singularities in scattering matrix associated with Weyl point. We experimentally demonstrate a helical phase distribution in the angle (momentum) resolved scattering matrix of electromagnetic waves in a photonic Weyl metamaterial. It further leads to spiraling Fermi arcs in an air gap sandwiched between a Weyl metamaterial and a metal plate. Benefiting from the alignment-free feature of angular vortical reflection, our findings establish a new platform in manipulating optical angular momenta with photonic Weyl systems.

(2) 基于超构透镜阵列的三维高精度定位。利用光学手段实现物体的三维高精度定位是现代光学雷达和视觉传感等技术的基础，在相机、显微镜、自动驾驶、增强现实

等领域也有重要应用。然而目前的光学定位系统大都需要较大的体积且难以校正像差。近年来，基于超构表面的透镜设计吸引了越来越多研究者的兴趣。相对于传统的光学透镜，超构透镜具有体积小、易集成、易调控、调控自由度更丰富等优点，非常适合用来实现小型化的光学定位系统。我们提出了一种单层超构表面透镜阵列设计，利用不同超构透镜空间位置信息的不同，首次在人工微结构系统实现了被成像物体的三维高精度定位，定位精度达 0.60%−1.31%。同时，通过采用图像梯度下降算法，将不同子图像的图像信息进行筛选结合，有效地消除了透镜固有的成像像差，进而提高成像视场至49.6°。这种消除像差的方法不需要引入复杂的透镜设计以及多层消像差设计，从而极大地简化了加工制备过程。此外，我们还验证了所提出的透镜阵列对于入射光偏振态不依赖的特性，这对于基于被动照明式任意物体的空间定位具有明显意义。 [Optica 7, 1706 (2020).]

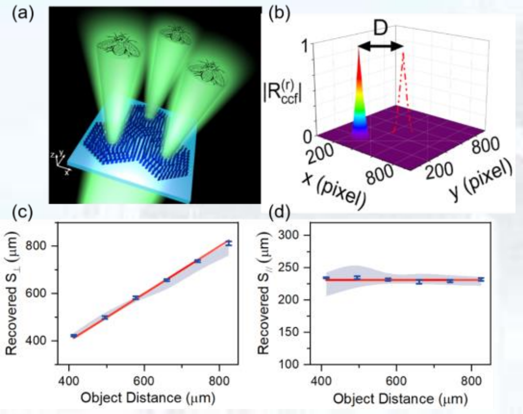

图 2. (a) 三维定位超透镜阵列示意图；(b) 利用互相关函数确定子图像间特征参量；(c,d) 实验测量的(c)纵向与(d)横向定位结果，灰色区域为未经过算法校正的结果。

Fig. 2 (a) Schematic of the ideal metalens array. (b) Determination of the characteristic parameters between sub-images by using the cross-correlation function. (c, d) Experimental results of the three-dimensional positioning.

Three-dimensional (3D) positioning with the correction of imaging aberrations in the photonic platform remains challenging. We combine techniques from nanophotonics and machine vision to significantly improve the imaging and positioning performance. We use a titanium dioxide metalens array operating in the visible region to realize multipole imaging and introduce a cross-correlation-based gradient descent algorithm to analyze the intensity distribution in the image plane. This corrects the monochromatic aberrations to improve the imaging quality. Analysis of the two-dimensional aberration-corrected information in the image plane enables the 3D coordinates of the object to be determined with a measured relative accuracy of 0.60%–1.31%. We also demonstrate the effectiveness of the metalens array for arbitrary incident polarization states. Our approach is single-shot, compact, aberration-corrected, polarization-insensitive, and paves the way for future integrated photonic robotic vision systems and intelligent sensing platforms that are feasible on the submillimeter scale, such as face recognition, autonomous vehicles, microrobots, and wearable intelligent devices.

(3) 基于手性镜子的自旋选择光场全维度操控技术。提出了一种手性镜子的系统性设计方法，实现了对光场的自旋选择全维度独立操控。我们首先设计并实验验证了两种手性光学响应相反的手性镜子，证明了其在谐振波长下可以分别实现对左旋圆偏振光场和右旋圆偏振光场的自旋选择反射，且对两种圆偏振光场的反射差高于 78%。通过定性和定量理论分析，我们阐述了所提出的手性镜子中光场的自旋选择反射产生的物理机理——铝制纳米结构中偶阶共振模式的自旋选择激发：即在谐振波长处特定圆偏振光波入射下，所提出的手性镜子结构单元中铝制纳米结构内部会产生一对方向相反的电流抑制光场的反射。基于该物理机制，我们进一步证明了通过对所提出的手性镜子的三个结构变量的独立控制，就能够实现对特定圆偏振光场的反射振幅，相位在谐振波长下的完全控制，且谐振波长可以在宽谱段上被连续调整。我们还通过实验证明了所提出的手性镜子可以被应用于手性光学防伪，

手性灰度成像和自旋态探测等领域。所提出的手性镜子克服了手性镜子研究领域先前工作中的一些缺点，在宽波段范围内实现了对特定圆偏振光场反射强度和谐振波长的任意设计，为光场自旋选择全维度独立操控的实现提供了一种可行的方式。[Adv. Mater. 32, 1907983 (2020)]

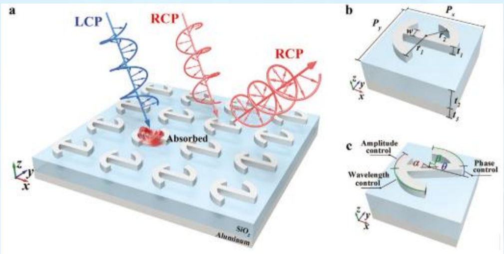

图 3. 基于手性镜子的自旋选择光场多维度操控示意图。

Fig. 3 Schematic illustrating the realization of the full-dimensional manipulation of circular-polarized waves based on the designed chiral mirror.

Realizing arbitrary manipulation of optical waves, which still remains a challenge, plays a key role in the implementation of optical devices with on-demand functionalities. However, it is hard to independently manipulate multiple dimensions of optical waves because the optical dimensions are basically associated with each other when adjusting the optical response of the devices. In our research, the concise design principle of a chiral mirror is utilized to realize the full-dimensional independent manipulation of circular-polarized waves. By simply changing three structural variables of the chiral mirror, the proposed design principle can arbitrarily and independently empower the spin-selective manipulation of amplitude, phase, and operation wavelength of circular-polarized waves with a large modulation depth. This approach provides a simple solution for the realization of spin-selective full-dimensional manipulation of optical waves and shows ample application possibilities in the areas of optical encryption, imaging, and detection.

(4) 提出了多路复用非衍射非线性超表面。贝塞尔光束和艾里光束等非衍射波束在自由空间传播时可具有不变的横向强度面，因此在需要小发散角、长工作距离和高稳定性的光学系统中具有很高的应用价值。传统的利用锥透镜来产生贝塞尔光束的方法难以产生大数值孔径的贝塞尔光束，而利用具有环形孔的透镜对来产生贝塞尔光束的方法一般效率较低。传统的产生艾里光束的方法是基于空间光调制器和傅里叶转换系统，一般体积较大并且不易精确控制。利用超表面来产生和调控非衍射光束是近几年光学领域的研究热点之一，超表面的超薄厚度与亚波长尺度优势有望实现超紧凑的非衍射光束产生器，超表面较强的相位调控和振幅调控能力有助于实现高效、大数值孔径的非衍射光束。但目前的可产生非衍射光束的超表面大都是在线性光学系统中实现的，因此它们的工作通道数目被大大限制了。我们设计并从实验上验证了一种可产生非线性非衍射光束的超表面，该超表面可以分别在基频和二倍频波长下产生三种不同数值孔径和不同拓扑荷数的贝塞尔光束。另外，通过引入非线性信号，还可以同时产生三种具有不同传播曲线和焦距的艾里光束。产生的每一种衍射光束只能通过特定的波长和自旋组合来读取，这使得利用这些不同的衍射光束通道来进行信息的多路复用成为可能。我们还发现利用傅里叶分析方法来研究这些非衍射光束可以更全面、简洁地描述其复杂性质，并且我们从实验上，通过探测透镜焦平面上的光场获得了各种非衍射光束的性质，进一步验证了我们提出的傅里叶分析方法的正确性。除此之外，我们还利用两束对称艾里光束的相干叠加产生了突然自聚焦光束。我们的研究为贝塞尔光束和艾里光束等非衍射光束的多路复用提供了新的方法，有望应用于光通讯、多层细胞操纵和大视场生物成像等领域。[Adv. Funct. Mater. 30, 1910744 (2020)]

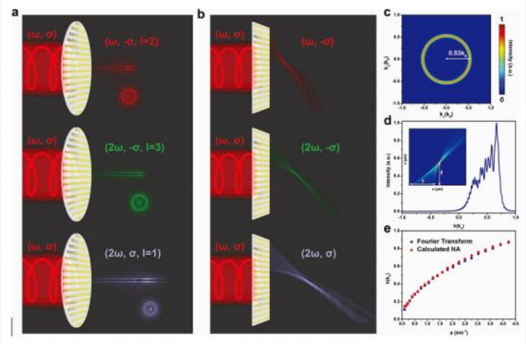

图 4. 多路复用非衍射非线性超表面示意图。

Fig. 4 Schematic of the multiplexed nondiffracting nonlinear metasurfaces.

Metasurfaces and planar photonic nanostructures have drawn great interest from the optical scientific community due to their diverse abilities of manipulating electromagnetic waves and high integration. Most metasurfaces launch diffracting waves, and thus suffer from divergence, short working distance, and instability. Although much effort has been devoted to researching nondiffracting metasurfaces which can launch electromagnetic waves with constant transverse intensity profiles in free-space propagation, the number of working channels is inherently limited as these meta-devices are implemented in the linear optical regime. In our research, the multiplexed nondiffracting nonlinear metasurfaces are theoretically proposed and experimentally realized, which can generate the representative nondiffracting Bessel beam and Airy beam. Three Bessel beams with different numerical apertures and topological charges and three Airy beams with different propagation curves and focal lengths can be generated by a combination of different spins and wavelengths. The complex properties of the nondiffracting beams can be designed and detected in a more comprehensive and concise way with Fourier analysis. This proof-of-concept represents a new strategy for realizing multiplexed nondiffracting metasurfaces with advantages of ultracompactness, high-pixelation, and easy integration and paves the way for multi-channel optical communication and manipulation.

(5) 基于二维材料的多功能范德瓦尔斯异质结电子器件在未来的纳米电子学领域中具有重要的应用潜力。我们利用激光直写微纳加工技术在同一预制备的黑磷/二硫化钼异质结构上实现了多功能的范德瓦尔斯异质结器件功能，包括二极管、NPN 型与 PNP 型三极管。相比设计复杂的器件结构与化学刻蚀方法，该技术具有快速、灵活、环境友好与通用的优势。不仅三个二极管均展示出典型的电学整流行为，同时两个三极管也表现出良好的电流放大输出性能，对于 NPN 型和 PNP 型，放大增益分别为 41 和 12。此外，我们还从器件结构以及激光直写加工的角度系统分析了两种类型三极管的性能差异。在相同激光直写加工宽度条件下，由于黑磷和二硫化钼的载流子浓度不同，NPN 型三极管表现出更好的放大性能。同时，三极管的放大增益可由激光直写可调的基区宽度进行有效调制。实验结果表明，电流增益会随基区宽度的增大而减小，这一点与理论结果也相吻合。这种激光直写微纳加工的方法对于实现二维材料大规模集成电路也具有广阔的应用前景。

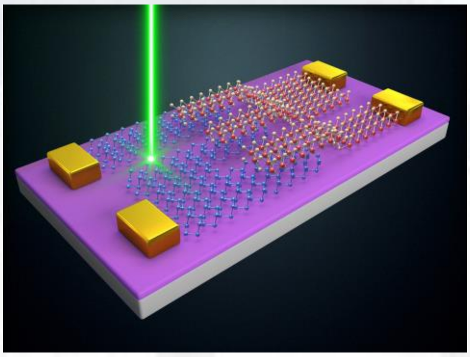

图 5. 激光可写多功能范德瓦尔斯异质结示意图。

Fig. 5 laser writable multifunctional van der Waals heterostructures

Multifunctional van der Waals heterostructure electronic devices based on two dimensional (2D) materials have great application potential in the future nanoelectronics. We have utilized laser write processing (LWP) technique to fabricate three diodes and NPN (PNP) bipolar junction transistor (BJT) simultaneously on a single pre-fabricated black phosphorus/molybdenum disulfide (BP/MoS_2) heterostructure. Compare with the complex device architectural designs and chemical etching method, this LWP technique holds the advantages of being fast, flexible, environmentally friendly and universal. The three diodes exhibited typical electrical rectification performance and both BJTs (NPN and PNP) rendered good current amplification output with a common-emitter current gain (β) of $\approx$ 41 and 12, respectively. Then, we have systematically analyzed the performance difference between NPN and PNP BJT from the viewpoints of structure and LWP. Owing to the difference in carrier concentration of BP and MoS_2, the NPN BJT shows better performance than the PNP BJT under the same LWP width. Furthermore, the current gain can be effectively modulated through the tunable base width of laser writing. Herein, the current gain decreased with the increase of base width, which is consistent with the theoretical results. The proposed LWP approach exhibits promise for large-scale integrated circuits based on 2D heterostructures.

(6) 二维材料堆叠技术是包括二维材料的制备、转移、堆叠、转角等一系列操作在内的纳米加工技术。这类技术突破了单一材料的性能限制，为二维材料的研究带来了新的维度，我们总结概括了近年来二维材料堆叠技术的研究进展。其中包括改良的机械剥离法、反应刻蚀减薄法、化学气相沉积法、液相剥离法等高质量二维材料制备技术，同时还介绍了干/湿法转移、微区堆叠、高精度角度控制、超净表面处理、深度机器学习与自动化组装等二维材料堆叠结构加工技术。此外文章还归纳总结了 2D-0D、2D-1D 和2D-3D的二维材料混合维堆叠结构在不同领域的应用。同时我们的研究指出，二维材料堆叠技术目前存在着重复性差、操作繁琐、过于依赖人工经验等不足，同时面临着纳米级别定点转移、小于 0.01°的角度控制、全自动化生产等挑战。未来，如何实现高质量，高精度，和高效率的样品制备将是堆叠技术研究的重点。

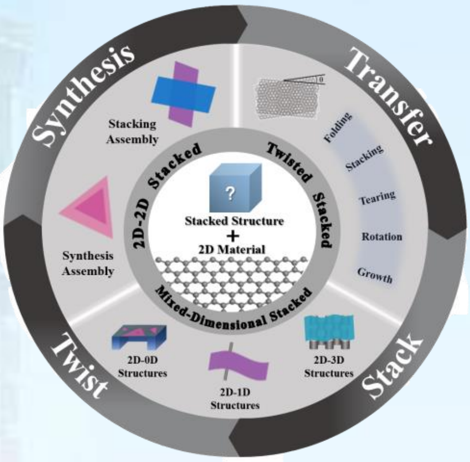

图 6. 二维材料堆叠技术汇总。

Fig. 6 Summary of two-dimensional material stacking technology

2D (Two-dimensional) material stacking technology is a nano-processing technology that includes a series of operations such as preparation, transfer, stacking, and cornering of 2D materials. This type of technology breaks through the performance limitations of a single material and brings a new dimension to the research of 2D materials. We summarized the research progress of 2D material stacking technology in recent years. Including improved mechanical stripping method, reactive etching thinning method, chemical vapor deposition method, liquid phase stripping method and other high-quality 2D material preparation technology, but also introduced dry/wet transfer, micro-area stacking, high-precision angle Control, ultra-clean surface treatment, deep machine learning and automatic assembly and other 2D material stack structure processing technology. In addition, the article also summarized the application of mixed-dimensional (2D-0D, 2D-1D, 2D-3D) stacked structure in different fields. At the same time, our research points out that the 2D material stacking technology currently has disadvantages such as poor repeatability, cumbersome operation, and excessive reliance on manual experience. At the same time, it faces challenges such as nano-level fixed-point transfer, angle control less than 0.01°, and fully automated production. In the future, how to achieve high-quality, high-precision, and high-efficiency sample preparation will be the focus of stacking technology research.

(7) 施加的应变会导致石墨烯的碳-碳键发生重大变化，从而形成电子超晶格。这些超晶格内的电子/声子耦合和伪规范场的存在赋予其独特的电子和磁性特性。然而，很少研究过应变和原始石墨烯之间的界面相互作用。本文中，我们报道了在原始石墨烯与应变诱导的超晶格即石墨烯皱纹之间的界面处的光电流显着增加。光电流分布表明石墨烯的弯曲晶格大大增加。这些结果表明，光电流的增强是由于原始石墨烯和变形的超晶格之间的塞贝克系数不同，导致界面处的光热电效应显着增加。

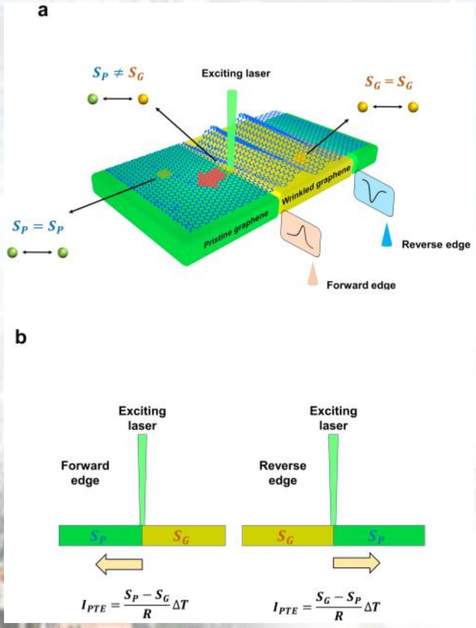

图 7. 褶皱区域的塞贝克系数变化与光电响应增强。

Fig. 7 Mechanism of photocurrent enhancement due to the difference in Seebeck coefficient between pristine graphene and GWSL.

Applied strain introduces significant changes in the carbon-carbon bond of graphene and, thereby, forms electronic superlattices. The electron/phonon coupling and existence of pseudo-gauge fields within these superlattices render unique electronic and magnetism properties. However, the interfacial interactions between strained and pristine graphene have rarely been studied. Herein, we report a prominent increase in photocurrent at the interface between pristine graphene and strain-induced superlattice, i.e., graphene wrinkle. The photocurrent distribution indicates a large increase in the bending lattice of graphene. These results demonstrate that the photocurrent enhancement is due to the difference in Seebeck coefficient between pristine graphene and deformed superlattices, resulting in a significant increase in photothermoelectric effect at the interface.

(8) 我们将微流控装置与具有良好稳定性的 DNA 纳米结构与组装在一起，实现了低浓度 DNA 样品的特异性捕获。DNA 纳米材料较差的稳定性和可操作性严重阻碍了其应用的进一步发展。之前的研究中，我们提出了一种热稳定的 DNA 纳米网状结构。然而，基于离心管的过滤装置捕获目标生物分子时，在灵敏度和可操作性方面还存在一些不足。我们将该 DNA 纳米结构集成到微流控芯片中制成一种特异性核酸捕获装置。在捕获单链 DNA 样品时，该装置的特异性提高到了单碱基水平。微流控芯片为 DNA 纳米结构提供了一个封闭的环境，使装置具有良好的储存稳定性。在室温下存放 6 个月后，该装置对浓度低至 1pM 的 ssDNA 样品仍具有良好的特异性的捕获功能。该特异性核酸捕获装置可应用于 ctDNA 的富集，有助于癌症的早期诊断。

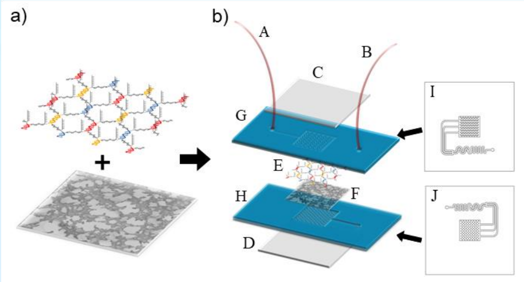

Fig. 8 The structure of the P-mesh microfluidic capture device. a) The PVDF membrane combined with P-mesh. b) The details of the P-mesh microfluidic capture device. A, B: PVC microbore tube; C, D: glass slide; E: P-mesh; F: PVDF membrane; G: top PDMS microchannel layer; H: bottom layer; I: channel of G; J: channel of H.

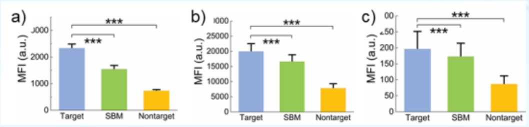

Fig. 9 a) MFI percentage of 1uM Cy5-labeled ssDNA captured by the P-mesh microfluidic capture device. b) MFI percentage of 1uM Cy5-labeled ssDNA captured by the P-mesh microfluidic capture device after storage over 6 months. c) MFI percentage of 1pM Cy5-labeled ssDNA captured by the P-mesh microfluidic capture device after storage over 6 months.

We assembled the microfluidic device and DNA nanostructures with good stability to achieve the specific capture of low concentration DNA samples. The poor stability and operability severely impede further development of the application of DNA nanomaterials. A thermally stable DNA nanomesh structure was proposed in our previous study. However, when capturing the target biomolecules, the centrifugal tube filter device still has some shortcomings in sensitivity and operability. Here, the DNA nanomesh is integrated into the microfluidic chip. The specificity of microfluidic DNA specific capture device was improved to the single base mismatch level while capturing the ssDNA sample. The microfluidic chip provides a closed environment for DNA nanomesh, make the device has excellent storage stability. After 6 months of storage at room temperature, the device still has a specific capture function on ssDNA sample with the concentration as low as 1pM. The microfluidic DNA specific capture device can apply to the enrichment of ctDNA in the future and contribute to the early diagnosis of cancer.

(9) 我们组建了一套可以实时进行多通道测量的装置，可以检测光子胶体晶体传感器形成的德拜衍射环偏移量。其原理是在传感器收到外界环境变化刺激时，衍射环出现偏移，我们采用线阵 CCD 进行衍射环偏移量的实时测量。我们用盘尼西林及其抑制剂的相关实验进行了验证，与已有的检测装置相比，这种方法可以进行实时的多通道测量，且成本低，是一种可以实用化的检测装置。

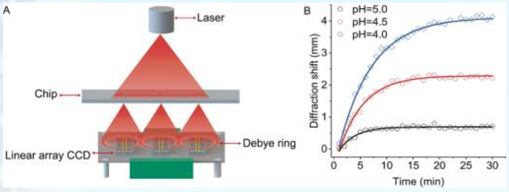

Fig. 10 (A) Schematic illustration of the optical device for multichannel measurement of the Debye diffraction ring shift of the 2D PCCH sensors. (B) The representative time-responsive Debye diffraction ring shift of the PCCH films at different pH.

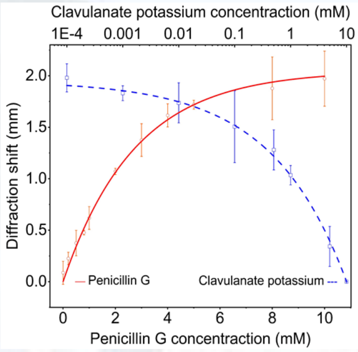

Fig. 11 The Debye diffraction ring shift the penicillinase-decorated PCCH sensor for detection of penicillin G (solid line; red) and clavulanate potassium (dotted line; blue).

We demonstrate real-time and multi-channel measurement of Debye diffraction ring shift of two-dimensional (2D) photonic colloidal crystal hydrogel (PCCH) sensors with a homebuilt portable and digital optical device for the first time. The principle is based on real-time measurement of the positional movement of the Debye diffraction ring with a linear charge coupled device (CCD), which can be employed to determine the diffraction shift of the 2D PCCH film upon external environmental stimuli. We demonstrate excel-lent performance of the optical device by employing detection of penicillinase and its inhibitor clavulanate potassium as an example. Compared to the existing methods used in 2D PCCH sensors, this method takes advantages of cost-effective instrumentation, real-time measurement, digitized signal output, and multiplex detection. Therefore, it has great potential in practical applications of 2D PCCH sensors.

光子学材料及先进制备技术/ Photonics Materials and Advanced Fabrication Techniques

负责人：孔勇发

本方向涉及多功能光学晶体、低维功能材料、软物质、微晶陶瓷、光子学微结构等光子学材料及原位 4D 超快电子显微镜技术等方面。本年度发表论文 19 篇；授权专利 3 项。在研课题经费 1749.54 万元。2020 年度“光子学材料及先进制备技术”方向主要在以下方面取得了进展：

In this field, we mainly focused on the development of multi-functional optical crystals, low dimensional functional materials, soft materials, microcrystalline ceramics, optical microstructures and other optoelectronic materials, as well as 4D ultra-fast electron microscopy technique. 19 papers have been published in international academic journals, and 3 authorized patents were published. The total researching founds are 17.50 million. This year, we obtained some important results as following:

课题组对近期铌酸锂（$LiNbO_3$, LN）在光折变和基片集成等方面的工作进行了总结综述，并发表在 ***Adavanced Materials*** 上。近年来课题组发现通过掺杂调控可以有效地将铌酸锂晶体的可见光抗光损伤阈值提高 4~6 个数量级，同时发现了具有紫外抗光损伤性能的 LN:Zr 晶体。通过第一性原理模拟了铌酸锂晶体本征和非本征缺陷与掺杂离子的相互作用和影响。文章综述了近期引起广泛关注的 LNOI 材料的进展，包括其制备、电光、非线性。

The research group summarized the recent work of Lithium Niobate ($LiNbO_3$, LN) in photorefractive and substrate integration, and published it on ***Advanced Materials***. In recent years, the research group found that the visible optical damage threshold of $LiNbO_3$ crystal can be effectively increased by 4 ~ 6 orders of magnitude by doping control, and LN:Zr crystal with UV optical damage resistance was found. The interaction and influence of intrinsic and extrinsic defects with doped ions in $LiNbO_3$ crystal are simulated from first-principles calculations. This article also reviews the recent development of LNOI materials, including its preparation, electro-optic and nonlinear.

课题组利用第一性原理研究了高价掺杂铌酸锂晶体的缺陷结构，其中掺氮铌酸锂的研究结果表明氮原子以最低的缺陷形成能取代氧位并形成最稳定的晶格结构，对电子结构的研究结果表明氮在靠近价带顶的位置形成了两条能级，其主要由氮的 p 电子和氧的 p 电子构成，为空穴载流子的传输提供了证据。该工作被选为 PCCP 当期封面。

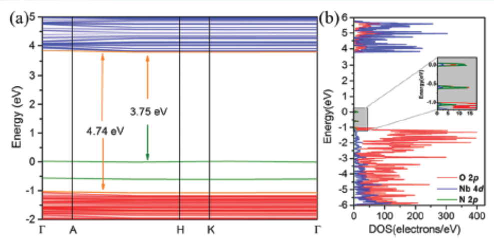

图 1. (a) 用 HSE06 计算 LN:N 的能带结构。从导带底到价带顶和新能级的能量分别为 4.74 eV 和 3.75 eV。(b) LN:N 中不同单原子态（包括 O 2p，Nb 4d 和 N 2p）的分态密度图。

Fig.1 (a) Band structure of LN:N calculated with HSE06. The energies from the CBM to the VBM and the new energy levels are 4.74 eV and 3.75 eV respectively. (b) PDOS of the main single atomic states including O 2p, Nb 4d, and N 2p with an amplified region of impurity states in the band gap of LN:N.

The defect structure of high valence doped lithium niobate crystal was studied by first principles. The research results of nitrogen doped lithium niobate show that nitrogen atom can replace oxygen ions with the lowest defect and form the most stable lattice structure. The research results of electronic structure show that nitrogen forms two energy levels near the top of valence band, which are mainly composed of p-electrons of nitrogen and p-electrons of oxygen It provides evidence for the transport of hole carriers. This work is selected as the current front cover of *PCCP*.

近年来，高通量计算和材料基因组方法的迅速发展，提高了研究人员设计先进材料的能力。晶体结构预测技术在高通量计算和材料基因组方法中发挥着重要作用。本文从 Pauling 规则中提取了一套简便的晶体结构构造操作指南。基于这一组准则，我们设计了一个叫做 Pauling's rules guided Monte Carlo search（PAMCARS）的算法，它通过结合经典 montecarlo 搜索和从头算结构弛豫，预测给定成分的基态和亚稳态无机晶体结构。在实际测试中，该算法成功地预测了碳同素异形体 $CaSO_4$、$Ba_2TiSi_2O_8$ 和 $BaAlBO_3F_2$ 的晶体结构。此外，还预测了一些尚未报道的碳、$CaSO_4$ 和 $Ba_2TiSi_2O_8$ 的高对称亚稳晶体结构。对石墨层的成功预测表明，PAMCARS 能够预测由范德华力组装的某些层状材料。$Ba_2TiSi_2O_8$ 低能亚稳晶体结构中的两个可能解释了 $Ba_2TiSi_2O_8$ 在 160℃左右的性质异常。Pauling 规则引导的 montecarlo 搜索在预测实验中的基态和亚稳晶体结构方面具有较高的效率和能量分辨率。

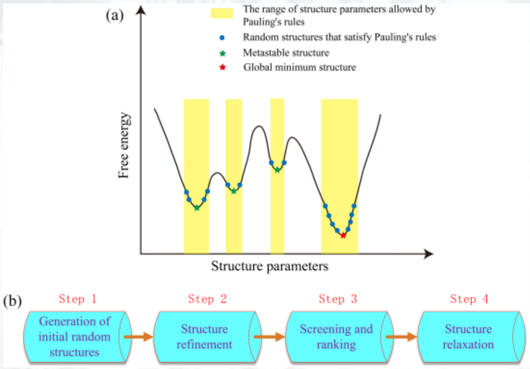

图 2. (a) 满足泡林规则的随机结构在晶体典型能量场中的分布。代表亚稳态结构的局部极小值和代表基态结构的全局极小值的位置被标记在能量景观上。满足 Pauling 规则的随机结构分布在极小值附近。(b) 保林规则的四个主要步骤指导蒙特卡罗搜索。

Fig.2 (a) The distribution of the random structures satisfying Pauling’s rules in a typical energy landscape of a crystal. The locations of the local minimums representing metastable structures and the global minimum representing ground-state structure are marked on the energy landscape. Random structures satisfying Pauling’s rules are distributed near the minimums. (b) Four main steps in Pauling’s rules guided Monte Carlo search.

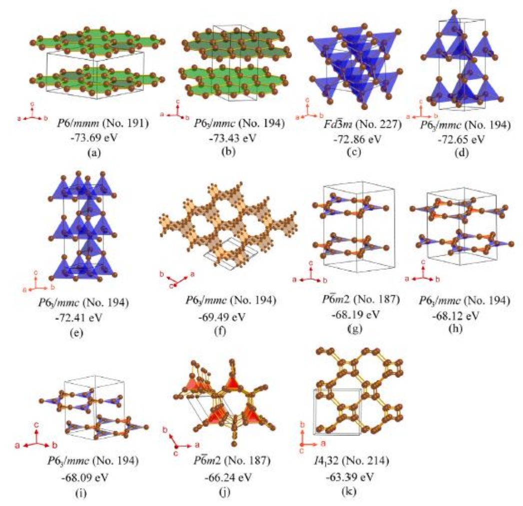

图 3. (a) 具有理想堆积层的石墨层，(b) 石墨层错位堆积，(c) 立方钻石，(d) 4H 钻石，(e) 2H 钻石，(f) H-8 碳，(g–i) 具有不同堆叠的 C_{31} 薄板层，(j) C_{31} 片式聚合物，(k) K_4 水晶。

Fig. 3. (a) Graphite layers with ideal stacking. (b) Graphite layers with displaced stacking. (c) Cubic diamond. (d) 4H diamond. (e) 2H diamond. (f) H-8 Carbon. (g–i) Layers of C_{31} sheets with different stacking. (j) C_{31} sheet polymer. (k) K_4 crystal.

The rapid development of the high-throughput calculations and materials genome approaches in recent years has improved researchers’ ability to design advanced materials. Crystal structure prediction techniques play an important role in high-throughput calculations and materials genome approaches. In this article, a set of easy-operation guidelines for constructing crystal structures is extracted from Pauling’s rules. Based on this set of guidelines, we have designed an algorithm called Pauling’s rules guided Monte Carlo search (PAMCARS), which predict the ground-state and meta-stable inorganic crystal structures of a given composition by combining a classical Monte Carlo search in the configuration space constrained by Pauling’s rules with ab initio structural relaxations. In the actual tests, the crystal structures of carbon allotropes, $CaSO_4$, $Ba_2TiSi_2O_8$ and $BaAlBO_3F_2$ are successfully predicted by this crystal structure prediction algorithm. In addition, a number of unreported high-symmetric metastable crystal structures of carbon, $CaSO_4$ and $Ba_2TiSi_2O_8$ are also predicted. The successful prediction of graphite layers indicates that PAMCARS is able to predict some layered materials assembled by the Van der Waals forces. Two of the predicted low-energy metastable crystal structures of $Ba_2TiSi_2O_8$ may explain the property anomaly of $Ba_2TiSi_2O_8$ around 160 ℃. Pauling's rules guided Monte Carlo search exhibits high efficiency and energy resolution in predicting the ground-state and metastable crystal structures in the tests.

在具备锰离子“自还原”特性的体系中开展研究，发现在四价锰离子还原为二价的过程中，伴随着离子的变价，会形成类似于异价离子取代所产生的缺陷。这些缺陷所形成的陷阱能级会束缚载流子，当材料受到外界机械力刺激的情况下，陷阱能级中的载流子脱陷后经导带与发光中心复合而实现力致发光。系列研究结果表明，材料中的缺陷对发光有重要影响，人们可通过有效的缺陷调控改善材料的发光性质以及制备复合功能发光材料。同时，“自还原”体系的提出也为加快新型力致发光材料的研发指明了有效途径。

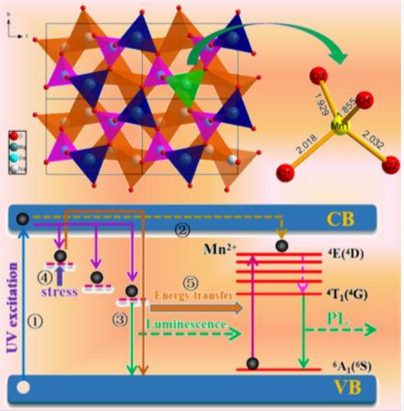

图 4. 新型力致发光材料 $KZn(PO_3)_3:Mn^{2+}$。

Fig. 4 Novel mechanoluminescent material $KZn(PO_3)_3:Mn^{2+}$.

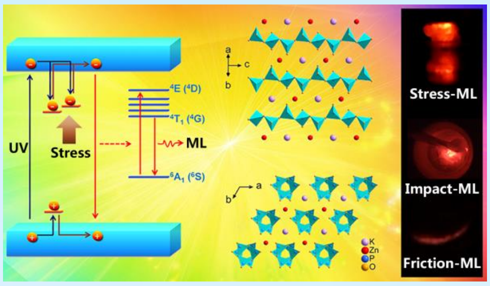

图 5. 新型力致发光材料 $Na_2MgGeO_4:Mn^{2+}$。

Fig. 5 Novel mechanoluminescent material $Na_2MgGeO_4:Mn^{2+}$.

The research is focus on the "self-reduction" system of manganese ions. It is found that during the self-reduction process of Mn^{4+} to Mn^{2+} ions, lattice defects are formed along with the ionic valence change. The defects are similar to those caused by substitution of different valent ions, and form trap levels in the forbidden band which will store some carriers. When the materials are stimulated by external mechanical forces, the carriers will detrap from the trap levels, and recombine with the luminescent center to show the characteristics of mechanoluminescence. A series of research results show the importance of the defects in materials on the optical properties. One can construct multi-functional luminescent materials by effective defect control. Meanwhile, the proposal of the “self-reduction” system also points out an effective way to accelerate the development of novel mechanoluminescent materials.

4D 超快电子显微镜由于超高的时空分辨率被广泛应用于超快结构和载流子动力学测量，但是其光阴极发射的电子存在能量差异，且在自由飞行过程中存在较强空间电荷作用，导致其时间分辨率被限制在几百飞秒量级，远大于材料中电荷运动的时间尺度（数十飞秒）。我们提出了一种基于自由电子和局域光场相互作用的光子诱导近场电子显微镜（PINEM）的“电子选通”方案（two-color photon-pump/PINEM-probe），使用两束不同波长、偏振相互垂直的飞秒激光作为泵浦光（图 6a 所示的 P1 和 P2），其中

飞秒激光脉冲 P1（50 fs）与样品处的电子脉冲同步，产生用于成像和探测的 PINEM 电子，飞秒激光脉冲 P2 则作为泵浦光激发样品的动力学过程，通过调节 P1 与 P2 的时间延迟和利用电子能量过滤系统，实现超高时空分辨的 PINEM 电子成像。当 P1 极化方向与样品边缘平行且与电子脉冲同时到达样品时，将获得最强的电子-光子相互作用和最佳的 PINEM 电子脉冲，其脉冲宽度由 P1 飞秒激光的脉冲宽度决定。而样品的介电函数信息（与样品的电子态直接相关）则通过 P1 产生的近场被直接编码到 PINEM 信号中。因此，可通过探测样品在 P2 飞秒激光泵浦之后（P2 极化方向与样品边界垂直，以排除 P2 产生近场的干扰）PINEM 信号的变化来监测其介电函数随时间的演化，从而获得样品电子态的超快动力学过程。利用该技术，我们在纳米与数十飞秒时空尺度揭示了单根一维 VO_2 纳米线在绝缘体-金属相变过程中电子态的超快演化动力学过程。由于 PINEM 电子的脉冲宽度仅由 P1 飞秒激光脉冲（~50 fs）决定，与原始电子脉冲宽度无关，从而使可使超快电镜的时间分辨率提升了一个数量级，为进一步实现从飞秒与纳米超高时空分辨尺度探测纳米功能材料中的电荷动力学提供了新的思路和方法。

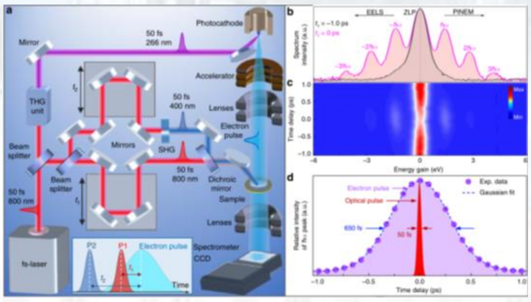

图 6. 双色光子诱导的近场光学超快电子显微镜。

Fig. 6 Two-color photon induced near-field ultrafast electron microscopy.

Due to the ultrahigh spatiotemporal resolution, 4D ultrafast electron microscopy has been widely used in the investigation of ultrafast structural and carrier dynamics of functional materials. However, the energy difference of the electrons emitted by the photocathode and the strong space charge effect during the free flight of the electron pulse result in the limitation of the time resolution to hundreds of femtoseconds (fs), which is much larger than the time scale (tens of fs) of the charge motion in the materials. We proposed a scheme of "electron gate" (two-color by photon-pump/PINEM-the probe, PINEM is an optical field induced electron microscope based on the interaction of the free electron and the local light field), using two perpendicular polarized fs laser pulses with different wavelengths as pump light (P1 and P2 as shown in Fig. 6a), including P1 pulse (50 fs) that is timely synchronized with the electron pulse at the sample to produce PINEM electrons for imaging and detection, and P2 pulse as a pump to tringle the dynamical process in sample. The high space and time resolution of PINEM electronic imaging is realized by adjusting the time delay between P1 and P2 and using the electronic energy filtration system. When the polarization of P1 is parallel to the sample edge and it reaches at the sample timely oveloped with the electron pulse, the strongest electron-photon interaction and the optimal PINEM will be obtained, where the pulse width of the PINEM electrons is determined by the pulse width of P1 laser pulse. The information of dielectric function of the sample (directly related to the electronic state) is directly encoded into the PINEM signal through the near field generated by P1. Therefore, the evolution of the dielectric function over time can be monitored by tracking the changes of the PINEM signal of the sample after the pump of P2 laser pulse (polarization of P2 is perpendicular to the sample edge to exclude the creation of near field), thus obtaining the ultrafast dynamic process of the electronic state of the sample. Using this technique, we reveal the ultrafast evolution dynamics of the electronic state in a single 1D VO_2 nanowire during the insulatpr-metal phase transition at a spatiotemporal scale of nanometer and tens of fs. As the pulse width of the PINEM electrons is only determined by the P1 laser pulse (~50 fs), independent of the original electron pulse width, the time resolution of 4D ultrafast electron microscopy is enhanced by an order of magnitude, which paves a new route for probing carrier dynamics in nanometer functional materials at fs and nanometer ultrahigh spatiotemporal resolution.

将飞秒激光集成于电子显微镜使得可以在超高的时间和空间尺度对物质的结构和形貌动态演化过程进行成像，这也就是 4D 超快电子显微镜技术。激光驱动的光电发射方案是目前实现 4D UEM 的主要方法。然而，实现激光驱动的光电子发射存在几个障碍:飞秒激光器体积庞大且价格昂贵，仪器改装复杂；由于阴极上不可避免的激光指向不稳定，光束波动是一个固有的问题。在这项工作中，我们开发了一种无需飞秒激光的 4D UEM 技术来实现相同的超快成像与探测功能，但不需要复杂的仪器改装。我们通过使用射频（RF）来调制和切断连续电子束获得超短电子脉冲，其重复率从 100 MHz 到 12 GHz 可调，从而开发出了一种新型皮秒电子脉冲发生器。该脉冲电子发生器可以和现有传统电镜进行集成，实现新型的 4D 超快电镜技术。作为首次应用，我们研究了千兆赫电磁波在交错梳状金属天线结构中的传播动力学过程，在纳米空间和皮秒时间尺度下直接观察到了梳状交指线周围电磁场的瞬态振荡过程，发现其局部电磁场具有时间依赖的极化和局部场的振幅增强效应。本研究论证了基于 RF 的无需激光 4D UEM 技术在时空分辨超快动力学可视化研究领域的可行性，特别是在与信息处理技术相关的微电子器件中的超快电动力学研究领域。

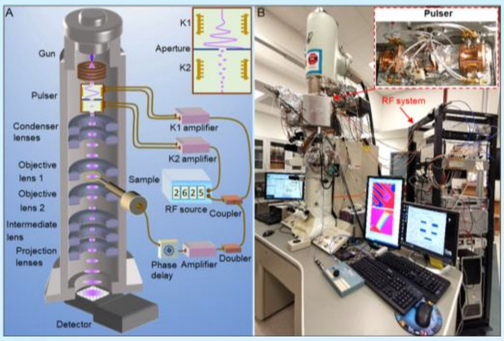

图 7. 基于射频脉冲电子发生器的 4D 超快电子显微镜。

Fig. 7 Laser-free ultrafast electron microscopy based on RF-pulser.

Integrating femtosecond (fs) lasers with electron microscopies has enabled direct imaging of transient structures and morphologies of materials in real time and space, namely, 4D ultrafast electron microscopy (4D UEM). Laser-actuated photoemission scheme is currently the primary method for 4D UEM. However, several barriers exist for achieving laser-actuated photoemission: fs lasers can be bulky and expensive, instrumental modifications are intricate, and beam fluctuation is an intrinsic problem due to the inevitable laser pointing instabilities on the cathode. In this work, we developed a laser-free 4D UEM offering the same capability but without requiring fs lasers and intricate instrumental modifications. We create picosecond electron pulses for probing dynamic events by chopping a continuous beam with a radiofrequency (RF)-driven pulser with the pulse repetition rate tunable from 100 MHz to 12 GHz. As a first application, we studied gigahertz electromagnetic wave propagation dynamics in an interdigitated comb structure. We reveal, on nanometer space and picosecond time scales, the transient oscillating electromagnetic field around the tines of the combs with time-resolved polarization, amplitude, and local field enhancement. This study demonstrates the feasibility of laser-free 4D UEM in real-space visualization of dynamics for many research fields, especially the electrodynamics in devices associated with information processing technology.

稀土离子在氟化物晶体中的溶解度高，发光猝灭浓度低，且氟化物的声子能量低，因此稀土离子掺杂的氟化物材料一直是发光学领域的研究热点，课题组近期在以下两方面取得突破性进展。

Doping concentration of rare earth ions in fluoride crystals is higher and luminescent quenching concentration is lower than others. And phonon energy of fluoride is lower than others. Fluoride doped with rare earth ions has been a focus for science research. We have got advanced in following topic.

(1) 温度诱导的氟化物晶体相转变及相形成机理研究。通过对材料结构、形貌、组分测试和第一性原理计算，研究了温度诱导下的 $KGdF_4$ 的相变机理，认为 $KGdF_4$ 材料的结构是由结构相转变和化学合成两个过程共同决定的。低温时化学合成过程占主导地位，高温时结构相转变过程占主导位置，提出并验证了 $KGdF_4$ 晶体结构相转变过程的物理模型，如图 8 所示。研究结果为可调控特定晶相的材料制备提供了一种新思路，对相似材料的制备有重要参考价值。文章发表于 J Mater Sci: Mater Electron (2020) 31:18096–18104。

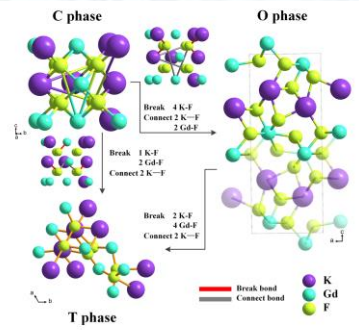

图 8. $KGdF_4$ 在立方相、正交相和三方相之间的结构转换

Fig. 8 The structural phase transition process of $KGdF_4$ between Cubic, Orthogonal and Tripartite phases

Phase transfer and growing mechanism of multi-phase fluoride material induced by temperature. The phase changing mechanism of $KGdF_4$ with temperature is investigated by through measurement on structure, morphology, component and ab initio calculation. The structure of $KGdF_4$ material was decided both by structural phase transition and chemical synthesis. Moreover, chemical synthesis processes dominate at low temperatures and the phase transition processes dominate at high temperatures region. A model of structure phase transition process of the $KGdF_4$ crystal was established reasonably, as shown in Fig. 8. This work provided a new idea for the preparation of $KGdF_4$ material with controlled and specific crystal phases. The results have been published on J Mater Sci: Mater Electron (2020) 31:18096–18104

(2) 稀土离子掺杂氟氧化物玻璃陶瓷中光谱调控和荧光温度传感特性。光谱可调控发光材料是获得白光和三基色发光材料的最佳选择，在 LED 显示和生物荧光探针等领域有重要应用，我们在 $Yb^{3+}/Tm^{3+}/Er^{3+}$ 离子共掺的氟氧化物玻璃陶瓷中，在建立激发态能量传输模型基础上，通过 Er^{3+} 离子浓度的改变成功制备出上转换发光光谱出从蓝紫→冷白→绿→橙红波段的发光材料，研究结果如图 9 所示，首次实现了在同一基质材料中，通过单一元素的浓度改变实现全波段发光。

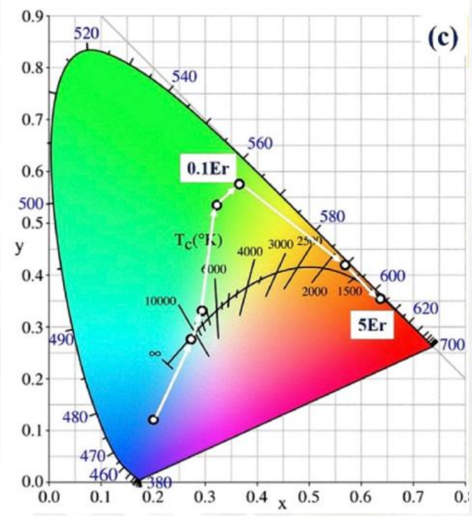

图 9. Er^{3+}/Tm^{3+}/Yb^{3+}共掺的氟氧化物玻璃陶瓷中上转换发光颜色随 Er^{3+}浓度的变化。

Fig. 9 The variation of up conversion luminescent color of the oxyfluoride glass ceramics doped with Er^{3+}/Tm^{3+}/Yb^{3+} as a function of Er_{3+} concentration.

Spectral modulating and fluorescent temperature sensor in oxyfluoride glass ceramics doped with rare earth ions. The luminescent materials of turning spectra are one of best candidates for white and three-based color luminescent materials, which used in LED display of industry and biology probe of medicine. The oxyfluoride glass ceramics doped with Yb^{3+}/Tm^{3+}/Er^{3+} have been fabricated, which have turning up conversion spectra with violet, blue, green and red emission, by modulating Er^{3+} concentration based on the mode of excited state energy transfer. The result is shown as Fig. 9. The novel luminescent material with all visible emission spectra in single host with changing single element was obtained firstly.

根据该体系激发态能量传递机制，在 Tm^{3+}/Er^{3+}中选择合适热能对能级，研究了 Yb^{3+}/Tm^{3+}/Er^{3+}离子共掺的氟氧化物玻璃陶瓷中上转换发光的非接触式温度传感特性，代表性结果如图 10 所示。荧光温度传感灵敏度与选择的热能对有关，绿绿荧光比和红近红外荧光比的温度传感灵敏度呈线性变化趋势，红绿荧光比的温度传感灵敏度呈先降后升的变化趋势，最大灵敏度 2.70，该热能对来自 $^3F_{2,3}$ (Tm^{3+}) /$^4S_{3/2}$ (Er^{3+})。与表 1 中常见材料体系的荧光温度传感灵敏度相比，该材料明显优于已报导的成果。

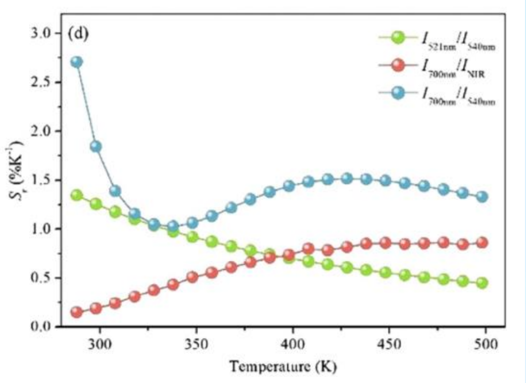

图 10. 976 nm 激光激发下不同耦合对能级的上转换发光温度传感灵敏度随温度的变化趋势。

Fig. 10 The relative sensitivities of the couple energy levels with temperature for up conversion luminescence excited by 976nm.

表 1. 稀土离子掺杂的各类材料中上转换发光的温度传感灵敏度比较，最后一行是本文结果。

Table 1 The relative sensitivities of up conversion luminescent temperature sensing of optical materials doped with rare earth ions. The result of this work is shown in the last line.

Activators	Hosts	Transitions	TR (K)	S_r (%K^{-1})
Er^{3+}	Si glass	$^2H_{11/2}$, $^4S_{3/2}$→$^4I_{15/2}$	303-573	1.11
Er^{3+}	$BaMgF_4$	$^2H_{11/2}$, $^4S_{3/2}$→$^4I_{15/2}$	323-593	0.83
Er^{3+}	YF_3 GC	$^2H_{11/2}$, $^4S_{3/2}$→$^4I_{15/2}$	293-563	1.01
Tm^{3+}	YF_3	$^3F_{2,3}$, $^3H_4$→$^3H_6$	300-750	0.10
Tm^{3+}	PbF_2 GCs	$^3F_{2,3}$, $^3H_4$→$^3H_6$	300-700	0.03
Er^{3+}/Tm^{3+}	β-PbF_2 GC	$^3F_{2,3}$→$^3H_6$ /$^4S_{3/2}$→$^4I_{15/2}$	288-498	2.70

Noncontact up-conversion luminescent temperature sensing properties of oxyfluoride glass ceramics doped with Yb^{3+}/Tm^{3+}/Er^{3+} were studied systematically using novel coupled energy levels of Tm^{3+} / Er^{3+} according to the mechanism of excited state energy transfer, which is shown as Fig. 10. The relative sensitivities of luminescent temperature sensing are decided by the coupled energy levels. The sensitivities of temperature sensing of I_{521}/I_{546} decreases linearly and the sensitivities of I_{700}/I_{NIR} increases linearly with temperature. However, the sensitivity of I_{700}/I_{546} decrease dramatically and then increase smoothly. And the maximum is 2.70, which is from the energy levels of $^3F_{2,3}$ (Tm^{3+}) /$^4S_{3/2}$ (Er^{3+}). It is much higher than others in Table 1.

YAG:Yb 晶体作为一种具有纳秒级衰减时间的快闪烁晶体，被用于高重频辐射探测领域。但该晶体在使用中存在闪烁发光强度低和晶体抗辐照硬度差的问题。通过深入研究该晶体的闪烁发光机制和辐照损伤形成机制，从而为解决上述问题提出相应的方案。图 11 表明，YAG:Yb 晶体在 300-600 nm 以及 900-1100 nm 区间都有明显的 X 射线激发下的发光。但是该晶体的发光存在明显的吸收现象，导致晶体所发的光会很大程度上被自吸收，其中 900-1100 nm 的红外发光自吸收强度要强于 300-600 nm 的发光。从图 12 可观察到 XEL 的强度随着温度升高有着明显的降低，说明晶体的发光存在着较强的温度猝灭效应。图 13 表明晶体在 330 nm 发光的衰减时间较慢，而 500 nm 发光的衰减时间较快。从根据第一性原理计算获得的 YAG:Yb 晶体的能级图（图 14）可看出，晶体在 400-600 nm 之间的发光都可归因于氧空位的发光。从 YAG:Yb 晶体的 EDS 结果（图 15）可看出，晶体中不同部位的氧含量非常不均匀，这一结果验证了晶体中存在大量氧空位这一假设。我们的研究揭示了 YAG:Yb 在 300-600 nm 的发光存在两种机制。其中 400-600 nm 的宽带发光是由氧空位引起的发光，其衰减时间较快。透射电镜实验结果进一步证明了这一结论。

YAG:Yb crystal is applied in the high-repetition imaging because of its nanosecond decay time. However, the YAG:Yb crystal shows low scintillation light output and poor radiation hardness. Our investigation on the scintillation mechanism and radiation induced damage mechanism is going to propose an approach to address these issues. Fig. 11 shows the transmittance spectra and X-ray excited luminescence (XEL) of YAG:Yb with various Yb content. There are two broad band emission ranging from 300-600 nm and 900-1100 nm. The significant self-absorption effect is observed in the crystal, which will induce strong self-absorption of scintillation light. And the self-absorption effect of 900-1100 nm light is stronger. Figure 12 shows XEL of YAG:Yb crystal measured at various temperature. The intensity of XEL depends on the temperature, indicating the significant temperature quenching effect of the scintillation light. Fig. 13 shows decay curve of YAG:Yb excited by X-rays. It demonstrates the decay time of 330 nm scintillation light is longer, while that of 5000 nm scintillation light is shorter. Fig. 14 shows the energy levels of oxygen vacancies in YAG:Yb crystal. It illustrates the scintillation light between 400-600 nm of YAG:Yb crystal can be attributed to the luminescence of oxygen vacancies. Fig. 15 shows EDS result of YAG:Yb crystal measured by TEM. It shows the distribution of oxygen in the crystal is not homogeneous, which demonstrates the model that there are many oxygen vacancies in the crystal. Our investigation illustrates there are two kinds of luminescence mechanism for 300-600 nm scintillation light. The broad emission band between 400-600 nm is attributed to the emission of oxygen vacancies. And its decay time is very short. The TEM result demonstrates the conclusion.

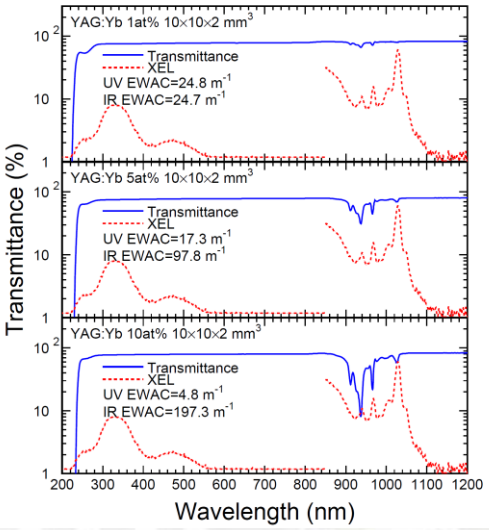

图 11. 不同 Yb 掺杂浓度 YAG 晶体的透过光谱和 X 射线激发发射光谱。

Fig. 11 Transmittance spectra and XEL of YAG:Yb with various Yb content.

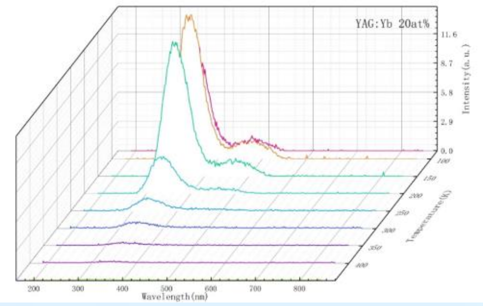

图 12. YAG:Yb 晶体的变温 XEL。

Fig. 12 XEL of YAG:Yb measured at various temperature.

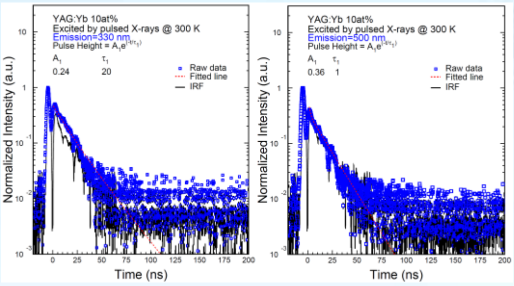

图 13. YAG:Yb 晶体在 X 射线激发下的衰减时间。(左) 330 nm 发光；(右) 500 nm 发光。

Fig. 13 The decay curve of YAG:Yb excited by X-rays. (left) 330 nm light; (right) 500 nm light.

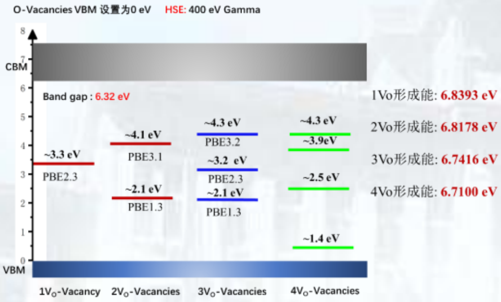

图 14. YAG:Yb 晶体内的氧空位能级。

Fig. 14. The energy levels of oxygen vacancies in YAG:Yb crystal.

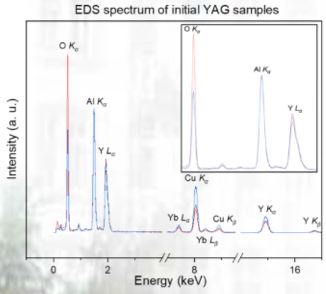

图 15. YAG:Yb 晶体在透射电镜里面测试到的微区能谱。

Fig. 15 The EDS result of YAG:Yb crystal measured by TEM.

肿瘤治疗是临床医学面临的重要挑战之一。到目前为止，不同的癌症治疗方法已经取得了较大的发展，如放射治疗，手术，化疗和光动力治疗。在此，我们提出了一种新的癌症治疗方法，即在 37℃体温利用 TiO_2-Pd/石墨烯复合材料产生活性氧(ROS)杀死癌细胞。研究结果表明，BALB/c 小鼠的肿瘤在 37℃体温条件下成功消退，没有任何外部条件，如辐射、紫外线、可见光和红外照射。该方法对于癌症治疗的实际应用是一个可行的方法。

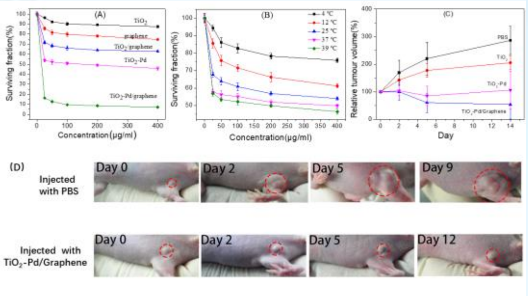

图 16. (A) 在 37℃和 16 小时条件下，A549 细胞存活率与 TiO_2, 石墨烯,TiO_2/石墨烯,TiO_2-Pd 和 TiO_2-Pd /石墨烯的浓度的关系；(B)在不同的温度下 4 小时，A549 细胞存活率与 TiO_2-Pd /石墨烯浓度的关系；(C)不同样品治疗后小鼠肿瘤体积生长曲线；(D) 治疗前后小鼠肿瘤的变化照片。

Fig. 16 (A) Variation in surviving fraction of A549 cells with the concentration of TiO_2, graphene, TiO_2/graphene, TiO_2-Pd and TiO_2-Pd/graphene at 37 oC for 16 h. (B) Variation in surviving fraction of A549 cells with the concentration of TiO_2-Pd/graphene at different temperatures for 4 h. (C) Tumor volume growth curves on mice after treatment with different samples. Error bars were based on s.d. of 3 mice per group. (D) Representative photos of tumors on mice after various treatments indicated.

Cancer therapy is one of the most important challenges in clinical medicine. So far diferent methods have been developed for cancer therapy, such as radiation therapy, surgery, chemotherapy and photodynamic therapy. Here we propose a new concept for cancer therapy, i.e., killing the cancer cells simply via reactive oxygen species (ROS) generated by TiO_2-Pd/graphene composites. Activated by animal heat of 37 ℃, the electrons in the valence band can be excited to the conduction band of TiO_2 via the energy levels of Pd species and graphene, generating ROS without light irradiation or electric excitation. The tumors in BALB/c mice are successfully regressed at animal heat without any other external conditions, such as radiation, UV, visible and IR irradiation. Our results suggest that the design of animal heat activated cancer therapy is a feasible concept for practical applications of cancer treatments.

采用水热法合成了 α-MnS 和 γ-MnS 光催化剂，利用光沉积法制备了 Pd 修饰的 γ-MnS 光催化剂。通过 XRD、SEM 和 TEM 对其尺寸、结构和形貌进行了表征。α-MnS 为{200}面暴露双棱锥结构，而 γ-MnS 为{100}、{110}和{102}面暴露的六棱锥结构。通过理论计算研究了催化剂的态密度和能带结构。结果表明，Pd 作为活性物种存在于催化剂表面,扩展了可见光的吸收,促进了电子和空穴的分离,并提高了光还原 CO_2 合成 CH_4 的光催化活性，从而证明了表面改性对于发展与高活性的催化剂是一种有效的方法。本研究为设计和合成具有高性能和应用潜力的新型可见光催化剂奠定基础。

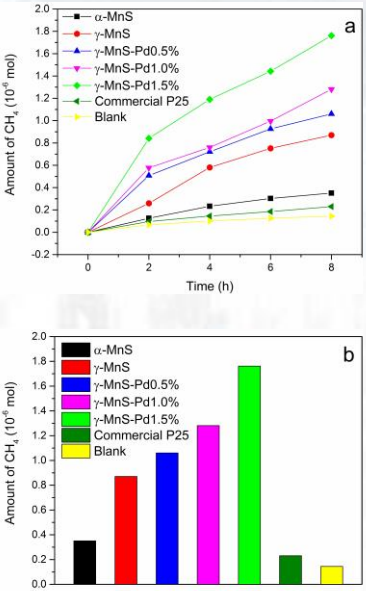

图 17. (a) P25，α-MnS，γ-MnS 和 γ-MnS－PdX%的光催化活性；(b) P25、α-MnS、γ-MnS 和 γ-MnS－PdX%在第 8 小时的光催化活性。

Fig. 17 (a) Photocatalytic activities of commercial P25, α-MnS, γ-MnS, and γ-MnS–PdX%. (b) Photocatalytic activities of commercial P25, α-MnS, γ-MnS, and γ-MnS–PdX% at the eighth hour.

α-MnS and γ-MnS photocatalysts were synthesized by the hydrothermal method and their size, structure, and appearance were determined by X-ray diffraction (XRD) patterns and scanning (SEM) and transition (TEM) electron microscopy images. α-MnS behaved as a bipyramid exposed with {200} facet, while γ-MnS behaved as a hexagonal prism exposed with {100}, {110}, and {102} facets. In addition, palladium (Pd)-modified γ-MnS photocatalysts were prepared via a photodeposition method, and their density of states and energy band structure were studied by theoretical calculations. The introduced Pd ions, which existed on the photocatalysts surface as –S–Pd–S– active species, expanded the visible light absorption, promoted the separation of electrons and holes, and improved the photocatalytic activity for the photoreduction of CO_2 to CH_4, indicating surface modification as an effective method for the development of MnS-based materials with high CO_2 photoreduction activity. Therefore, this study could set the basis for the design and synthesis of novel visible light photocatalysts with active surface and high application potential in diverse fields.

采用水热法合成了一系列用于 CO_2 光还原的 Pd 修饰硫化物催化剂(ZnS-PdX%、In_2S_3-PdX%和 CuS-PdX%)。–S–Pd–S–表面物种的引入增加了硫化物催化剂的可见光吸收，延长了光生电子的寿命，抑制了光载流子的复合。此外，催化剂的带结构与 CO_2 氧化还原电位的匹配得到改善。与 ZnS、In_2S_3 和 CuS 的相比，ZnS- Pd1.5%、In_2S_3-Pd1.5%和 CuS- Pd1.5%催化剂的光催化活性有效提高。

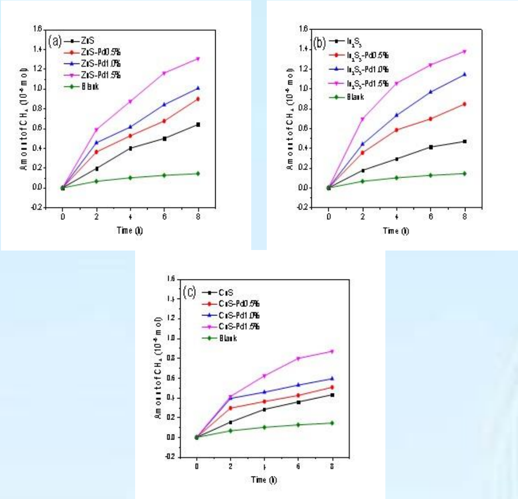

图 18. (a) ZnS 和 ZnS－PdX%，(b) In_2S_3 和 In_2S_3－PdX%，(c) CuS 和 CuS－PdX%在紫外光照射下 8 小时光还原 CO_2 合成 CH_4 的光催化活性。

Fig. 18 Photocatalytic activity of (a) ZnS and ZnS–PdX%, (b) In_2S_3 and In_2S_3–PdX% and (c) CuS and CuS–PdX% for the photoreduction of CO_2 to CH_4 under UV light for 8 h.

A series of Pd-modified sulphide photocatalysts (ZnS–PdX%, In_2S_3–PdX% and CuS–PdX%) for the photoreduction of CO_2 were synthesised via a simple hydrothermal method. Here, the introduction of the –S–Pd–S– surface species onto the surface of the sulphides extended the visible light absorption, prolonged the lifetime of photogenerated electrons and suppressed the recombination of the photocarriers. Additionally, the match between the band structure and the redox potential for the photoreduction of CO_2 was improved. As a result, the photocatalytic activity of ZnS–Pd1.5%, In_2S_3–Pd1.5% and CuS–Pd1.5% was enhanced when compared with the results from ZnS, In_2S_3 and CuS photocatalysts.

该研究制备了四种金属离子(M: Pt、Pd、Cu 和 In)修饰的 TiO_2 (TiO_2-M)热催化剂，而且 TiO_2- Pd 和 TiO_2 -Pt 的热催化活性明显高于 TiO_2、TiO_2- Cu 和 TiO_2 -In 催化剂。研究表明，金属离子(M: Pt、Pd、Cu 和 In)以 O-M-O 和/或 O-M-Cl 的形式存在于 TiO_2 表面；通过 Pd 或 Pt 物种的准连续能级，TiO_2-Pd 和 TiO_2- Pt 催化剂能有效地将热激发电子从价带转移到导带，从而对于降解 HCHO 表现出的显著热催化活性。此外，系统研究了热催化体系中 TiO_2-M 的能带结构与热载流子氧化还原以及和活性氧物种(如 O_2^-、·OH)的生成关系。结果表明，半导体带隙中的准连续能级是实现热功能材料高效热催化性能的关键因素之一。

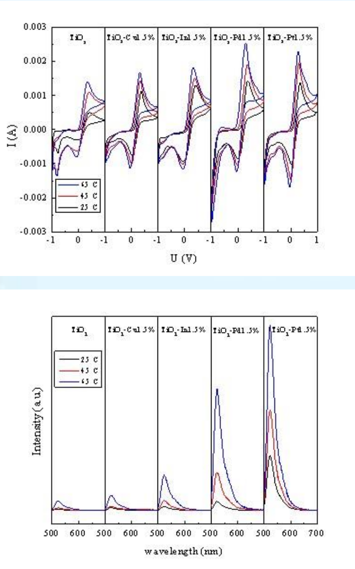

图 19. TiO_2 和 TiO_2- M1.5% (M: Cu, In, Pd 和 Pt)在不同温度下的 DCF 循环伏安曲线和荧光光谱。

Fig. 19 Cyclic Voltammetry curve and fluorescence spectra of the DCF of pure TiO_2 and TiO_2-M1.5% (M: Cu, In, Pd and Pt) at difference temperature.

Four metal ions (M: Pt, Pd, Cu and In) modified TiO_2 (TiO_2-M) thermal catalysts were prepared. The metal ions exist on the surface of TiO_2 as *O-M*-O and/or *O-M*-Cl species. TiO_2–Pd and TiO_2–Pt samples exhibit much better thermal catalytic activity than TiO_2, TiO_2–Cu and TiO_2–In. Due to the efficient thermal excited electrons transfer from the valence band to the conduction band through quasi-continuous energy levels of Pd or Pt species, the TiO_2–Pd and TiO_2–Pt catalysts exhibited significant thermal catalytic activity for degradation of HCHO. Furthermore, the relationship between band structure and redox ability of thermal charge carriers for TiO_2-M, as well as the generation ability of ROS (reactive oxygen species, for instance, O_2^- and OH) in thermal catalysis system are investigated systematically. This work revealed that the quasi-continuous energy level in the band gap of semiconductors is one of the key factors to achieve efficient thermal catalytic performance over thermal-functional materials.

我们采用格子自洽场理论研究了受限于两平行板间的不同链结构的对称 AB-型嵌段共聚物(线形 AB、星形 A_2B_2、环形 AB)熔体形成的层状结构。我们令不同链结构体系的板间距 D 满足 $D/R_g \approx 5$(R_g 为理想格子链的回旋半径)，而且 D 的值与体相周期 L_0 相等。计算结果表明，当不同链结构体系的链长 N 相同时，环形和星形链体系形成的层状结构周期 L 比线形链体系形成的小；星形链体系在组分间排斥作用参数 χN_{AB}(χ 为 Flory-Huggins 相互作用参数，N_{AB} 为单个共聚物分子中一对 A 和 B 嵌段的总链节数目)比环形和线形链体系都小的情况下，其归一化界面宽度介于环形和线形链体系之间。我们还发现，当两板为中性时，垂直层结构的单链自由能比平行层结构的低。随着板对共聚物中一种嵌段的选择作用 Λ 的增大，体系发生垂直层到平行层的一阶相变。当不同链结构体系的分离强度相同时，星形链(由于链端点多)体系一阶相变对应的 Λ 值最大，即体系最容易保持垂直层结构。这些发现证明星形嵌段共聚物比线形和环形嵌段共聚物更适合应用于共聚物纳米刻蚀。

We compare the lamellae formed by symmetric linear AB diblock, symmetric ring AB diblock, and symmetric star A_2B_2 copolymer melts confined between two parallel and identical surfaces using LSCF. All the systems have comparable $D/R_g \approx 5.0$, where D is the distance between the two surfaces and R_g denotes the root-mean-square radius of gyration of an ideal chain, and D equal to the bulk lamellar period L_0. We find that the domain sizes of ring and star copolymers are smaller than that of the linear AB counterparts with the same chain length N. The normalized A-B interfacial width of perpendicular lamellae for star copolymers have a modest value, although its χN_{AB} is smaller than linear and ring copolymers with χ being the Flory-Huggins parameter and N_{AB} being the number of segments on one pair of A- and B-blocks. Furthermore, the calculated Helmholtz free energy per chain shows that perpendicular lamellae are stable over parallel lamellae when the two confining surfaces are neutral. As the surface preference Λ (e.g., for B-segments) increases, all systems exhibit a first-order phase transition from perpendicular to parallel lamellae. At the same degree of segregation, the star copolymers have larger Λ range to form perpendicular lamellae than linear and ring copolymers. These findings prove that star block copolymers are more suitable for lithographic applications of copolymers.

我们采用格子自洽场理论研究了受限于两平行板间的对称星形共聚物 A_mB_m (m=1, 2, 3, 4, 5)熔体形成的层状相结构。在给定的相互作用下 χN_{AB} 不变，$N_{AB}=(N-1)/m$，针对 $D=L_0$ 的情况，系统考察了 N 和单个共聚物分子中 A(或 B)臂数目 m 对受限层结构细节及层取向的影响。计算结果表明，当 N 或 N_{AB} 不变时，受限层的归一化界面宽度随 m 的增大而减小。受限板为中性时，垂直层结构的单链自由能比平行层结构的低。当 m 不变时，N 越小的体系发生垂直层到平行层的一阶相变对应的 Λ 值越大，体系越容易保持垂直层结构。并且 N 越小，层状结构周期越小。当 N 或 N_{AB} 不变时，m 越大体系越容易保持垂直层结构。总之，星形共聚物的链长越短、臂数越多时，垂直层稳定的 Λ 区间越大、层状结构的界面宽度越小。这些结论可以指导刻蚀应用中对体系参数的选择。

We study the lamellar structures formed by incompressible melts of symmetric star block copolymer (BCP) A_mB_m confined between two identical, homogeneous and parallel surfaces with $D = L_0$, using LSCF calculations on a simple cubic lattice. All the star BCPs have the same χN_{AB} value. The effects of N and the number of A or B arms m in each A_mB_m chain on the lamellar structures and the orientation were investigated in details. We found that the normalized A-B interfacial widths of the confined lamellae increase with decreasing m at fixed N or $N_{AB} = (N-1)/m$. The calculated Helmholtz free energy per chain shows that perpendicular lamellae are stable over parallel lamellae when the two confining surfaces are neutral. At a fixed m value, the star BCPs with smaller N have larger Λ range to form perpendicular lamellae. At a fixed N (or N_{AB}), the star BCPs with larger m have larger Λ range to form perpendicular lamellae. These findings may provide useful information for the lithographic applications of BCPs.

光场调控及其应用/Manipulation of Optical Fields and Its Application

负责人：王慧田

本方向主要开展新型矢量光场的调控生成及应用、非线性光学效应、量子光学及新材料的理论预测等方向的研究。本年度发表论文 6 篇；申请或授权专利 3 项。董校获“天津市创新人才推进计划青年科技优秀人才”。在研课题经费 427 万元。取得的代表性成果如下：

In our direction, we mainly focused on the generation of the new kind of vector optical fields and their applications, the nonlinear effect, quantum optics and Material Calculation and Prediction. This year, we have 6 published papers and 3 authorized patents this year. The research project was funded with 4.27 million RMB. Xiao Dong received “Tianjin Innovative Talent Promotion Plan”. We obtained some respective results as follows.

（1）涡旋光子的双缝干涉/ Double-slit interference of vortex photons

光子轨道角动量(OAM)是螺旋波前为 $\exp(il\phi)$ 的涡旋光束所具有的特征，并且该光束中的每个光子将携带量子化的 $l\hbar$ 的轨道角动量，其中 l 为拓扑荷，原则上可以取 $-\infty$到$+\infty$的任意整数，从而可以提供无限维 Hilbert 空间。OAM 作为一种新的自由度和独立的物理维度可以用来承载独立的信息通道，为光学和量子超高容量信息处理打开了大门。

光子作为一个基本粒子具有波粒二象性。但是，携带轨道角动量的涡旋光子在双缝干涉中的量子特性尚不清楚。我们基于平均光子轨迹(APTs)，从理论上描述了携带 OAM 的单光子在双缝干涉中的干涉行为。模拟结果表明，平均光子轨迹具有明显的螺旋结构，这意味着涡旋光子的传播速度低于既定的光速。平均光子轨迹的端点概率变为周期性弯曲条纹，反映了涡旋光子的波动特性。实验上利用单光子符合成像装置观测了单光子轨道角动量的双缝干涉，实验结果展现了涡旋光子的波粒二象性，如图 1 所示。该工作为理解微观量子行为提供了一种直观方法，并且所提出的方法也可用于探索其它量子粒子的微观行为，若借助更先进、更灵敏的量子检测技术，螺旋粒子的类螺旋性质可应用于量子精密测量。该研究工作发表在[Chinese Optics Letters 18, 10 (2020)]，并被选为 Editor’s Pick。

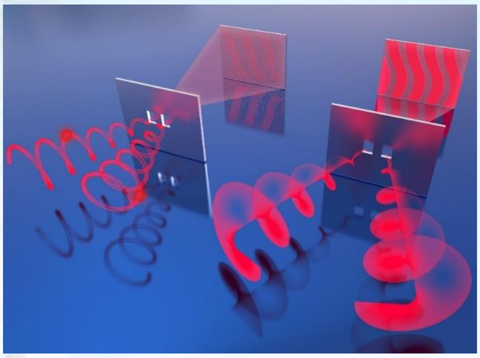

图 1. 光子平均轨迹描述了双缝干涉中涡旋光子的粒子行为和波动特性。

Fig. 1 The average photon trajectories describe the particle behavior and wave characteristics of vortex photons in double-slit interference.

As a basic particle, photon has wave particle duality. However, the quantum properties of vortex photons with orbital angular momentum in double slit interference are still unclear. Based on average photon trajectories (APTs), we theoretically describe the interference behavior of single photons carrying OAM in double-slit interference. The simulation results show that the APT has an obvious helical structure, which means that the propagation speed of vortex photons is lower than the established speed of light. The probability of the end points of APTs becomes a periodic curved stripe, which reflects the wave characteristics of vortex photons. In the experiment, the single-photon coincidence imaging device was used to observe the double-slit interference of single-photon orbital angular momentum, and the experimental results showed the wave-particle duality of vortex photons, as shown in fig.1. This work provides an intuitive method for understanding microscopic quantum behavior, and the proposed method can also be used to explore the microscopic behavior of other quantum particles. With the help of more advanced and sensitive quantum detection technology, the helical-like nature of helical particles can be applied to quantum precise measurement. This research was published in [Chinese Optics Letters 18,10 (2020)] and was selected as editor's pick.

（2）高维纠缠的渐近锁定层析/Asymptotical Locking Tomography of High-Dimensional Entanglement

量子纠缠是量子信息处理中至关重要的一种资源，一直以来都是国际学术界研究的焦点。光子的偏振纠缠调控手段已相对成熟并应用于量子密集编码、量子密钥分发、量子隐形传态和纠缠交换等多种量子协议中。但是，由于维度的限制，基于偏振自由度的量子协议的信道容量不能大于 2 比特。高维纠缠是打破这一限制的重要途径，且相对于二维纠缠具有更强的鲁棒性。然而，若要利用高维纠缠态，先决条件之一就是能对其进行定量标定，可通过量子态层析实现。虽然目前已报道了几种量子态层析方法，诸如传统的量子态层析、无偏量子态层析和对称信息量子态层析等，但是这些方法随着纠缠维度的提高，所需的测量急剧增加（$\sim d^4$），实用性大大降低，极大地妨碍了高维纠缠优势的发挥，限制了更广泛和深入的应用。因此，找到一种高效且实用的量子态层析方法是亟需解决的关键问题。

我们提出了一种非常实用的高效量子态层析方法—渐近锁定层析(ALT)。该方法只需$<2d^2$的测量，即可获得双光子 d 维纠缠态的密度矩阵。基于实验上制备的双光子自旋-轨道角动量 4 维超纠缠态，文章验证了该方法的可行性（图 2），为高维量子态层析提供了一种全新的高效手段，有望成为高维量子态表征的标准方法之一。此方法不仅适用于双粒子高维纯态，还可用于多粒子高维纯态以及一些特殊的混合态，有望推动高维量子纠缠更加深入和广泛的应用。研究工作以 Express Letters 形式发表在 [Chinese Physics Letters 37, 034204 (2020)]。

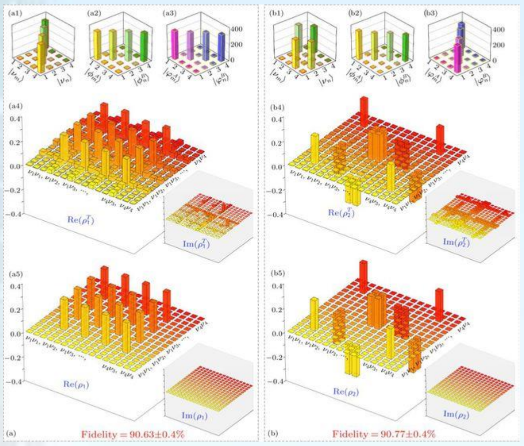

图2 实验制备的两个4维自旋-轨道角动量超纠缠态的重构密度矩阵。

Fig. 2 Experimental data and reconstructed density matrices for the spin-OAM hyperentangled states.

Quantum entanglement is a vital resource in quantum information processing, and it has always been the focus of international academic research. Polarization entanglement manipulation of photons has been relatively mature and applied into many quantum protocols, such as quantum dense coding, quantum key distribution, quantum teleportation and entanglement swapping. Due to the limitation of dimension, the quantum protocols based on the polarization-entangled Bell states is limited to 2 bits for a single qubit. High-dimensional (HD) entanglement is the most promising way of transcending the limitation, and it offers improved robustness with respect to the two-dimensional one. To capitalize on the HD entangled states, the prerequisite is to quantify them explicitly which can be realized by quantum state tomography. Hence, several quantum state tomography methods have been presented, such as full quantum state tomography mutually unbiased bases quantum state tomography, and symmetric informationally complete positive operator-valued quantum state tomography. For bipartite entangled state with each particle having d-dimension, the measurements required in the above methods dramatically increase in d^4, making them impractical and without advantage for the HD entanglement. This will strongly mitigate possible advantages and practical applications of HD entanglement. Therefore, finding an efficient and practical strategy is the key problem to be solved.

Here we present a very efficient and practical method—asymptotical locking tomography (ALT), which can acquire the density matrix of bipartite entangled state with each particle having d-dimension by measurements less than $2d^2$. In the experiment, we use a four-dimensional (4D) spin-OAM hyperentangled state to verify the strategy (see fig. 2). This provides a new and efficient method for high-dimensional quantum state tomography, and is expected to become one of the standard methods for the characterization of high-dimensional quantum states. It is valid for not only the two-particle pure HD entangled state but also the special mixed state and multipartite HD entangled state. Our ALT method should be a great advance to promote the practical applications of HD entangled states. The research was published in [Chinese Physics Letters 37, 034204 (2020)] in the form of Express Letters.

（3）氦是元素周期表中最惰性的元素之一，极难形成化合物。许多科学家试图寻找稳定的氦元素化合物，并且做出了许多积极的探索，其中最成功的例子是 HHe$^+$，它是氦化合物的最具代表性的自由基，是已知最强的酸。HHeF 被认为是最可能含有 HHe$^+$ 的化合物，但在实验上几乎不可能观察到。对 HHe$^+$ 的探索不仅在化学上非常重要，而且在地球科学和行星科学中也有着重要意义。但是，对于 HHe$^+$，人们仍不知道它是否可以存在于这种压力极高的巨型地幔的环境中以及对行星内部物理的化学行为有什么样的作用。已经有研究证明，高压下可以形成氦的稳定化合物，由此我们猜测在高压下是否也可以形成稳定的 HF-He 化合物，是否会存在 HHe$^+$。我们采用基于进化算法的结构预测软件 USPEX 在高压下对 HF-He 体系进行了变组分结构搜索。通过系统的搜索，我们证明了在 1000GPa 以下的压力环境下 HHe$^+$ 是不能形成的。我们还发现了两个新型的化合物，即 He$_2$ (HF)$_4$ 和 He(HF)，其中 He$_2$ (HF)$_4$ 具有方形的 HF 环状结构，He(HF)具有手性链的 HF 结构。He$_2$ (HF)$_4$ 还具有类芳香性的电子行为(图 3)。以上结果拓展了我们对惰性气体的认识，也使我们对巨行星内部化学键和化学压力的形成有了新的认识和理解。

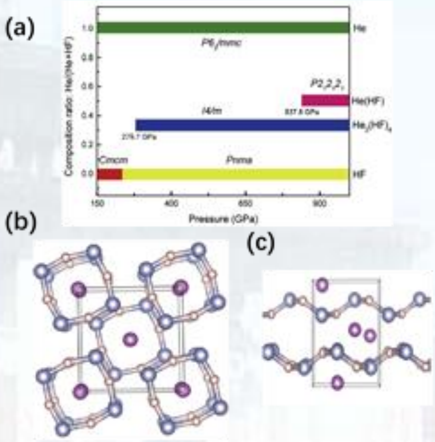

图 3. (a) HF-He 体系压力-组分相图；(b) He$_2$ (HF)$_4$ 在[001]方向上的结构图；(c) He(HF)在[100]方向上的结构图。

Fig. 3 (a)The phase diagram of HF–He system; (b) The conventional cell of He$_2$(HF)$_4$ in [001] orientation; (c)The conventional cell of He(HF) in [100] orientation.

Helium is one of the most inert elements in the periodic table, which is extremely difficult to form compounds. Many scientists have tried to find stable helium compounds and made many active explorations. The most successful example is HHe$^+$, which is the most representative free radical of helium compounds and the strongest acid ever known. HHeF is considered to be the compound most likely to contain HHe^+, but it is almost impossible to observe experimentally. The exploration of HHe^+ is not only very important in chemistry, but also in earth science and planetary science. However, for HHe^+, people still do not know whether it can exist in the giant mantle environment which has extremely high pressure and what effect it has on the physical and chemical behavior of the planet's interior. Studies have shown that stable compounds of helium can be formed under high pressure, so we suspected whether stable HF-He compounds can also be formed under high pressure and whether HHe^+ will exist. We used the structure prediction software USPEX based on evolutionary algorithm to search the structure of HF-He system under high pressure. Through systematic search, we proved that HHe^+ cannot be formed in a pressure environment below 1000 GPa. We also discovered two new compounds, namely $He_2(HF)_4$ and He(HF), where $He_2(HF)_4$ has a square HF ring structure, and He(HF) has a chiral chain HF structure. $He_2(HF)_4$ also has aromatic-like electronic behavior (see fig. 3). The above results expand our understanding of noble gases and also have impact on our understanding of the formation of chemical bonds and chemical pressures inside giant planets.

光谱表征及传感技术/Spectral Charaterization and Sensing Techniques

负责人：宋峰

本方向涉及稀土发光材料制备、稀土材料发光光谱、温度传感、二维材料光电性质研究、成像光谱研究、超分辨成像研究、近红外光谱算法研究、气体与水的光学监测等方面的研究。本年度发表论文 6 篇，申请专利 1 项，授权专利 7 项。本年度获得天津市科学技术进步奖一等奖 1 项。2020 年度“光谱表征及传感技术”方向主要在以下方面取得了进展：

Our groups mainly focused on the preparation of rare-earth luminescent materials and the study of luminescent spectra and temperature sensing properties of rare-earth materials, optical properties and electrical properties of two-dimensional materials, imaging spectroscopy, super resolution imaging, near-infrared spectroscopy algorithm, optical monitoring of gas and water, etc. Six papers have been published in international academic journals, 1 patent were applied for, and 7 patents were authorized. A First-Class Prize of Tianjin Science and Technology Progress Award was awarded. In 2020, “spectral characterization and sensing techniques” has made progress in the following aspects:

（1）采用化学沉淀法在室温下合成了一系列橙红色发光 $K_{0.3}Bi_{0.7}F_{2.4}:Eu^{3+}$荧光粉，具有快速、经济、省时的制备特点。XRD 和 Rietveld 精修结果证实了所制备的材料为纯相。确定了 Eu^{3+}最佳掺杂浓度为 40% mmol，并验证了相应的浓度猝灭机制为偶极-偶极相互作用。此外,利用 Judd-Ofelt 理论研究了 Eu^{3+}在 $K_{0.3}Bi_{0.7}F_{2.4}$ 中所处的局部结构环境和 J-O 参数的趋势($\Omega_2>\Omega_4$)。$K_{0.3}Bi_{0.7}F_{2.4}:Eu^{3+}$的热重分析和活化能结果表明，所制备的材料具有高热稳定性，在温度传感器应用中表现出良好的性能。此外，研究了样品在 303-573 K 的温度依赖性，以探讨热猝灭性能。通过特殊的热猝灭性能实现了发光温度传感，并获得了 1.54×10^4 K^{-1}左右的高温灵敏度，这表明 $K_{0.3}Bi_{0.7}F_{2.4}:Eu^{3+}$是一种很有前景的光学温度计。另一个重要的结果是，$K_{0.3}Bi_{0.7}F_{2.4}:Eu^{3+}$呈现出的 CIE 坐标(0.6226,0.3747)为橙红色发射，在 UV 灯(365 nm)照射下的发光也显示出明显的橙红色，且色纯度约为 98.4%，表明制备的 $K_{0.3}Bi_{0.7}F_{2.4}:Eu^{3+}$ 可潜在地应用在 UV w-LEDs。

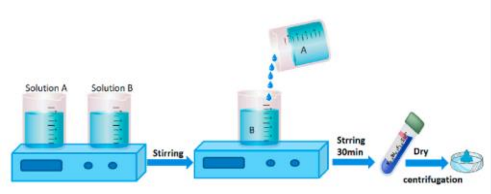

图 1. $K_{0.3}Bi_{0.7}F_{2.4}:x\%Eu^{3+}$ 纳米颗粒制备流程图。

Fig. 1 Schematic diagram of preparation process for $K_{0.3}Bi_{0.7}F_{2.4}:x\%Eu^{3+}$ nanoparticles.

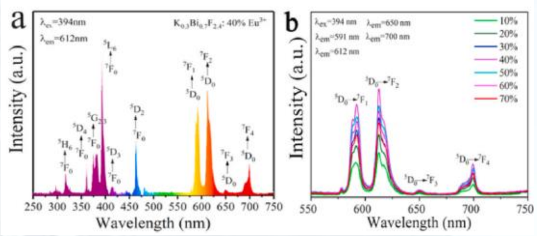

图 2. (a) $K_{0.3}Bi_{0.7}F_{2.4}:40\%Eu^{3+}$的激发和发射谱图，(b) 杂不同浓度 Eu^{3+}的 $K_{0.3}Bi_{0.7}F_{2.4}:40\%Eu^{3+}$发射谱图。

Fig. 2 (a) Excitation and emission spectra of the $K_{0.3}Bi_{0.7}F_{2.4}:40\%Eu^{3+}$ products, (b) Emission spectra of the $K_{0.3}Bi_{0.7}F_{2.4}:x\%Eu^{3+}$ products under various Eu^{3+}.

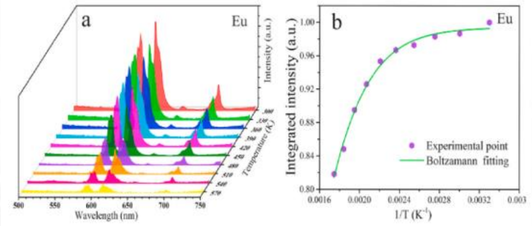

图 3. (a) 不同温度下 $K_{0.3}Bi_{0.7}F_{2.4}:Eu^{3+}$样品的荧光发射谱图，(b) $K_{0.3}Bi_{0.7}F_{2.4}$ 中 Eu^{3+}离子中电子 $^5D_0$-$^7F_2$ 跃迁的相对强度的温度依赖性。

Fig. 3 (a) Emission spectra of $K_{0.3}Bi_{0.7}F_{2.4}:Eu^{3+}$ samples at different temperature, (b) Temperature dependence of relative intensity of Eu3+ ions ${}^5D_0$-${}^7F_2$ transition in the $K_{0.3}Bi_{0.7}F_{2.4}$: Eu^{3+}.

A series of orange red emitting $K_{0.3}Bi_{0.7}F_{2.4}:Eu^{3+}$ phosphors were synthesized via a chemical precipitation reaction method at room temperature, which is convenient, economical and less time consuming. XRD and Rietveld refinement results confirm the pure phase of as-prepared materials. The optimal doping concentrations are determined to be 40%mmol, and both of the corresponding concentration quenching mechanism have been validated to be dipole-dipole interactions. Additionally, the Judd-Ofelt theory was selected to study the local structure environment of the Eu^{3+} ions in the $K_{0.3}Bi_{0.7}F_{2.4}$ host lattices and the tendency of J-O parameters ($\Omega_2 > \Omega_4$) confirm the asymmetric environment around Eu^{3+} ions. The thermogravimetric analysis and activation energy results of $K_{0.3}Bi_{0.7}F_{2.4}:Eu^{3+}$ materials with high thermal stability exhibit promising performances for temperature sensor applications. Moreover, the temperature-dependent of samples are investigated in a large temperature range of 303–573 K to explore thermal quenching performance. Signifcantly, luminescent temperature sensing has been accomplished by specifcally utilizing thermal quenching performance and high temperature sensitivity around $1.54 \times 10^4\ K^{-1}$ is achieved, which indicates that $K_{0.3}Bi_{0.7}F_{2.4}:Eu^{3+}$ fluorescent nanoparticles can be exploited for promising luminescent thermometer. Another important results are the $K_{0.3}Bi_{0.7}F_{2.4}:40\%Eu^{3+}$ nanoparticles exhibiting orange red emission with the CIE coordinates (0.6226, 0.3747) and the luminescence photographs of $K_{0.3}Bi_{0.7}F_{2.4}:Eu^{3+}$ samples under UV lamp (365 nm) irradiation revealing obvious orange red. Besides, the color purity of orange red $K_{0.3}Bi_{0.7}F_{2.4}:Eu^{3+}$ phosphor is demonstrated to be about 98.4%, which indicate that the as-prepared $K_{0.3}Bi_{0.7}F_{2.4}:Eu^{3+}$ phosphors may be a candidate component applied in UV w-LEDs.

（2）采用高温固相法制备了 $CaZrO_3:4.0\%Yb^{3+}/\ 0.2\%\ Er^{3+}/\ x\%\ Tm^{3+}$ (x = 0.2, 0.3, 0.4, 0.5, 0.6, 1.0, 1.4, 1.8)荧光粉。XRD 结果证实了 Yb^{3+},Er^{3+}和 Tm^{3+}的引入没有带来任何明显的晶体结构变化。通过改变 Er^{3+}和 Tm^{3+}的掺杂比例，证实了 Er^{3+}和 Tm^{3+}之间的能量传递。通过研究泵浦功率与发射强度的关系，证实了上转换绿、红、蓝发射的 n 值分别接近 2 和 3，说明这些发射分别是通过两步和三步光子顺序吸收过程完成的。此外,通过优化 Tm^{3+}离子的掺杂浓度和采用合适的泵浦功率,发射颜色可以调节到标准白光，位于 CIE（0.333，0.333）坐标处，该材料可潜在地应用在显示设备和激光领域。

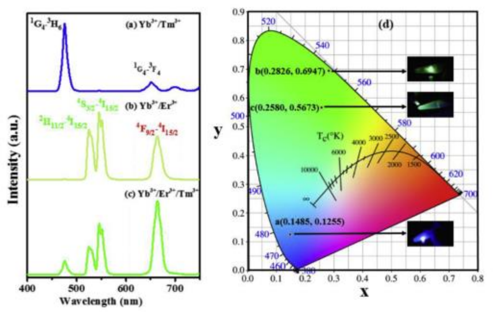

图 4. 上转换发射谱图：(a) $CaZrO_3:4.0\%Yb^{3+}/\ 0.2\%\ Tm^{3+}$，(b) $CaZrO_3:4.0\%Yb^{3+}/\ 0.2\%\ Er^{3+}$，(c) $CaZrO_3:4.0\%Yb^{3+}/\ 0.2\%\ Er^{3+}/\ 0.2\%\ Tm^{3+}$，(d)CIE 色坐标图。

Fig. 4 Upconversion Emission Spectra of (a) $CaZrO_3:4.0\%Yb^{3+}/\ 0.2\%\ Tm^{3+}$, (b) $CaZrO_3:4.0\%Yb^{3+}/\ 0.2\%\ Er^{3+}$, (c) $CaZrO_3:4.0\%Yb^{3+}/\ 0.2\%\ Er^{3+}/\ 0.2\%\ Tm^{3+}$under the excitation of 980 nm diode laser (laser working current 1.5 A (3000 mW)), (d) represents the CIE chromaticity diagram for blue, green and bluish green are shown respectively.

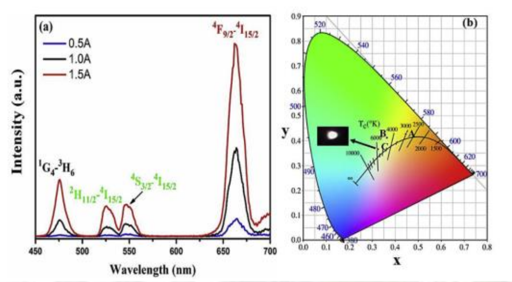

图 5. (a) $CaZrO_3:4.0\%Yb^{3+}/\ 0.2\%\ Er^{3+}/\ 1.8\%\ Tm^{3+}$上转换发射

谱图，(b) 在不同电流的 980 nm 激发光源激发下的 CIE 色坐标。

Fig. 5. (a) Upconversion emission spectra of $CaZrO_3$:4.0%Yb^{3+}/ 0.2% Er^{3+}/ 1.8% Tm^{3+} under the excitation of 980 nm diode laser. (b) Corresponding color chromaticity diagram under 980 nm diode laser excitation indicated as point A (0.5 A), point B(1.0 A) and point C (1.5 A). The inset is the white light corresponding to 1.5 A (3.0 W).

Using the high temperature solid state reaction method $CaZrO_3$:4.0%Yb^{3+}/ 0.2% Er^{3+}/ x% Tm^{3+}(x =0.2, 0.3, 0.4, 0.5, 0.6, 1.0, 1.4, 1.8) mol% phosphors are successfully fabricated. The XRD results were in agreement with the standard JCPDS card # 35-0645 for $CaZrO_3$ and the introduction of Yb^{3+}, Er^{3+} and Tm^{3+} did not bring any obvious change in the crystal structure of the host matrix. The intensities of green and red emission band of Er^{3+} ions decreases with increasing the dopage concentration of Tm^{3+} ions, which confirms energy transfer between Er^{3+} and Tm^{3+} ions. The increase in the intensity of blue emission may be ascribed to the increased population of $^1G_4$ level of Tm^{3+} contents less than 0.4 mol %. The IP plots showed a direct relation between the laser pump power and the upconversion emission intensity, the value of n for the upconversion green, red and blue emissions approaches two and three suggesting that these emissions have been accomplished by two-step and three-step photons sequential absorption process, respectively. Furthermore, by optimizing the doping concentration of Tm3þ ions and employing a proper pump power, the emission color is tuned to white light which is close to the standard CIE coordinates x= 0.333, y=0.333 on a standard CIE chromaticity diagram, indicating the practical applications of the prepared phosphor in display devices and laser fields.

（3）首次在室温下快速合成镧系离子(Yb^{3+}/Er^{3+})掺杂的 $K_{0.3}Bi_{0.7}F_{2.4}$ 荧光纳米粒子，有望应用于发光温度传感器。此外，首次详细研究了不同反应条件下制备的 $K_{0.3}Bi_{0.7}F_{2.4}$ 纳米粒子的晶体结构和形貌，包括反应时间和 Bi 源与 NH_4F 的不同摩尔比。此外，利用基于荧光强度比技术的发光温度计研究了 Yb^{3+}/Er^{3+}掺杂 $K_{0.3}Bi_{0.7}F_{2.4}$ 矩阵。$K_{0.3}Bi_{0.7}F_{2.4}$:Yb^{3+}/Er^{3+}表现出了优异的上转换发光性能，根据上转换发射强度与泵浦功率密度的函数关系，确定了样品的上转换机理。同时，研究了样品在 323-523k 温度范围内的光学测温性能，以考察温度传感器的性能。值得注意的是，所研究的纳米粒子在 523 K 时的最大传感器灵敏度为 0.0058 K^{-1} (Sa)，在 323 K 时的最大传感器灵敏度为 1.08 K^{-1} (Sr)，表明 $K_{0.3}Bi_{0.7}F_{2.4}$:20%Yb^{3+}/2%Er^{3+}荧光纳米粒子可作为一种有前景的发光温度计。

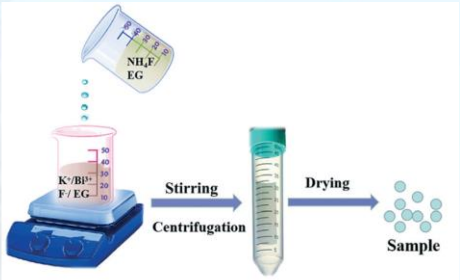

图 6. $K_{0.3}Bi_{0.7}F_{2.4}$ 制备流程图。

Fig. 6 Schematic for the preparation process for $K_{0.3}Bi_{0.7}F_{2.4}$ nanoparticles.

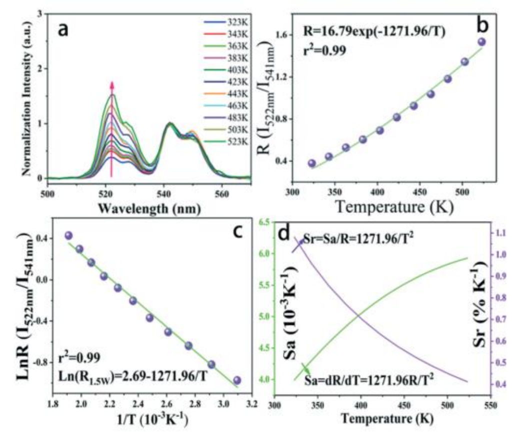

图 7. (a)$K_{0.3}Bi_{0.7}F_{2.4}$:20%Yb^{3+},2%Er^{3+}纳米粒子在 980 nm 激发下(激光功率= 1.5 W)随温度变化的归一化绿色发射光谱，(b) R 和绝对温度的关系，(c) Ln(R)作为绝对温度逆函数的序列图，(d) $K_{0.3}Bi_{0.7}F_{2.4}$:20%Yb^{3+},2%Er^{3+}纳米粒子的灵敏度随绝对温

度的变化。

Fig. 7 (a) Temperature-dependent normalized green emission spectra of $K_{0.3}Bi_{0.7}F_{2.4}$:20%Yb^{3+},2%Er^{3+} nanoparticles under 980 nm excitation (laser power = 1.5 W). (b) Relationship between R and the absolute temperature. (c) Monolog plots of Ln(R) as a function of inverse absolute temperature. (d) The sensitivity of $K_{0.3}Bi_{0.7}F_{2.4}$:20%Yb^{3+},2%Er^{3+} nanoparticle as a function of absolute temperature.

An ultrafast route at room temperature has been developed for the first time to synthesize lanthanide ion (Yb^{3+}/Er^{3+})-activated $K_{0.3}Bi_{0.7}F_{2.4}$ fluorescent nanoparticles and hold the potential to be applied in luminescent temperature sensors. In addition, the crystal structure and morphology of the $K_{0.3}Bi_{0.7}F_{2.4}$ nanoparticles prepared at different reaction conditions were studied in detail for the first time, including the reaction time and different mole ratios of Bi source and NH_4F. Moreover, Yb^{3+}/Er^{3+} doped in the $K_{0.3}Bi_{0.7}F_{2.4}$ matrix using a luminescent thermometer based on the fluorescence intensity ratio technology was also investigated. Additionally, $K_{0.3}Bi_{0.7}F_{2.4}$:Yb^{3+}/Er^{3+} revealed excellent up-conversion luminescence performance, and the up-conversion mechanisms of samples are affirmed according to the up-conversion emission intensity as a function of the pump power density. Simultaneously, the optical thermometric performance of the samples was investigated in the temperature range of 323-523 K to indagate the temperature sensor performance. Significantly, the maximum sensor sensitivity of the studied nanoparticles were 0.0058 K^{-1} (Sa) at 523 K and 1.08 K^{-1} (Sr) at 323 K, which indicates that $K_{0.3}Bi_{0.7}F_{2.4}$:Yb^{3+}/Er^{3+} fluorescent nanoparticles can be exploited as a promising luminescent thermometer.

（4）MXene 材料的光电性质及其应用
Photoelectric properties and applications of MXene

MXene 是一类与石墨烯相似的二维纳米材料。这类材料通常具有较好的机械性能、电学性能、磁学性能和光学性能，最重要的是，它们具有出色的化学性能。通常，MXene 是通过利用强酸刻蚀其前驱体 MAX 相制备的，由于该反应在溶液中发生，会使 MXene 表面结合大量表面终端，使其具有良好的生物相容性。此外，MXene 材料的层间可以插入不同的大分子或离子，使其层间距及性能可以发生相应的改变。这种良好的可调节性是石墨烯等其他材料不具有的。这些出色的性质使得 MXene 材料被广泛应用于超级电容器、电化学储能、电磁干扰屏蔽、传感器、生物医药、可再生能源和环境保护等各个领域。Ti3C2Tx 是使用最广泛的 MXene 材料之一。课题组主要对 Ti3C2Tx 的制备过程进行了研究，并将 Ti3C2 材料应用于表面增强拉曼光谱、外泌体检测和环保等领域。

MXene is a type of two-dimensional nanomaterial similar to graphene. Such materials usually have good mechanical properties, electrical properties, magnetic properties and optical properties, and most importantly, they have excellent chemical properties. Generally, MXene is prepared by etching the MAX phase of its precursor with a strong acid. Since this reaction occurs in a solution, the surface of MXene will be bound to a large number of surface terminals, making it have good biocompatibility. In addition, different macromolecules or ions can be inserted between the layers of MXene material, so that the layer spacing and properties can be changed accordingly. This good adjustability is not available in other materials such as graphene. These excellent properties make MXene materials widely use in various fields such as supercapacitors, electrochemical energy storage, electromagnetic interference shielding, sensors, biomedicine, renewable energy and environmental protection. Ti3C2Tx is a kind of material which widely utilizes the MXene materials. We mainly studied the preparation process of Ti3C2 MXene, and applied Ti3C2 material to the fields of surface enhanced Raman spectroscopy (SERS), exosome detection and environmental protection.

用拉曼光谱分析对化学湿法刻蚀制备 Ti3C2 的整体过程进行了表征。实验过程中，我们选用了 HF 和 HCl + LiF 两种刻蚀剂，对制备过程中的产物进行拉曼分析。结果表明，这两种刻蚀过程虽然反应原理相同，但其物质变化过程却略有不同。我们还发现在这两种过程中的某些特定时间段，不含表面终端的纯净 Ti3C2 纳米片含量极高。制备不含表面官能团的 MXene 薄片仍是当前研究的一大难点，而这些特定时间段的产物可以近似认为纯净，对于相应的实验研究有重要意义。

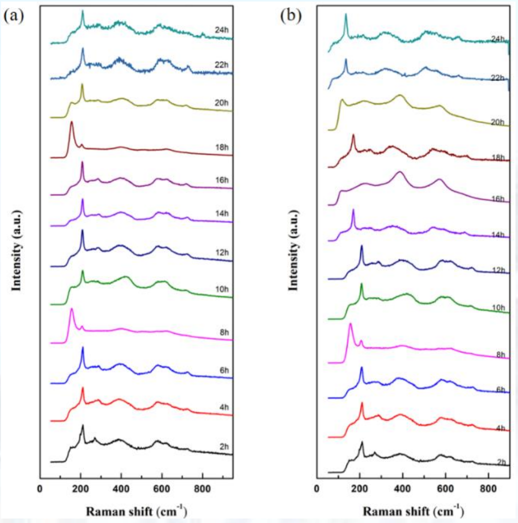

图 8. (a) 氢氟酸直接刻蚀过程中每 2h 产物的拉曼光谱；(b) HCl + LiF 原位刻蚀过程中每 2h 产物的拉曼光谱。

The overall process of preparing Ti3C2Tx by chemical wet etching was characterized by SEM(scanning electron microscope), EDS(Energy Dispersive Spectrometer) and Raman Spectroscopy. During the experiment, we chose two etching agents, namely HF and HCl + LiF, and then conducted a comparative study on these samples by Raman spectroscopy. The results show that although the two etching processes have the same reaction principle, the material change process is slightly different. We also found that during some specific time periods in these two processes, the content of pure Ti3C2Tx nanosheets without surface terminations is extremely high. The preparation of MXene flakes without surface functional groups is still a major difficulty in current research, and the products of these specific time periods can be approximated as pure, which is of great significance for the corresponding experimental research.

由于 Ti3C2Tx 纳米片具有较好的电子传输特性和等离子体特性，我们创新地使用了 Ti3C2Tx@Ag 用于 SERS 基底进行了拉曼增强实验。以 R6G 分子为指示剂，对比了 AgNPs、Ti3C2Tx 和 Ti3C2Tx@Ag 三种基底的 SERS 效应后发现，Ti3C2Tx@Ag 基底对 R6G 溶液增强效果最好，对 R6G 溶液的检测限可低至 10^{-10} mol/L。

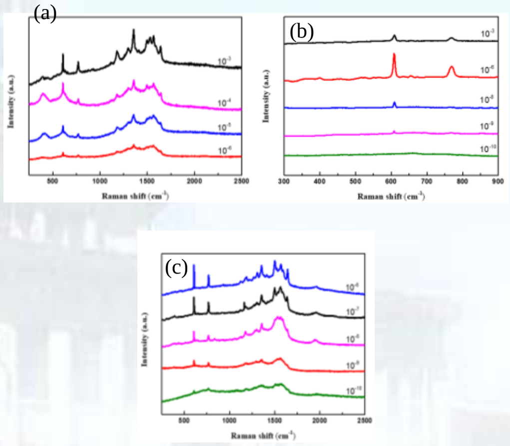

图 9. (a) AgNPs 对不同浓度的 R6G 的 SERS；(b) Ti3C2Tx 作为 SERS 基底检测不同浓度 R6G 溶液；(c) Ti3C2Tx@Ag 基底检测不同浓度 R6G 的拉曼光谱图。

Because Ti3C2Tx nanosheets have good electron transmission and plasma characteristics, we innovatively used Ti3C2Tx@Ag for SERS substrates to conduct Raman enhancement experiments. Using R6G molecules as indicators, comparing the SERS effects of AgNPs, Ti3C2Tx and Ti3C2Tx@Ag substrates, it is found that Ti3C2Tx@Ag substrate has the best enhancement effect on

R6G solution, and the detection limit of R6G solution can be as low as 10-10 mol/L.

Ti3C2Tx 具有良好的生物相容性，因此我们将其用于外泌体检测。对于小鼠乳腺癌（4T1）源外泌体和人类胚胎干细胞（UC）源外泌体，Ti3C2Tx 展现出良好的荧光淬灭效应，极少量的 Ti3C2Tx 就可以使其荧光信号的强度发生较大的下降。此外，以 Ti3C2Tx@Ag 为增强基底，可以有效地使人类胚胎干细胞源（UC）外泌体的拉曼信号得到有效增强。

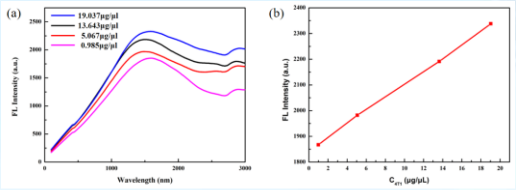

图 10. (a)不同浓度的 4T1（小鼠乳腺癌来源）外泌体的荧光光谱图；(b)4T1 外泌体的荧光强度随浓度的变化关系。

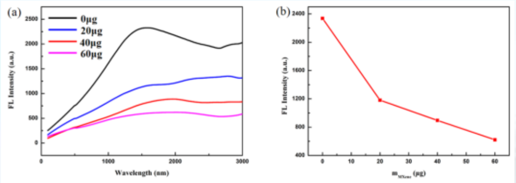

图 11. (a)向浓度为 19.037 μ g/μL 的 4T1 外泌体中加入不同质量 MXene 后的荧光光谱；(b)4T1 外泌体的荧光强度与加入 MXene 质量的关系。

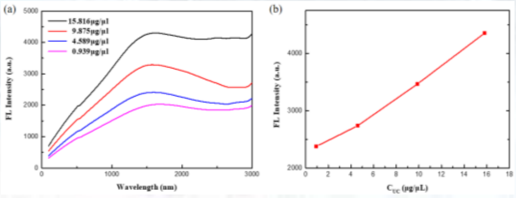

图 12. (a)不同浓度的 UC（人类胚胎干细胞源）外泌体的荧光光谱图；(b)UC 外泌体的荧光强度随浓度的变化关系。

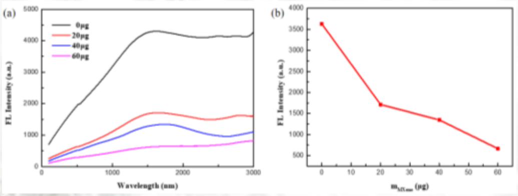

图 13. (a)向浓度为 15.816 μ g/ μ L 的 UC 外泌体中加入不同质量 MXene 后的荧光光谱；(b)UC 外泌体的荧光强度

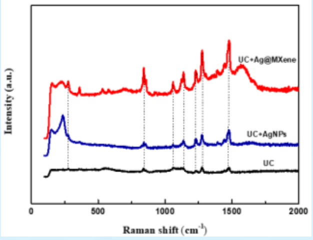

图 14. AgNPs 和 Ti3C2Tx@Ag 基底对 UC（人类胚胎干细胞源）外泌体的 SERS。

Ti3C2Tx has good biocompatibility, so we use it for exosome detection. For mouse breast cancer source (4T1) exosomes and human embryonic stem cell source (UC) exosomes, Ti3C2Tx exhibits a good fluorescence quenching effect, and a very small amount of Ti3C2Tx can make the intensity of its fluorescence signal greater decline. In addition, using Ti3C2Tx@Ag as the enhanced substrate can effectively enhance the Raman signal of human embryonic stem cell source (UC) exosomes.

将 Ti3C2Tx 材料用于污水处理。我们以红墨水和蓝墨水模拟有机污染物，分析 Ti3C2Tx 对于紫外光催化有机染料分解的反应过程的影响。结果表明，相对于单纯使用紫外光照射染料有机分子水溶液进行光催化，Ti3C2Tx 的加入，能够有效地提高反应剧烈程度，进而能够有效的地缩短反应时间。其中，Ti3C2Tx 的加入对于蓝墨水的褪色反应有更好的催化作用，反应时间有效缩短 30%以上。

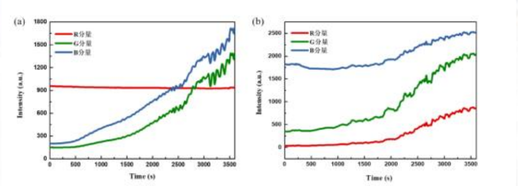

图 15. (a)汞灯光催化分解红墨水水溶液 RGB 变化曲线；(b)汞灯光催化分解蓝墨水水溶液 RGB 变化曲线。

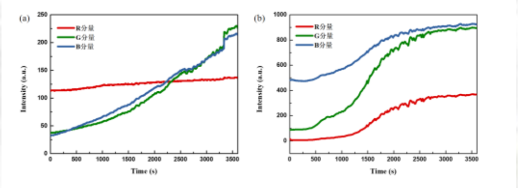

图 16. (a)汞灯+MXene 光催化分解红墨水水溶液 RGB 变化曲

线；(b)汞灯+MXene 光催化分解蓝墨水水溶液 RGB 变化曲线。

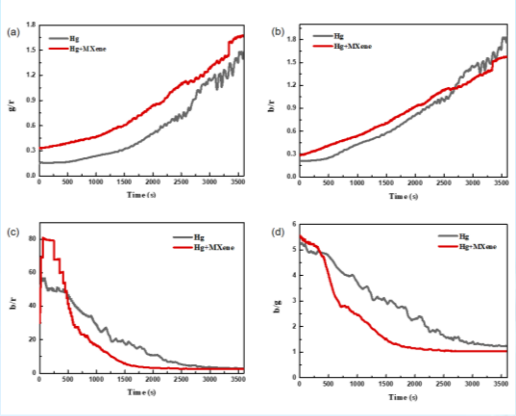

图 17. (a)和(b)分别为加入 MXene 前后红墨水褪色过程中 g/r 和 b/r 随时间变化曲线；(c)和(d)分别为加入 MXene 前后蓝墨水褪色过程中 b/r 和 b/g 随时间变化曲线。

Ti3C2Tx is used for sewage treatment. We simulated organic pollutants with red ink and blue ink, and analyzed the effect of Ti3C2Tx on the reaction process of UV photocatalytic organic decomposition. The results show that the addition of Ti3C2Tx can effectively increase the intensity of the reaction and shorten the reaction time, compared with the use of ultraviolet light to irradiate the aqueous solution of dye organic molecules. Among them, the addition of Ti3C2Tx has a better catalytic effect on the fading reaction of blue ink, and the reaction time is effectively shortened by more than 30%.

MXene 材料对有机物具有催化氧化作用，具有优良的导电性。我们制备了 MXene 修饰后的电极，通过实验确定最佳检测条件后，将修饰电极用于在最佳检测条件下测量不同浓度的葡萄糖溶液的 COD 值。实验结果证明葡萄糖浓度和 COD 浓度的对数呈线性关系。利用电化学方法检测 COD 浓度，在该实验中，使用了 MXene 改性的钛电极进行测量，与传统钛电极相比，该修饰电极具有更好的电化学性能，催化性能得到了显着提高，用恒电位稳态极化法测定的电性能得到了稳定的提高，将电信号直接转换为 COD 值，可以减少二次污染，实现了快速批量，方便检测的要求，在环境监测方面具有一定的实用意义。

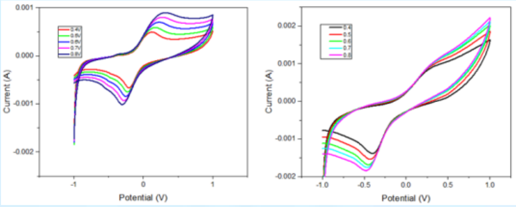

图 18. (a) 不同扫描速率的 Ti 电极的 C-V 图；(b) 不同扫描速率的 Ti-Mxene 电极的 C-V 图。

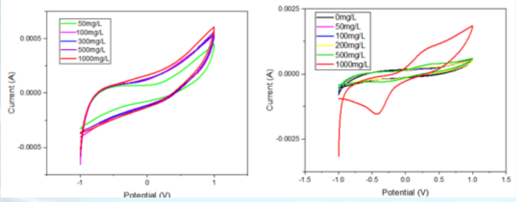

图 19. (a) 葡萄糖溶液中的循环伏安曲线；(b) 铁酸钾溶液中的循环伏安曲线。

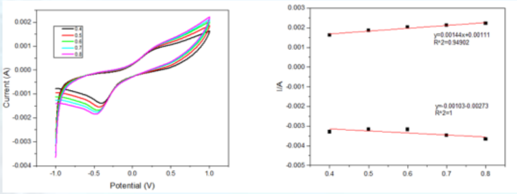

图 20. (a) 铁氰化物体系中不同扫描速率的 CV 曲线；(b)峰值电流和 CV 图中的扫描速率之间的对应关系。

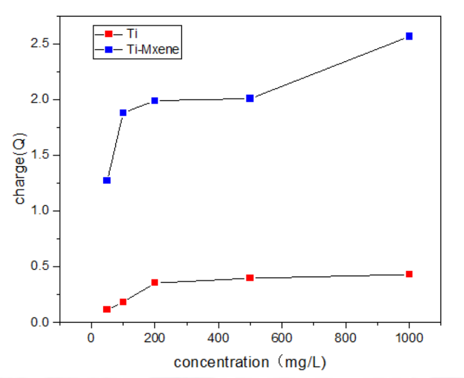

图 21. Ti 电极和 Ti-MXene 电极上不同浓度的葡萄糖和电量之间的关系。

The MXene material has a catalytic oxidation effect on organic matter. After the optimal detection conditions are determined, the modified electrodes are used to measure the COD values of glucose solutions with different concentrations under the optimal detection conditions. The logarithm of the glucose concentration and the COD concentration can be obtained in a linear relationship. The electrochemical method is used to detect the COD concentration. In the process, the electrical signal is directly converted into COD value, which can reduce secondary pollution and realize the requirement of rapid batch and convenient detection. In this experiment, the MXene modified titanium electrode is used for measurement. Compared with the titanium electrode, the modified electrode has better electrochemical performance and catalytic performance have been significantly improved, and the electricity has been steadily improved when measured by the constant potential steady-state polarization method.

（5）多光谱成像技术在遥感中的应用
Application of multispectral imaging technology in remote sensing

课题组设计了一种可以以高频率采集可见光-近红外区域图像、并自动追踪目标的被动式遥感仪器。该仪器分为图像采集模组、目标追踪模组和数据处理与传输模组图像采集模组采用 6×6 单元阵列，每个单元均由镜头+滤光片+CCD+树莓派构成，滤光片范围分别为可见光-近红外波段；采用多镜头分立式图像采集方法解决了多光谱技术中时间分辨率和光谱分辨率相互制约的限制问题。目标追踪部分将图像采集部分集成到一个二维云台上，通过横向和纵向两个步进电机控制云台的转向。电机又通过串口由服务器端控制。仪器设备可实现手动调整和自动调整，即预先设定轨道，以既定轨道开始运行，并同时拍摄图像。在数据处理与传输部分中，数据通过网络接口，将图像同时传输到服务器中，并由服务器完成图像处理的工作。包括 RAW 格式数据转换、图像融合等。

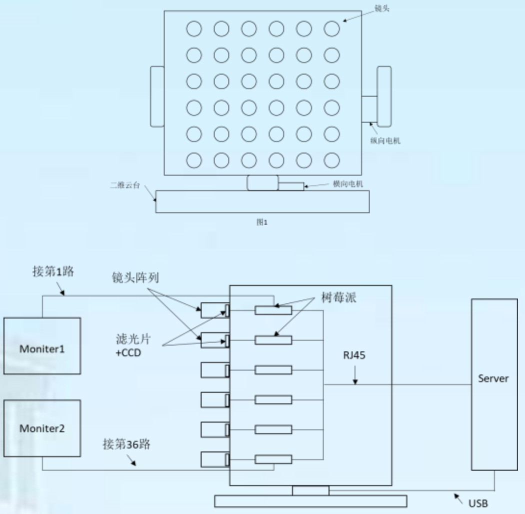

图 22. 成像光谱仪结构图。

Fig. 22 Imaging spectrometer structure diagram.

A kind of passive remote sensing instrument is designed, which can capture the visible near infrared image with high frequency and track the target automatically. There are three parts in this instrument, they are image acquisition part, target tracking part and data processing & transmission part. The instrument adopts 6 × 6 unit array, each unit is composed of lens + filter + CCD + Raspberry pie. Among the 36 units, the minimum wavelength is 360nm, the maximum wavelength is 910nm. In order to improve the signal-to-noise ratio (SNR) and indirectly improve the spatial resolution, the multi lens vertical image acquisition method is used to solve the problem of mutual restriction between temporal resolution and spectral resolution in multispectral technology. The image acquisition part of the instrument is integrated into a two-dimensional PTZ, and the steering of the PTZ is controlled by two horizontal and vertical stepping motors. The motor is controlled by the server through the serial port. It can realize manual adjustment and automatic adjustment, that is, preset the track, start running with the established track, and take images at the same time. After the completion of the data acquisition part, through the RJ45 interface, the 36 channels images are transferred to the server, at the same time the server completes the image processing, including RAW format data conversion, image fusion and so on.

（6）基于机器学习算法的近红外光谱数据分析方法研究 Research on near infrared spectroscopy data analysis method based on machine learning algorithm

我们编写了近红外光谱数据处理软件。该软件基于机器学习算法，能够有效建立模型，通过卷积神经网络和支持向量机算法，分析近红外光谱数据，进而定性完成分类任务或者定量完成成分计算任务。我们将该数据处理方法应用于粪水中的总磷总氮检测、塑料垃圾分类、海鱼品种快速鉴别等。

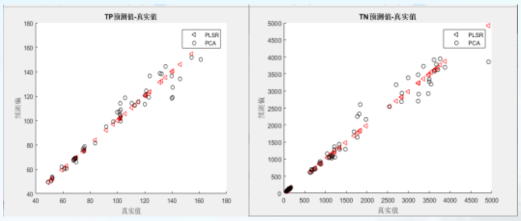

图 23. 训练集拟合结果（粪水中的总磷总氮检测）。

Fig. 23 Fitting results of training set (the detection of total phosphorus and nitrogen in fecal water).

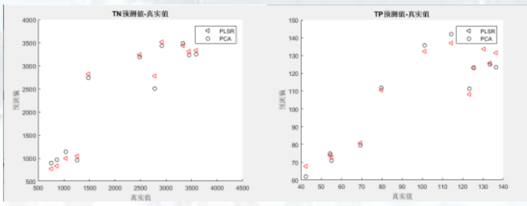

图 24. 预测集分析结果（粪水中的总磷总氮检测）。

Fig. 24 Analysis results of predictive set (the detection of total phosphorus and nitrogen in fecal water).

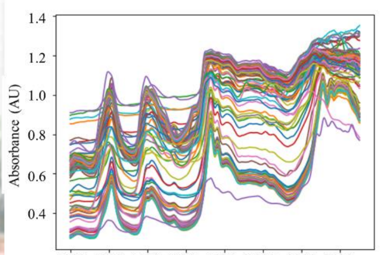

图 25. 塑料样品近红外光谱。

Fig. 25 Spectra of plastic samples.

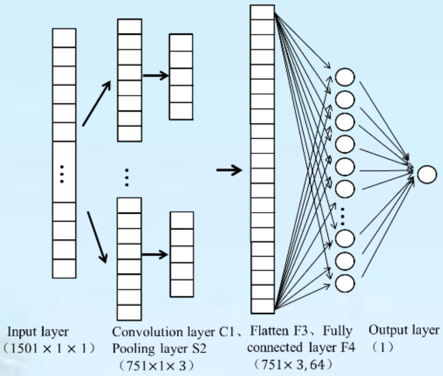

图 26. CNN 模型各层结构示意图。

Fig. 26 Representation of one-dimensional Convolutional Neural Network (1DCNN) architecture.

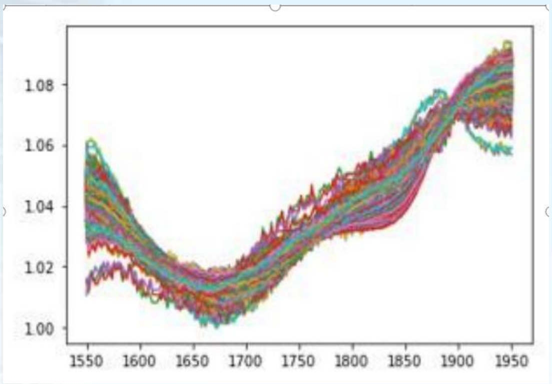

图 27. 经多元散射校正处理后光谱（海鱼品种快速鉴别）。

图 27. Spectrua after multivariate scattering correction processing (rapid identification of marine fish species).

We have compiled the near infrared spectrum data processing software. Based on machine learning algorithm, the software can effectively establish the model, analyze the NIR spectral data through convolution neural network and support vector machine algorithm, and then qualitatively complete the classification task or quantitatively complete the component calculation task. We applied the data processing method to the detection of total phosphorus and nitrogen in fecal water, the classification of plastic waste, and the rapid identification of marine fish species.

（7）超分辨成像及超分辨拉曼光谱 Super resolution imaging and Raman spectroscopy

在生产复杂的多维立体结构方面，3D

激光打印技术具有突出的灵活性和保真度，它极大地发展了生产多功能的设备。然而，手性纳米发射器严重依赖于同时表现出有效发射和严格限制的光-物质相互作用的人工结构，这是很吸引人的，但对这项技术来说，目前仍具有巨大的挑战。在我们的工作中，通过双三维激光打印光学二元性的银纳米结构一次实现手性光致发光。这种激光打印通过同时产生均匀分布的荧光银纳米团簇和聚集的等离子体银纳米粒子来严格限制纳米尺度上的手性相互作用，从而实现高度理想的二象性。所制备的螺旋直径为 550 nm 的螺旋发射体具有创纪录的各向异性因子，其绝对值可达 0.58，比荧光手性银团簇高出两个数量级。这种方法在未来的手化学纳米器件中具有广泛的应用前景。

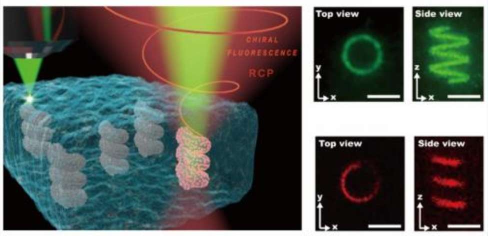

图 28. 三维激光打印实现银纳米结构的光学二象性及其手性荧光。

Fig. 28 Great Chiral Fluorescence from Optical Duality Silver Nanostructures Enabled by 3D Laser Printing.

Featured by prominent flexibility and fidelity in producing sophisticated stereoscopic structures transdimensionally, three-dimensional (3D) laser printing technique has vastly extended the toolkit for delivering diverse functional devices. Yet chiral nanoemitters heavily resorting to artificial structures that manifest efficient emission and tightly confined light-matter interactions simultaneously remains alluring but dauntingly challenging for this technique at this moment. In this work, we assert the chiral photoluminescence is implemented from silver nanostructures of optical duality in one go via a twofold three-dimensional laser printing scheme. Such laser printing protocol allows the highly desired duality by simultaneously producing uniformly distributed fluorescent silver nanoclusters and aggregated plasmonic silver nanoparticles to tightly confine chiral interactions at the nanoscale. A helical emitter of 550 nm-helix-diameter as fabricated has seen a record-high luminescence anisotropic factor with the absolute value up to 0.58, which is two orders of magnitude greater than fluorescent chiral silver clusters. This method holds great promise for future versatile applications in chiroptical nanodevices.

基于 pH 响应水凝胶，我们报告了一种可逆数据加密-解密技术，其中 pH 通道用于数据操作。在碱或酸的刺激下，水凝胶在响应 pH 值变化时表现出扩张或收缩。在水凝胶中预先掺杂银离子，通过直接写入和绘制银纳米点的图形，我们证明了数据输入可以在水凝胶平台中进行编码。通过这种方法，图像化的纳米点像素散射信号转换成二值化数字。同时，我们证明了水凝胶系统的阈值行为，即仅仅在有限的 pH 值范围内，被编码的等离子体图案可动态切换到光学可分辨/不可分辨的状态。通过精确匹配编码图案的像素间距和解密显微系统的衍射极限，可通过选择性施加酸和碱刺激实现可逆的亚衍射极限数据加密。该策略为光存储、多路数据操作和光数据安全提供了一个潜在的解决方案。

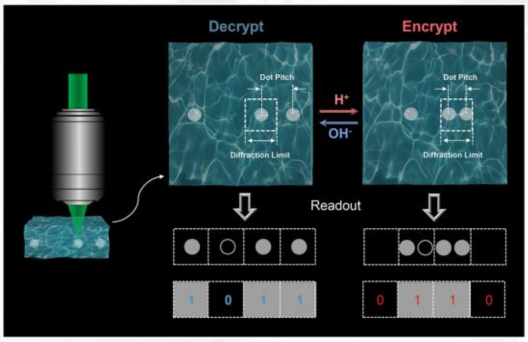

图 29. pH 刺激响应水凝胶的可逆数据加密解密。

Fig. 29 Reversible data encryption-decryption using pH stimuli-responsive hydrogel.

In this work, based on a ph-responsive

hydrogel, we report on a reversible data encryption-decryption technique where ph channel is employed for data manipulation. Upon alkali or acid stimulation, the hydrogel exhibits a network expansion or shrinkage in response to the ph variations. In particular, pre-doping the hydrogel with silver ions, we demonstrate that data input can be encoded in the hydrogel platform through direct writing and patterning of silver nanodots. By this means, the scattering signals from the patterned nanodot pixels are converted to the binarized data. Meanwhile, we show the threshold behaviour of the hydrogel system that dynamic switch of the encoded plasmonic pattern to optically resolvable/irresolvable state is viable only at finite ph key values. By delicately matching pixel spacings of the encoded pattern and the diffraction limit of the deciphering microscopic system, reversible sub-diffraction limit data encryption is achieved by selectively imposing acid and alkali stimulations. The suggested strategy offers a potential solution for optical storage, multiplexed data manipulation, and optical data security.

高折射率介电纳米结构支持多种丰富的电和磁 Mie 共振，可为将光物质相互作用集中在纳米级提供多功能的平台。通过整合无极子态的远场散射控制和近场集中的独特功能，在这里，我们展示了单个亚波长尺寸的硅纳米盘中巨大的光热非线性。纳米级能量集中和由无极子模式介导的近场增强产生具有大调制深度和宽动态范围的可逆非线性散射，揭示了在轻度入射光强度下(MW/cm2)高达 0.5 的创纪录高非线性指数变化。与非结构体硅相比，观察到的光热非线性显示出三个数量级的增强，并且比通过辐射电偶极模式产生的光热非线性显示出近一个数量级的增强。这种非线性散射可以在共聚焦反射成像中赋予独特的点扩散功能，从而为纳米结构 Si 的远场定位提供了可能，其精度接近 40 nm。我们的发现为基于光学偶极的有源硅光子学提供了新的思路。

Featured with a plethora of electric and magnetic Mie resonances, high index dielectric nanostructures offer a versatile platform to concentrate light-matter interactions at the nanoscale. By integrating unique features of far-field scattering control and near-field concentration from radiationless anapole states, here, we demonstrate a giant photothermal nonlinearity in single subwavelength-sized silicon nanodisks. The nanoscale energy concentration and consequent near-field enhancements mediated by the anapole mode yield a reversible nonlinear scattering with a large modulation depth and a broad dynamic range, unveiling a record-high nonlinear index change up to 0.5 at mild incident light intensities on the order of MW/cm2. The observed photothermal nonlinearity showcases three orders of magnitude enhancement compared with that of unstructured bulk silicon, as well as nearly one order of magnitude higher than that through the radiative electric dipolar mode. Such nonlinear scattering can empower distinctive point spread functions in confocal reflectance imaging, offering the potential for far-field localization of nanostructured Si with an accuracy approaching 40 nm. Our findings shed new light on active silicon photonics based on optical anapoles.

在这项研究中，使用圆柱矢量束来研究硅纳米结构的光热非线性。 我们通过用角向偏振矢量束选择性激发平面外 Mie 共振，观察到有效的非线性散射。由于激活的电多极模式的非共振激发，切换到径向偏振光束导致的散射非线性可忽略不计。由于 MD 增强的光热效应，具有足够高强度的方位偏振光束会引起 Si 纳米盘的强烈散射饱和。另外，密集堆积的硅纳米盘阵列的远场超定位显示了创纪录的 50nm FWHM，相当于 λ/ 11

精度。

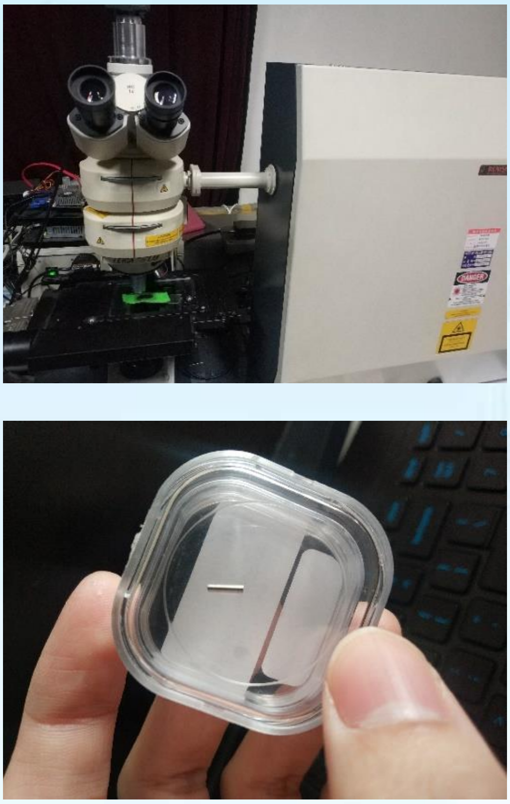

图 30. 基于单模光纤的共聚焦显微镜在小动物活体影像测量中的应用。

Fig. 30 Application of confocal microscope based on single mode optical fiber in image measurement of small animal in vivo.

In this study, cylindrical vector beams were implemented to investigate the photothermal nonlinearity of Si nanostructures. We observed efficient nonlinear scattering by selectively exciting the out-of-plane magnetic Mie resonances with an azimuthally polarized vector beam. Switching to the radially polarized beam resulted in negligible scattering nonlinearity owing to the off-resonance excitation of activated electric multipolar modes. The azimuthally polarized beam with sufficiently high intensities could induce strong scattering saturation of the Si nanodisks on account of the MD-enhanced photothermal effect. In addition, the far-field super-localization of densely packed Si nanodisk arrays showed a record-high 50 nm FWHM, corresponding to λ/11 precision.

（8）气体光学监测研究 Study on gas optical monitoring

课题组搭建了基于 TDLAS 技术的丙烷气体检测系统的实验装置。完成丙烷气体检测装置的参数调试以及预实验工作。我们使用中心波长为 3370nm 的激光器及中红外碲镉汞探测器。与此同时课题组完成了基于 NDIR 方法气体检测装置的算法设计工作。通过计算机设计 Goertzel 算法模拟处理探测装置输出信号，检验算法测量准确性。

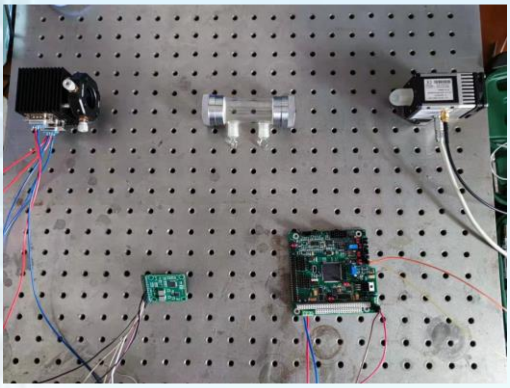

图 23. 丙烷气体检测装置图。

Fig. 23 The instrument selected for the propane gas detection device.

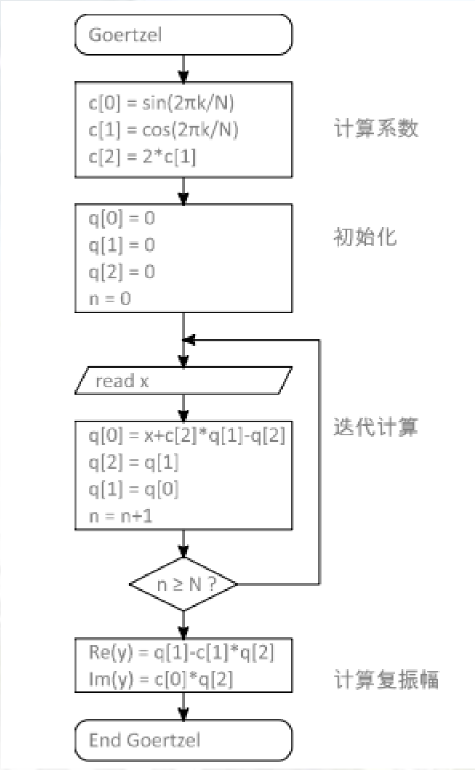

图 32. Goertzel 算法流程框图。

Fig. 32 Flow chart of Goertzel algorithm.

We set up an instrument for the propane gas detection device based on TDLAS technology. In this instrument we choose alaser with a center wavelength of 3370nm, and a mid-infrared mercury cadmium telluride detector. And we also complete the parameter adjustment and pre-experiment work of the propane gas detection device. We completed the algorithm design of the NDIR gas detection device, design the Goertzel algorithm to simulate the output signal of the detection device through the computer design, and verify the accuracy of the algorithm measurement.

发表论文/Publications in Journal

1. Fei Xie, Mengxin Ren*, Wei Wu, Dianqiang Yu, Wei Cai, Jingjun Xu*, Phase-transition optical activity in chiral metamaterials, *Phys. Rev. Lett.*, 125, 237401 (2020).

2. Mengxin Ren*, Wei Cai*, Jingjun Xu*, Tailorable dynamics in nonlinear optical metasurfaces. *Adv. Mater.*, 32, 1806317 (2020).

3. Fei Xie#, Wei Wu#, Mengxin Ren*, Wei Cai, Jingjun Xu*, Lattice collective interaction engineered optical activity in metamaterials, *Adv. Opt. Mater.*, 8, 1901435 (2020).

4. Song Huang, Qiang Wu*, Zixi Jia, Xiaorong Jin, Xianhui Fu, Hui Huang, Xiaodan Zhang, Jianghong Yao, Jingjun Xu, Black silicon photodetector with excellent comprehensive properties by rapid thermal annealing and hydrogenated surface passivation, *Adv. Opt. Mater.*, 8(7), 1901808 (2020).

5. Fulin Xing, Songyue Qu, Junfang Liu, Jianyu Yang, Fen Hu, Irena Drevenšek-Olenik, Leiting Pan*, Jingjun Xu, Intercellular bridge mediates Ca^{2+} signals between micropatterned cells via IP3 and Ca^{2+} diffusion, *Biophysical Journal*, 118, 1196-1204 (2020).

6. Li Li, Daping Zhao, Jiang Fan, Rong Huang, Wei Wu, Mengxin Ren, Xinzheng Zhang, Wei Cai, Jingjun Xu, Unveiling breathing plasmon modes in aluminum metal–insulator–metal cavities by cathodoluminescence", *J. Opt.*, 22, 035003 (2020).

7. Li Li, Lei Wang, Chenglin Du, Zhongyuan Guan, Yinxiao Xiang, Wei Wu, Mengxin Ren, Xinzheng Zhang, Aiwei Tang, Wei Cai, Jingjun Xu, Ultrastrong coupling of CdZnS/ZnS quantum dots to bonding breathing plasmons of aluminum metal-insulator-metal nanocavities in near-ultraviolet spectrum, *Nanoscale*, 12, 3112 (2020).

8. Lena Du, Cong Wang, Wenqi Xiong, Bin Wei, Fengyou Yang, Shengyao Chen, Lijun Ma, Xiaofeng Wang, Congxin Xia, Xinzheng Zhang*, Zhongchang Wang,* Qian Liu*, Strain-induced band-gap tuning of 2D-SnSSe flakes for application in flexible sensors, *Adv. Mater. Technol.*, 5(1), 1900853-8 (2020).

9. Shaohua Gao, Jiayi Wang, Wenhua Li, Xuanyi Yu, Xinzheng Zhang*, Xiao Song, Andrey Iljin*, Irena Drevensek -Olenik, Romano A. Rupp, Jingjun Xu*, Low threshold random lasing in dye-doped and strongly disordered chiral liquid crystals, *Photon. Res.*, 8(5), 642-647 (2020).

10. Yang Liu, Xiaodan Xu, Donghao Yang, Xinzheng Zhang*, Mengxin Ren, Nan Gong, Wei Cai*, Faheem Hassan, Zhimao Zhu, Irena Drevenšek-Olenik, Romano A. Rupp, Jingjun Xu*, Multifunctional and tunable trigate graphene metamaterial with "Lakes of Wada" topology, *Opt. Exp.*, 28(17), 24772-24788 (2020).

11. Junjun Ma#, Jiaxin Chen#, Mengxin Ren*, Wei Wu, Wei Cai*, Jingjun Xu*. Second harmonic generation and its nonlinear depolarization from lithium niobate thin films. *Opt. Lett.*, 45, 145 (2020).

12. Zixi Jia, Qiang Wu*, Xiaorong Jin, Song Huang, Jinze Li, Ming Yang, Hui Huang, Jianghong Yao, Jingjun Xu, Highly responsive tellurium-hyperdoped black silicon photodiode with single-crystalline and uniform surface microstructure, *Optics Express*, 28, 5239-5247 (2020).

13. Song Huang, Gongrong Deng, Xiaorong Jin, Yu Lu, Guanting Song, Hui Huang, Peng Zhao, Cunling Zhang, Jianghong Yao, Qiang Wu*, Jingjun Xu, The dark current suppression of black silicon photodetector by a lateral heterojunction, *Optical Materials*, 110, 110474 (2020).

14. Suyuan Wang, Qiang Wu*, Jun Zheng*, Bin Zhang, Song Huang, Zixi Jia, Jianghong Yao, Qingjun Zhou, Li Yang, Jingjun Xu, Buwen Cheng, Well-aligned periodic germanium nanoisland arrays with large areas and improved field emission performance induced by femtosecond laser, *Applied Surface Science*, 508, 145308 (2020).

15. Yuejian Jiao, Zhen Shao, Sanbing Li, Xiaojie Wang, Fang Bo, Jingjun Xu, Guoquan Zhang, Nano-domains produced through a two-step poling technique in lithium niobate on insulators, *Materials*, 13, 3617 (2020).
16. Li Zhang, Zhenzhong Hao, Qiang Luo, Ang Gao, Ru Zhang, Chen Yang, Feng Gao, Fang Bo*, Guoquan Zhang*, Jingjun Xu*, Dual-periodically poled lithium niobate microcavities supporting multiple coupled parametric processes, *Opt. Lett.*, 45(12), 3353-3356 (2020).
17. Shuting Kang, Ru Zhang, Zhenzhong Hao, Di Jia, Feng Gao, Fang Bo*, Guoquan Zhang*, Jingjun Xu*, High-efficiency chirped grating couplers on lithium niobate on insulator, *Opt. Lett.*, 45(24), 6651-6654 (2020).
18. Qiang Luo, Zhenzhong Hao, Chen Yang, Ru Zhang, Dahuai Zheng, Shiguo Liu, Hongde Liu, Fang Bo*, Yongfa Kong*, Guoquan Zhang*, Jingjun Xu*, Microdisk lasers on an erbium-doped lithium-niobite chip, *Sci. China. Phys. Mech.*, 64(3), 234263 (2020).
19. Zhenzhong Hao, Li Zhang, Wenbo Mao, Ang Gao, Xiaomei Gao, Feng Gao, Fang Bo*, Guoquan Zhang*, Jingjun Xu*, Second-harmonic generation using d_{33} in periodically poled lithium niobate microdisk resonators, *Photonics Res.*, 8(3), 311-317 (2020).
20. Junda Zhu, Haitao Liu*, Fang Bo*, Can Tao, Guoquan Zhang*, Jingjun Xu*, Intuitive model of exceptional points in an optical whispering-gallery microcavity perturbed by nanoparticles, *Phys. Rev. A*, 101(5), 053842 (2020).
21. Lu Zhang, Dongxu Zhou, Yiping Lu, Hongzhi Zhang, Guoquan Zhang*, Super-bunched focusing with chirped random-phase gratings, *Photonics Res.*, 8(4), 503-510 (2020).
22. Jianji Liu, Jiachen Liu, Ping Yu, Guoquan Zhang*, Sub-megahertz narrow-band photon pairs at 606 nm for solid-state quantum memories, *APL Photonics*, 5(6), 066105 (2020).
23. Jintian Lin, Fang Bo*, Ya Cheng*, Jingjun Xu*, Advances in on-chip photonic devices based on lithium niobate on insulator, *Photonics Res.*, 8(12), 1910-1936 (2020).
24. Yuejian Jiao, Zhen Shao, Sanbing Li, Xiaojie Wang, Fang Bo, Jingjun Xu, Guoquan Zhang*, Improvement on thermal stability of nano-domains in lithium niobate thin films, *Crystals*, 10(2), 74 (2020).
25. Xiaomei Gao, Lechen Yang, Fang Bo*, Jiafang Li*, Guoquan Zhang, Jingjun Xu, Vector beams in planar photonic crystal cavities with rotating air holes, *Opt. Lett.*, 45(6), 1587-1590 (2020).
26. X. Gao, L. Yang, H. Lin, L. Zhang, J. Li, F. Bo, Z. Wang, L. Lu*, Dirac-vortex topological cavities, *Nat. Nanotechnol.*, 15, 1012-1018 (2020).
27. Pengfa Chang, Botao Cao, Ligang Huang, Jiwei Li, Yue Hu, Feng Gao*, Wending Zhang, Fang Bo, Xuanyi Yu, Guoquan Zhang, Jingjun Xu*, Polarization-modified Fano line shape spectrum with a single whispering gallery mode, *Sci. China. Phys. Mech.*, 63(1), 214211 (2020).
28. Min Guo, Shiqi Xia, Nan Wang, Daohong Song, Zhigang Chen, Jianke Yang, Weakly nonlinear topological gap solitons in Su–Schrieffer–Heeger photonic lattices, *Opt. Lett.*, 45(23), 6466-6469 (2020).
29. Shiqi Xia, Dario Jukić, Nan Wang, Daria Smirnova, Lev Smirnov, Liqin Tang, Daohong Song, Alexander Szameit, Daniel Leykam, Jingjun Xu, Zhigang Chen, Hrvoje Buljan, Nontrivial coupling of light into a defect: the interplay of nonlinearity and topology, *Light: Science & Applications*, 9, 147 (2020).
30. Xiuying Liu, Shiqi Xia, Ema Jajtić, Daohong Song, Denghui Li, Liqin Tang, Daniel Leykam, Jingjun Xu, Hrvoje Buljan Zhigang Chen, Universal momentum-to-real-space mapping of topological singularities, *Nature Communications*, 11, 1586 (2020).
31. J. Ma, J. W. Rhim, L. Tang, S. Xia, H. Wang, X. Zheng, S. Xia, D. Song, Y. Hu, Y. Li, B.-J.

Yang, D. Leykam, Z. Chen, Direct observation of flatband loop states arising from nontrivial real-space topology, *Phys. Rev. Lett.*, 124, 183901 (2020).

32. Denghui Li, Domenico Bongiovanni, Michael Goutsoulas, Shiqi Xia, Ze Zhang, Yi Hu, Daohong Song, Roberto Morandotti, Nikolaos K. Efremidis, Zhigang Chen, Direct comparison of anti-diffracting optical pin beams and abruptly autofocusing beams, *OSA Continuum*, 3, 1525(2020).
33. Wenchao Yan, Hua Zhong, Daohong Song, Yiqi Zhang, Shiqi Xia, Liqin Tang, Daniel Leykam, Zhigang Chen, Flatband line states in photonic super-honeycomb lattices, *Adv. Optical Mater.*, 8, 1902174 (2020).
34. L. Tang, D. Song, S. Xia, S. Xia, J. Ma, W. Yan, Y. Hu, J. Xu, D. Leykam, Z. Chen, Photonic flat-band lattices and unconventional light localization, *Nanophotonics*, 9, 1161 (2020). (Invited Review).
35. S. Xia, C. Danieli, W. Yan, Z. Li, S. Xia, J. Ma, H. Lu, D. Song, L. Tang, S. Flach, Z. Chen, Observation of quincunx-shaped flatband states in photonic rhombic lattice without band-touching, *APL Photonics*, 5(1), 016107 (2020).
36. H. Wang, L. Tang, J. Ma, H. Hao, X. Zheng, D. Song, Yi Hu, Y Li, Z. Chen, optical clearing and shielding with fan-shaped vortex beams, *APL Photonics*, 5(1), 016102 (2020).
37. Pengbo Jia, Domenico Bongiovanni, Yi Hu, Roberto Morandotti, Zhigang Chen, Jingjun Xu, Direct reading of the nonlinear optical response via spatial mapping, *Phys. Rev. Applied*, 14, 064001 (2020).
38. Ping Zhang, Qianqian Kang, Yumiao Pei, Zhaoyuan Wang, Yi Hu, Zhigang Chen, Jingjun Xu, Unveiling chiral phase evolution in rabi oscillations from a photonic setting, *Phys. Rev. Lett.*, 125, 123201 (2020).
39. L. Li, Y. Jiang, P. Jiang, X. Li, Y. Qiu, P. Jia, Z. Pi, Y. Hu, Z. Chen, J. Xu, Experimental observation of three-dimensional non-paraxial accelerating beams, *Opt. Express*, 28, 17653 (2020).
40. Yumiao Pei, Zhaoyuan Wang, Yi Hu, Cibo Lou, Zhigang Chen, Jingjun Xu, Spontaneous diametric-drive acceleration initiated by a single beam in a photonic lattice, *Opt. Lett.*, 45, 3175 (2020).
41. Hua Cheng, Wenlong Gao*, Yangang Bi, Wenwei Liu, Zhancheng Li, Qinghua Guo, Yang Yang, Oubo You, Jing Feng, Hongbo Sun, Jianguo Tian, Shuqi Chen*, Shuang Zhang*, Vortical reflection and spiraling Fermi arcs with Weyl metamaterials, *Physical Review Letters*, 125, 093904 (2020).
42. Wenwei Liu, Dina Ma, Zhancheng Li, Hua Cheng, Duk-Yong Choi, Jianguo Tian, Shuqi Chen*, Aberration-corrected three-dimensional positioning with single-shot metalens array, *Optica*, 7, 1706 (2020).
43. Zhancheng Li, Wenwei Liu, Hua Cheng, Duk-Yong Choi, Shuqi Chen*, Jianguo Tian, Spin-selective full-dimensional manipulation of optical waves with chiral mirror, *Advanced Materials*, 32, 1907983 (2020).
44. Shuqi Chen*, Wenwei Liu, Zhancheng Li, Hua Cheng, Jianguo Tian, Metasurfaces empowered optical multiplexing and multifunction, *Advanced Materials*, 32, 1805912 (2020).
45. Zhi Li, Wenwei Liu, Guangzhou Geng, Zhancheng Li, Junjie Li, Hua Cheng, Shuqi Chen*, Jianguo Tian, Multiplexed nondiffracting nonlinear metasurfaces, *Advanced Functional Materials*, 30, 1910744 (2020).
46. Ruhao Pan, Zhancheng Li, Zhe Liu, Wei Zhu, Liang Zhu, Yunlong Li, Shuqi Chen, Changzhi Gu, Junjie Li, Rapid bending origami in micro/nanoscale toward a versatile 3D metasurface, *Laser Photonics Review*, 14, 1900179 (2020).

47. Jin Han, Yuttana Intaravanne, Aning Ma, Ruoxing Wang, Songtao Li, Zhancheng Li, Shuqi Chen, Jensen Li, Xianzhong Chen, Optical metasurfaces for generation and superposition of optical ring vortex beams, *Laser Photonics Review*, 14, 2000146 (2020).

48. Lin Chen, Tangxuan Ren, Yang Zhao, Qiang Yu, Zengli Huang, Kai Zhang, Jing Wen, Feng Lin, Shuqi Chen, Polarization‐independent wavefront manipulation of surface plasmons with plasmonic metasurfaces, *Advanced Optical Materials*, 8, 2000868 (2020).

49. Zhancheng Li, Wenwei Liu, Hua Cheng, Shuqi Chen*, Few-layer metasurfaces with arbitrary scattering properties, *Science China-Physics Mechanics & Astronomy*, 63, 284202 (2020).

50. Ye Wang, Wenwei Liu, Wei Xin*, Tingting Zou, Xin Zheng, Yanshuang Li, Xiuhua Xie, Xiaojuan Sun, Weili Yu, Zhibo Liu, Shuqi Chen*, Jianjun Yang*, Chunlei Guo*, Back-reflected performance-enhanced flexible perovskite photodetectors through substrate texturing with femtosecond laser, *ACS Applied Materials & Interfaces*, 12, 26614 (2020).

51. Zhancheng Li, Wenwei Liu, Chengchun Tang, Hua Cheng, Zhi Li, Yuebian Zhang, Junjie Li, Shuqi Chen*, Jianguo Tian, Bilayer plasmonic metasurface for polarization-insensitive bidirectional perfect absorption, *Advanced Theory and Simulations*, 3, 1900216 (2020).

52. Wenwei Liu, Hua Cheng, Shuqi Chen*, Jianguo Tian, Diffractive metalens: from fundamentals, practical applications to current trends, *Advances in Physics-X*, 5, 1742584 (2020).

53. Xiao-Guang Gao, Xiao-Kuan Li, Wei Xin, Xu-Dong Chen, Zhi-Bo Liu, Jian-Guo Tian, Fabrication, optical properties, and applications of twisted two-dimensional materials. *Nanophotonics*, **9** (7), 1717 (2020).

54. Zhen Hu, Zhibo Liu, Jianguo Tian, Stacking of exfoliated two-dimensional materials: a review. *Chinese Journal of Chemistry*, **38** (9), 981 (2020).

55. Xiaoqiang Jiang, Xiaokuan Li, Shaonan Chen, Baowang Su, Kaixuan Huang, Zhibo Liu, Jianguo Tian, Tunneling devices based on graphene/black phosphorus van der Waals heterostructures. *Materials Research Express*, **7** (1), 016310 (2020).

56. Xiaokuan Li, Ruoxuan Sun, Haowei Guo, Baowang Su, Dekang Li, Xiaoqing Yan, Zhbo Liu, Jianguo Tian, Controllable doping of transition-metal dichalcogenides by organic solvents. *Advanced Electronic Materials*, **6** (3), 1901230 (2020).

57. Ruoxuan Sun, Qinqin Guo, Haowei Guo, Xiaoqing Yan, Zhibo Liu, Jianguo Tian, Photoresponse in a strain-induced graphene wrinkle superlattice. *Journal of Physical Chemistry Letters*, **11** (13), 5059, (2020).

58. Haowei Guo, Zhen Hu, Zhibo Liu, Jianguo Tian, Stacking of 2D materials, *Advanced Functional Materials*, 30, 2007810 (2020).

59. Baowang Su, Xilin Zhang, Binwei Yao, Haowei Guo, Dekang Li, Xudong Chen, Zhibo Liu, Jianguo Tian, Laser writable multifunctional van der waals heterostructures, *Small*, 16(50), 2003593 (2020).

60. Huimin Chen, Yuxing Bai, Lirong Zheng, Li Wu*, Liwei Wu, Yongfa Kong, Yi Zhang*, Jingjun Xu, Interstitial oxygen defect induced mechanoluminescence in $KCa(PO_3)_3:Mn^{2+}$, *Journal of Materials Chemistry C*, 8, 6587-6594 (2020).

61. Huimin Chen, Li Wu*, Tongqing Sun, Rui Dong, Zhongzhong Zheng, Yongfa Kong, Yi Zhang*, Jingjun Xu, Intense green elastico-mechanoluminescence from $KZn(PO_3)_3:Tb^{3+}$, *Applied Physics Letters*, 116 (5), 051904 (2020).

62. Jinjin Liu, Hua Yu, Li Zhang, Haotian Dong, Shikang Liu, Lijuan Zhao, Controlling the final phase of multiphase $KGdF_4$ materials via chemical synthesis and structural phase transition, *Journal of Materials Science: Materials in Electronics*, 31(20), 18096-18104 (2020).

63. Yuting Fu, Lijuan Zhao, Yuao Guo, Hua Yu, A transparent and dual-functional oxyfluoride glass ceramics with color-tunable up-conversion luminescence and high thermosensitivity, *Journal of Luminescence*, 217, 116790 (2020).
64. YanlongYu, Pengchong Jiang, YabinYan, Hanbo Li, Lixin Zhang, Shan Jiang, WenshengYang, Ya’an Cao*, Animal heat activated cancer therapy by a traditional catalyst TiO_2-Pd/graphene composites, *Scientific Reports*, 10(1), 15823 (2020).
65. Hanbo Li, Lixin Zhang, Ya’an Cao*, Synthesis of palladium-modified MnS photocatalysts with enhanced photocatalytic activity in the photoreduction of CO_2 to CH_4, *Applied Surface Science*, 541, 148519 (2020).
66. Hanbo Li, Tongqing Sun, Lixin Zhang, Ya’an Cao*, Matching and adjusting energy band structures of Pd-modified sulphides (ZnS, In_2S_3 and CuS) and improving the photocatalytic activity of CO_2 photoreduction, *Nanoscale*, 12 (35), 18180-18192 (2020).
67. Xuewen Fu*, Erdong Wang, Yubin Zhao, Ao Liu, Eric Montgomery, Vikrant J. Gokhale, Jason J. Gorman, Chunguang Jing, June W. Lau, Yimei Zhu*, Direct visualization of electromagnetic wave dynamics by laser-free ultrafast electron microscopy, *Science Advances*, 6(40), eabc3456 (2020).
68. Xuewen Fu*, Francesco Barantani, Simone Gargiulo, Ivan Madan, Gabriele Berruto, Thomas LaGrange, Lei Jin, Junqiao Wu, Giovanni Maria Vanacore, Fabrizio Carbone*, Yimei Zhu*, Nanoscale-femtosecond dielectric response of Mott insulators captured by two-color near-field ultrafast electron microscopy, *Nature Communications*, 11(1), 5770 (2020).
69. Zhao Liu, Xuewen Fu, Dong-Bo Zhang*, Strain gradient induced spatially indirect excitons in single crystalline ZnO nanowires, *Nanoscale*, 12(37), 19083-19087 (2020).
70. Yang Zhong, Zhenpeng Hu, Tongqing Sun, Weiwei Wang, Yongfa Kong*, Jingjun Xu, Pauling’s rules guided Monte Carlo search (PAMCARS): A shortcut of predicting inorganic crystal structures, *Computer Physics Communications*, 256, 107486 (2020).
71. Weiwei Wang, Yang Zhong, Dahuai Zheng, Hongde Liu*, Yongfa Kong*, Lixin Zhang, Romano Rupp, Jingjun Xu*, p-Type conductivity mechanism and defect structure of nitrogen-doped $LiNbO_3$ from first-principles calculations, *Physical Chemistry Chemical Physics*, 22(1), 20 (2020).
72. Weiwei Wang, Hongde Liu*, Dahuai Zheng, Yongfa Kong*, Lixin Zhang, Jingjun Xu, Interaction between Mo and intrinsic or extrinsic defects of Mo doped $LiNbO_3$ from first-principles calculations, *Journal of Physics: Condensed Matter*, 32, 255701 (2020).
73. Yongfa Kong*, Fang Bo, Weiwei Wang, Dahuai Zheng, Hongde Liu, Guoquan Zhang, Romano Rupp, Jingjun Xu*, Recent progress in lithium niobate: optical damage, defect simulation, and on-chip devices, *Advanced Materials*, 32(3), 1806452 (2020).
74. Jihua Xu*, Yinqi Chen, Yuhua Yin, Run Jiang, Zheng Wang, Baohui Li, Influence of grafting point distribution on self-assembly morphology of aba triblock copolymer brush, *Acta Polymerica Sinica*, 51(6), 632 (2020).
75. Jingxue Zhang, Jiaping Wu, Run Jiang, Zheng Wang, Yuhua Yin, Baohui Li*, Qiang Wang*, Lattice self-consistent field calculations of confined symmetric block copolymers of various chain architectures, *Soft Matter*, 16(17), 4311-4323 (2020).
76. Yongbing Song, Run Jiang, Zheng Wang, Yuhua Yin*, Baohui Li, Anchang Shi, Formation and regulation of multicompartment vesicles from cyclic diblock copolymer solutions: a simulation study, *ACS Omega*, 5(16), 9366-9376 (2020).
77. Wenrong Qi, Rui Liu, Lingjun Kong, Zhouxiang Wang, Shuangyin Huang, Chenghou Tu, Yongnan Li, Huitian Wang, Pancharatnam–Berry geometric phase memory based on spontaneous parametric down-conversion, *Opt. Lett.*, 45, 384363 (2020).

78. Wenrong Qi, Rui Liu, Lingjun Kong, Zhouxiang Wang, Shuangyin Huang, Chenghou Tu, Yongnan Li, Huitian Wang, Double-slit interference of single twisted photons, *Chin. Opt. Lett.*, 18, 10 (2020).

79. Yongnan Li, Shu-Wei Huang, Bowen Li, Hao Liu, Jinghui Yang, Abhinav Kumar Vinod, Ke Wang, Mingbin Yu, Dimlee Kwong, Huitian Wang, Kenneth Kin Yip Wong, Chee Wei Wong*, Real-time transition dynamics and stability of chip-scale dispersion-managed frequency microcombs, *Light: Science & Applications*, 9, 52 (2020).

80. Lingjun Kong, Rui Liu, Wentong Qi, Zhouxiang Wang, Shuangyin Huang, Chenghou Tu, Yongnan Li, Huitian Wang, Asymptotical locking tomography of high-dimensional entanglement, *Chin. Phys. Lett.*, 37, 034204 (2020).

81. Yanlong Wang, Yang Zhang, Baozhong Li, Kun Luo, Kaiyuan Shi, Li Zhang, Yi Li, Tianjun Yu, Wentao Hu, Chenlong Xie, Yingju Wu, Lei Su, Xiao Dong, Zhisheng Zhao, Guoqiang Yang, Restacked melon as highly-efficient photocatalyst, *Nano Energy*, 77, 105124 (2020).

82. Tianyue Zhang, Yingche, Kaichen, Jian Xu, Yi Xu, Te Wen, Guowei Lu, Xiaowei Liu, Bin Wang, Xiaoxuan Xu, Yi Shiou Duh, Yu Lung Tang, Jing Han, Yaoyu Cao, Bai Ou Guan, Shi Wei Chu, Xiangping Li, Anapole mediated giant photothermal nonlinearity in nanostructured silicon, *Nature Communications*, 11, 3027 (2020).

83. Hongjing Wen, Shichao Song, Fei Xie, Bin Wang, Jian Xu, Ziwei Feng, Shiyu Wu, Jing Han, Bai-Ou Guan, Xiaoxuan Xu, Yaoyu Cao, Xiangping Li, Great chiral fluorescence from the optical duality of silver nanostructures enabled by 3D laser printing, *Materials Horizons*, 7(12), 3201-3208 (2020).

84. Adnan Khan, Feng Song*, Aihua Zhou, Xiaoli Gao, Ming Feng, Muhammad Ikram, Huimin Hu, Xu Sang, Lisa Liu, Tuning white light upconversion emission from $Yb^{3+}/Er^{3+}/Tm^{3+}$ triply doped $CaZrO_3$ by altering Tm^{3+} concentration and excitation power, *Journal of Alloys and Compounds*, 835, 155286 (2020).

85. Xiaoli Gao, Feng Song*, Dandan Ju, Aihua Zhou, Adnan Khan, Ziyu Chen, Xu Sang, Ming Feng Lisa Liu, Room-temperature ultrafast synthesis, morphology and upconversion luminescence of $K_{0.3}Bi_{0.7}F_{2.4}:Yb^{3+}/Er^{3+}$ nanoparticles for temperature-sensing application, *CrystEngComm*, 22, 7066 (2020).

86. Xiaoli Gao, Feng Song*, Adnan Khan, Ziyu Chen, Dandan Ju, Xu Sang, Ming Feng, Lisa Liu, Room temperature synthesis, Judd Ofelt analysis and photoluminescence properties of down-conversion $K_{0.3}Bi_{0.7}F_{2.4}:Eu^{3+}$ orange red phosphors, *Journal of Luminescence*, 230, 117707 (2021)

87. Aihua Zhou*, Feng Song, Feifei Song, Chengguo Min, Xiaobin Ren, Liqun An, Fengying Yuan, Yueting Qin, Xiaoli Gao, Tunable red-to-green emission ratio and temperature sensing properties of $NaLuF_4:Ho^{3+}/Yb^{3+}$ microcrystals by doping with Ce^{3+} ions, CrystEngComm, 22, 6831 (2020).

88. Shuai Sun, Yiping Xu*, Liyong Ren, Jiayu Xu , Tianxu Jia, Lei Zhang, Jianting Xiao , Bingchuan Wang, Wenxing Yang, Shubo Cheng , Fang Chen , Chengju Ma, Feng Song, Research on the gas refractive index sensing based on microfiber double-knot resonator with a parallel structure", *Optik - International Journal for Light and Electron Optics*, 204,164207 (2020).

89. Bingchuan Wang, Liyong Ren, Xudong Kong, Yiping Xu*, Kaili Ren, Wenxing Yang, Shubo Cheng, Fang Chen, Feng Song, Study on fabrication, spectrum and torsion sensing characteristics of microtapered long-period fiber gratings", *Optik - International Journal for Light and Electron Optics*, 207, 164445 (2020).

90. 胡芬，林洋，侯梦迪，胡浩丰*，潘雷霆*，刘铁根，许京军，"基于深度学习的细胞骨架图像超分辨重建"，*光学学报*, 40, 2410001 (2020).

91. 夏世强，唐莉勤，夏士齐，马继娜，燕文超，宋道红，胡毅，许京军，陈志刚，"平带光子

微结构中的新颖现象：从模式局域到实空间拓扑”，*物理学报*, 69(15),154207 (2020).

92. 进晓荣，吴强[*]，黄松，贾子熙，宋冠廷，周旭，姚江宏，许京军, “飞秒激光过饱和掺杂硅基光电探测器研究进展”，*激光与光电子学进展*, 57(11), 111430 (2020).

93. 王晓杰，张国权, “铌酸锂铁电畴工程及其应用”，*物理实验*, 40(8), 1005-4642 (2020).

94. 玛地娜，李智，程化，陈树琪*，“超表面多维光场调控及基于机器学习的优化,” *科学通报*, 65, 1824 (2020).

95. 孙军，郝永鑫，张玲，许京军，祝世宁，“铌酸锂晶体及其应用概述,” *人工晶体学报*, 49(6), 947-964 (2020).

专利/Patents

申请专利/ Patents Applied

[1] US16/839,079；System and method for determining second order nonlinear susceptibility of material；发明；Mengxin Ren, Junjun Ma, Jiaxin Chen, Wei Wu, Wei Cai, Jingjun Xu。南开大学（2020.4.6）

[2] CN202010945696.0；一种具有横向结硅基光电探测器的制备方法；发明；吴强，黄松，进晓荣，刘瑶瑶，宋冠廷，周旭，张春玲，姚江宏，许京军。南开大学（2020.9.10）

[3] CN202010945697.5；一种宽禁带半导体表面深亚波长周期性条纹结构的制备方法；发明；吴强，刘瑶瑶，王俞萱，杨明，姚江宏，许京军。南开大学（2020.9.10）

[4] CN202011438154；铌酸锂半导体结构及其制备方法；发明；张国权，钱月照，张煜晨，许京军。南开大学（2020.12.10）

[5] ONI20016206US；Microstructural Lens Array and Spatial Positioning Method Based on Microstructural Lens Array；发明；陈树琪，刘文玮，玛地娜，程化，田建国。南开大学（2020.08.05）

[6] CN202010672030.2；微结构透镜阵列和基于微结构透镜阵列的空间定位方法；发明；陈树琪，刘文玮，玛地娜，程化，田建国。南开大学（2020.08.05）

[7] CN201911362732.4；手性光学元件及光学加密方法；发明；陈树琪，李占成，程化，田建国。南开大学（2020.04.23）

[8] CN202010272147.1；手性光学元件、手性光学加密组件及手性元件设计方法；发明；李占成，陈树琪，程化，田建国。南开大学（2020.06.30）

[9] CN202010184540.5；氨合氟化硼酸锌基尼个体及其制备方法和用途；发明；孙同庆，马进勇，刘莉娜，刘宏德，刘士国，孔勇发。南开大学（2020.3.16）

[10] CN202011357454.6；一种玻璃管红外囚禁罩；发明；谭成章，徐晓轩。南开大学（2020.11.27）

[11] CN202010958399.X；一种荧光复合薄膜及其在激光清洗后的油漆检测中的应用；发明；宋峰，陈子禹，于溪，张康，冯鸣。南开大学（2020.9.14）

[12] CN202011435998.X；一种树脂基复合材料表面涂料的激光清洗方法；发明；宋峰，高日翔，刘汉雄，于溪，杨贺，刘丽飒。南开大学（2020.12.11）

[13] CN202011610131.3；一种基于红绿蓝三色数值分析铜基底污染物以及其激光清洗效果的方法；发明；宋峰，高日翔，刘汉雄，刘丽飒。南开大学（2020.12.31）

授权专利/ Patents Approved

[1] ZL201810379613.9；一种检测红细胞变形性的微流控芯片及其方法；发明；潘雷霆，荀爽，邢福临，许京军。南开大学（2020.6.2）

[2] ZL201710461601.6；一种激光诱导石墨烯微纳结构的加工方法及其系统；发明；张心正，许京军，石彬，徐晓丹，刘洋，任梦昕，蔡卫，吴强，伊瑞娜。南开大学（2020.11.27）

[3] ZL201710844768.0；一种宽带隙晶体材料表面微纳结构的制备方法；发明；吴强，栗亚南，李强，张春玲，姚江宏，齐继伟，许京军。南开大学（2020.6.26）

[4] ZL201910230839.7；一种矢量贝塞尔光束生成装置；发明；涂成厚，王珂，王强，张洪爽，李勇男，王慧田。南开大学（2020.5.22）

[5] ZL201910096306.4；一种集成化的矢量光场生成器；发明；刘瑞，孔令军，齐文荣，田倩倩，李勇男，涂成厚，王慧田。南开大学（2020.7.28）

[6] ZL201910210865.3；一种量子螺旋成像系统；发明；刘瑞，齐文荣，孔令军，王周祥，李勇男，涂成厚，王慧田。南开大学（2020.7.28）

[7] ZL201810245862.9；一种由甲胺碘铅和甲胺碘构成的红色荧光粉的制备方法和应用；发明；刘磊，武莉，张毅，邢志雪。南开大学（2020.8.4）

[8] ZL201810616911.5；一种功能复合电光Q开关；发明；孙军，许京军，张玲，商继芳。南开大学（2020.7.24）

[9] ZL201810046180.5；一种紫外线固化装置；发明；徐晓轩，王斌，梁菁，车颖，徐阳阳，时金蒙，文虹镜，杨江涛，林宝志。南开大学（2020.5.15）

[10] ZL201810046446.6；一种水质检测用采样装置；发明；王斌，徐晓轩，黄津辉，李强，车颖，梁菁，徐阳阳，文虹镜，时金蒙，马雨霏。南开大学（2020.5.15）

[11] ZL201810046179.2；一种纳米压印衬底固化装置；发明；徐晓轩，王斌，梁菁，车颖，徐阳阳，时金蒙，文虹镜，杨江涛，林宝志。南开大学（2020.5.19）

[12] ZL201810046108.2；一种烟管内检测装置；发明；徐晓轩，王斌，杨江涛，文虹镜，徐阳阳，车颖，梁菁，时金蒙，张卓。南开大学（2020.7.14）

[13] ZL201810046128.X；一种增强拉曼光谱信号的装置；发明；徐晓轩，王斌，文虹镜，时金蒙，车颖，梁菁，徐阳阳，杨江涛。南开大学（2020.7.28）

[14] ZL201810046199.X；一种固化纳米压印装置；发明；徐晓轩，王斌，梁菁，车颖，徐阳阳，时金蒙，文虹镜，杨江涛，林宝志。南开大学（2020.8.18）

[15] ZL201920986622.4；一种自动清洁的光学仪器窗口；实用新型；徐晓轩，王斌，董超，徐阳阳，张月颖，梁亦豪。常州恒先传感科技有限公司，南开大学（2020.6.19）

[16] ZL201920986639.X；一种有毒有害气体监测用近红外光谱分析仪；实用新型；徐晓轩，王斌，董超，张月颖，张文杰，梁菁。常州恒先传感科技有限公司，南开大学（2020.4.14）

[17] ZL201920966327.2；一种饲料品质快速检测用近红外分析仪；实用新型；徐晓轩，董超，王斌，车颖，张文杰，徐阳阳。常州恒先传感科技有限公司，南开大学（2020.4.14）

[18] ZL201920966286.7；一种基于迈克耳逊干涉仪原理的微型近红外光谱仪；实用新型；王斌，徐晓轩，董超，张月颖，徐阳阳，梁菁。常州恒先传感科技有限公司，南开大学（2020.4.14）

[19] ZL201920949472.X；一种基于NB-IoT数据传输的光谱仪；实用新型；王斌，徐晓轩，

董超，文虹镜，梁亦豪，车颖。常州恒先传感科技有限公司，南开大学（2020.6.19）

[20] ZL201920952650.4；一种用于显微镜显微成像用的近红外光谱仪；实用新型；王斌，徐晓轩，董超，徐阳阳，车颖，张月颖。常州恒先传感科技有限公司，南开大学（2020.4.14）

[21] ZL201920931850.1；一种纺织纤维的鉴别光谱装置；实用新型；王斌，徐晓轩，董超，梁菁，张文杰，文虹镜。常州恒先传感科技有限公司，南开大学（2020.4.14）

[22] ZL201920917890.0；一种高稳定的紫外可见近红外准连续光源系统；实用新型；王斌，徐晓轩，董超，车颖，梁亦豪，文虹镜。常州恒先传感科技有限公司，南开大学（2020.4.14）

[23] ZL201920916987.X；一种用于烟草检测的生产线用的近红外光谱仪；实用新型；董超，徐晓轩，王斌，梁菁，文虹镜，车颖。常州恒先传感科技有限公司，南开大学（2020.4.14）

[24] ZL201920892706.1；一种近红外光谱仪用测量探头；实用新型；董超，王斌，徐晓轩，文虹镜，梁菁，徐阳阳。常州恒先传感科技有限公司，南开大学（2020.4.14）

[25] ZL201920881502.8；一种适用于无人值守的自校准近红外光谱仪；实用新型；董超，王斌，徐晓轩，梁亦豪，张文杰，张月颖。常州恒先传感科技有限公司，南开大学（2020.4.14）

[26] ZL201610321341.8；一种稀土粒子掺杂的磷酸盐剥离微晶光纤；发明；宋峰，安双新。南开大学（20200424）

国际合作与交流/International Cooperation and Exchange

来访人员名单/Visitors List

序号	姓名	国家或地区	单位	技术职称	报告题目	来访时间	来访目的
1	俞钢	美国	Cbrite Inc. USA	教授	柔性探测器数模转换电路中的研发问题	2020.5.18	学术交流（线上）
2	杨延勇	英国	Renishaw Company U.K.	教授	拉曼光谱在生命科学的应用	2020.7.6	学术交流（线上）
3	杨延勇	英国	Renishaw Company U.K.	教授	拉曼与 AFM 联用中样品台的若干问题	2020.10.7	学术交流（线上）
4	Irena Olenik-Drevensek	斯洛文尼亚	斯特藩研究所	教授	Magnetically tuable surface properties of magnetoactive elastomers	2020.11.11	学术交流（线上）
5	Andrey ILJIN	乌克兰	乌克兰科学院物理所	教授	Nonlinear optical properties of hybrid liquid crystal cells	2020.11.18	学术交流（线上）

出访人员名单/Personnel Exchange Researchers List

序号	姓名	国家或地区	单位	职称或职位	出访时间	出访目的
1						
2						
3						

研究生交流情况/Personnel Exchange Students List

序号	姓名	国家或地区	单位	博士生/硕士生	出访时间	出访目的
1	江晓洁	美国	奥本大学	博士生	2019.10-	联合培养
2	黄凯旋	中国	中科院物理所	博士生	2020.9-	联合培养
3	文虹镜	中国	暨南大学	博士生	2020.1.1-2020.1.17 2020.9.13-2020.12.31	联合培养
4	车颖	中国	暨南大学	硕士生	2020.1.1-2020.1.17	联合培养

国内、国际会议报告/Talks at Conferences

1. Z. Chen, “Topological phenomena in Photonic Dirac lattices”, International Conference on Metamaterials and Nanophotonics (MetaNano20), Sep. (2020). (**Keynote talk**, online)

2. Qiang Wu, Jianghong Yao, Chunling Zhang, Jiwei Qi, Chongpei Pan, Fuhua Yang, Jingjun Xu, “Interaction of femtosecond laser with crystal materials-From THz chip to hyperdoped photodetector”, The 14th Asia (Shenzhen) international Laser Application Manufacturing Forum, Shenzhen, China, Oct. 12-15 (2020). (**Invited talk**)

3. Guoquan Zhang, Xiaojie Wang, Yuejian Jiao, Zhen Shao, Fang Bo, Jingjun Xu, “Nano-domain structures fabricated in lithium niobite crystals”, The 2nd International Conference on Optics and Photonics (NICE OPTICS 2020), Nice, France, Oct.12-14 (2020). (**Invited talk**)

4. Qiang Wu, Jianghong Yao, Chunling Zhang, Jiwei Qi, Chongpei Pan, Fuhua Yang, Jingjun Xu, “Interaction of femtosecond laser with crystal materials - from THz chip to hyperdoped photodetector”, China-Poland Bilateral Seminar on Semiconductor Materials and Devices, Beijing, China, Dec. 13-15 (2020). (**Invited talk**)

5. Jiaping Wu, Baohui Li*, “Multicompartment aggregates from self-assembly of miktoarm star quaterpolymers in a dilute solution: A simulation study”, 2020 International workshop on Soft Matter and Biophysics Theories, Oct. 13 (2020). (**Invited talk**, Online)

6. Z. Chen, “Dirac-like photonic structures: from pseudospin to topology”, 19th International Conference Laser Optics, “R8: Nonlinear Photonics: Fundamentals and Applications”., ICLO 2020, Nov. 2-6 (2020). (online)

7. Z. Chen, “Nonlinear self-guiding of light in biological suspensions”, 19th International Conference Laser Optics, “R10: Nonlinear and Quantum Integrated Optics”, ICLO 2020, Nov 2-6 (2020). (online)

8. Z. Chen, L. Tang, “Design and demonstration of photonic flat-band lattices for light localization”, Photonics North, Canada, May (2020). (online)

9. Shiqi Xia, Nan Wang, Daria Smirnova, Lev Smirnov, Liqin Tang, Daohong Song, Alexander Szameit, Daniel Leykam, Zhigang Chen, “Demonstration of nonlinearity-induced coupling to topological edge and interface states”, Conference on Lasers and Electro-Optics, San Jose, US, May 10-15 (2020). (online)

10. Xiuying Liu, Zhixuan Dai, Daohong Song, Zhiming Zhang, Shiqi Xia, Liqin Tang, Hrvoje Buljan, Jingjun Xu, Zhigang Chen, “Two-dimensional Zitterbewegung analog in symmetry-breaking photonic honeycomb lattices”, Conference on Lasers and Electro-Optics, San Jose, US, May 10-15 (2020). (online)

11. Xiuying Liu, Shiqi Xia, Ema Jajtić, Daohong Song, Denghui Li, Liqin Tang, Daniel Leykam, Jingjun Xu, Hrvoje Buljan, Zhigang Chen, “Universal conversion of topological singularities from momentum to real space”, Conference on Lasers and Electro-Optics, San Jose, US, May 10-15 (2020). (online)

12 Jina Ma, Jun-Won Rhim, Liqin Tang, Shiqi Xia, Haiping Wang, Xiuyan Zheng, Shiqiang Xia, Daohong Song, Yi Hu, Yigang Li, Bohm-Jung Yang, Daniel Leykam, Zhigang Chen, “Observation of non-contractible loop states in a photonic Kagome lattice of Corbino-geometry”, Conference on Lasers and Electro-Optics, San Jose, US, May 10-15 (2020). (online)

13 Marouen Chemingui, Xiao Song, Xiaorong Li, Xinyuan Zhang, Qiang Wu, Xinzheng Zhang, Irena Drevensek-Olenik, Jingjun Xu, “Fabrication of two-dimensional microstructure to achieve topological liquid crystals patterns”, IEEE Photonics Conference 2020, Vancouver, Canada Sep. 28 - Oct. 1 (2020). (online)

14 Pengbo Jia, Zhili Li, Yi Hu, Zhigang Chen, Jingjun Xu, “Mapping a nonlinear response to a wave profile”, Conference on Lasers and Electro-Optics, San Jose, US, May 10-15 (2020). (online)

15 Wenrong Qi, Jie Zhou, Lingjun Kong, Chenghou Tu, Yongnan Li, Adάn Cabello, Jingling Chen, Huitian Wang, “Stronger quantum contextuality”, Conference on Lasers and Electro-Optics (CLEO) 2020, Washington, May 9-14 (2020). (Poster);

16 G. L. Zhang, C. Tu, Y. Li, and H. T. Wang, “Generation of arbitrary longitudinal polarized optical field under tight focusing condition”, Conference on Lasers and Electro-Optics, Washington, May 9-14 (2020). (Poster)

17 潘雷霆，“纳微尺度细胞成像与操控”，第四届光学青年科家论坛，宁波（2020.12.4-7）（**邀请报告**）

18 蔡卫，“等离激元超分辨成像与应用”，2020 年“极端光学”研究生暑期学校，上海（2020.7.13-14）**(邀请报告)**

19 王钰，李晓荣，高少华，杨东浩，王佳艺，崔慧林，Marouen Chemingui，张心正*，许京军，“区域液晶面外定向技术及其在光场调控中的应用”，第十九届全国基础光学与光物理学术讨论会，长春（2020.12.18-21）（**邀请报告**）

20 任梦昕，“非线性铌酸锂超构表面”，光学前沿在线，线上报告（2020.09.25-27）（**邀请报告**）

21 吴强，贾子熙，进晓荣，黄松，姚江宏，杨富华，许京军，“飞秒激光过饱和掺杂硅的高性能单元探测器、柔性光电探测器、单晶材料”，第十五届全国激光技术与光电子学学术会议，上海（2020.10.17-20）（**邀请报告**）

22 吴强，贾子熙，进晓荣，黄松，姚江宏，杨富华，许京军，“飞秒激光过饱和掺杂硅的高性能单元探测器、柔性光电探测器、单晶材料”，第十四届全国硅基光电子材料及器件研讨会，镇江（2020.9.25-26）（**邀请报告**）

23 吴强，姚江宏，张春玲，齐继伟，潘崇佩，杨富华，许京军，“飞秒激光与晶体的瞬态相互作用——太赫兹光芯片与过饱和掺杂光电探测器”，第十七届“中国光谷”国际光电子博览会暨论坛，武汉（2020.11.11-13）（**邀请报告**）

24 吴强，姚江宏，张春玲，齐继伟，潘崇佩，杨富华，许京军，“铌酸锂芯片上的太赫兹集成和超时空分辨成像”，第四届超快激光精密加工技术及应用研讨会，杭州

（2020.12.17-19）（**邀请报告**）

25 薄方，“周期极化 LNOI 微腔中的非线性光学效应”，第二十四届全国激光学术会议暨十五届全国激光技术与光电子学学术会议，上海（2020.10.17-20）（**邀请报告**）

26 薄方，“周期极化铌酸锂回音廊模式光学微腔”，2020 年先进光子学与光子技术论坛，西安（2020.11.20-22）（**邀请报告**）

27 薄方，“周期极化 LNOI 微腔：制备与谐波产生”，第二届全国光子技术论坛，广州（2020.11.27-30）（**邀请报告**）

28 薄方，“铌酸锂微纳光子学若干进展”，首届“四季青”青年论坛，北京（2020.12.18-20）（**邀请报告**）

29 薄方，“周期极化 LNOI 微盘腔的制备及非线性光学应用”，第四届集成光量子信息技术青年学术论坛，北京（2020.12.18-20）（**邀请报告**）

30 张国权，王晓杰，焦跃健，邵震，薄方，许京军，“铌酸锂晶体的纳米畴结构”，光学前沿在线：微纳光子学会议（2020）（中国激光杂志举办），线上会议（2020.9.25-26）（**邀请报告**）

31 武莉，陈慧敏，白宇星，“自还原体系中的缺陷与发光”，第十二届全国光学青年学术论坛，保定（2020.11.7-9）**(邀请报告)**

32 付学文，Chunguang Jing，June Lau，Yimei Zhu，“基于射频脉冲电子发生器的新型 4D 超快透射电子显微镜及其应用”，中国电子显微学会 2020 年学术年会，成都（2020.11.22-25）**(邀请报告)**

33 付学文，Yimei Zhu，“4D 超快电子显微镜”，时空相干电子源关键科学问题与前沿技术香山学术会议，北京（2020.12.8-9）**(邀请报告)**

34 胡禹俊，李宝会*，“对非手性嵌段共聚物自组装形成的螺旋结构的手性和股数调控的模拟研究”，第四届高分子科学与工程国际研讨会—先进高分子及复合材料高端论坛，北京（2020.12.11-13）（**邀请报告**）

35 涂成厚，“基于偏振调控的光场新特性与应用”，第二十四届全国激光学术会议暨第十五届全国激光技术与光电子学学术会议(LTO)，上海（2020.10.17-20）（**邀请报告**）

36 李勇男，“空间结构光场调控及应用”，第五届原子分子物理与光物理研讨会，济南（2020.10.16-18）（**邀请报告**）

37 宋锋，LMN 2020 世界激光制造大会暨第十四届中国（深圳）激光与智能装备、光电技术博览会, 深圳（2020.10.12-14）（**邀请报告**）

38 张平，康倩倩，裴雨苗，王兆远，胡毅，陈志刚，许京军，“拉比振荡中的手性效应”，第十二届全国光学青年论坛会议，保定（2020.11.6-8）

39 胡毅，“非线性加速光的调控与应用”，第四届光学青年科学家论坛，宁波（2020.12.4-7）

40 宋道红，“Universal momentum-to-real-space mapping of topological singularities”，第十二届全国光学青年学术论坛，保定（2020.11.6-8）

41 韩小芳，李彩芬，胡月，李记伟，高峰*，张文定，董校，许京军，“一种新型可调谐光

纤内马赫曾德干涉仪”，第四届光学青年科学家论坛，宁波（2020.12.4-7）

42 李占成，刘文玮，谢博阳，程化，陈树琪，田建国，“手性人工微结构波场调控物理及其应用”，多层次手性物质的精准构筑重大研究计划 2019 年度学术交流会，成都（2020.10.26-29）

43 刘文玮，李占成，谢博阳，程化，陈树琪，田建国，“电介质超构表面光场调控及应用”，第五届全国原子分子物理与光物理学术研讨会，济南（2020.10.16-18）

44 王烁琳，单益东，郑大怀，刘宏德，孔勇发，刘士国，许京军，“铋锌，铋铟，铋锆双掺铌酸锂晶体的光折变性能及其机制研究”，第二届人工晶体材料青年学术会议，宜兴（2020.11.21-23）（优秀研究生论文奖）

45 孙军，刘士国，李清连，喻彬，郝永鑫，张中正，赵晨成，第二届人工晶体材料青年学术会议，宜兴（2020.11.20-23）

46 王瑞，颜欣龙，杨帆，“YAG:Yb 晶体闪烁发光与辐照损伤的模型与测试”，第二届人工晶体材料青年学术会议，宜兴（2020.11.20-23）

47 颜欣龙，王瑞，杨帆，“锂基中子探测闪烁共晶的生长与性能研究”，第二届人工晶体材料青年学术会议，宜兴（2020.11.20-23）

48 潘雷霆，“基于 STORM 超分辨成像技术的巨噬细胞伪足小体基质降解功能及调控的研究”，第八届细胞结构与功能的信号基础研讨会，泰安（2020.10.29-11.2）（张贴报告）

49 王钰，高少华，杨东浩，李晓荣，王佳艺，崔慧林，Marouen Chemingui，张心正*，许京军，“手性材料与手性纳米结构中的光传输矩阵计算方法”，第十九届全国基础光学与光物理学术讨论会，长春（2020.12.18-21）（张贴报告）

50 韩小芳，高峰*，张文定，董校，张国权，许京军，“一种实用的全光纤可调谐上下话路耦合器”，第四届光学青年科学家论坛，宁波（2020.12.4-7）（张贴报告）

学术组织与期刊任职/Academic Service

国内外学术组织任职/Service to the Professional Societies

序号	姓名	任职机构	职位	任期
1	陈树琪	天津市优秀创新创业导师人才库	创新导师	2018-
2	陈树琪	中国超材料学会	理事	2019-
3	董校	中国化学学会高压化学分会（筹）	委员	2020.1-
4	孔勇发	教育部大学物理课程教学指导委员会大学物理实验专委会	委员	2019-2024
5	孔勇发	全国高校实验物理教学研究会	副理事长	2018-2022
6	孔勇发	全国硅酸盐学会人工晶体生长与材料专业委员会	理事	
7	潘雷霆	中国光学学会生物医学光子学专业委员会	青年委员	2015.12-2020.12
8	潘雷霆	中国微循环学会微循环与血液治疗专业委员会	常委	2017.12-2021.12
9	宋峰	固体激光技术重点实验室	学术委员	五年
10	宋峰	教育部大学物理教学指导委员会	委员	五年
11	孙军	国家标准化管理委员会-人工晶体标准化技术委员会	委员	2012.9-
12	孙军	国家新材料测试评价平台先进无机非金属材料行业中心	理事	2019.1-
13	孙军	国家新材料测试评价平台先进无机非金属材料行业中心	技术专家	2019.1-
14	孙军	河南省电子陶瓷材料与应用重点实验室	学术委员会委员	2019.1-
15	孙军	南阳师范学院	兼职教授	2019.5-
16	孙军	无机非金属材料河南工程实验室学术委员会	委员	2018.4-
17	孙军	中国兵工学会激光技术专业委员会	委员	2018.9-
18	孙军	中国材料与试验团体标准委员会光电材料及产品领域委员会	委员	2018.11-
19	孙军	中国材料与试验团体标准委员会光学晶体标委会	副主任委员	2018.12-
20	孙军	中国材料与试验团体标准委员会建筑材料领域人工晶体技术标委会	副主任委员	2018.8-
21	孙军	中国硅酸盐学会晶体生长与材料分会	理事	2018.07-

序号	姓名	任职机构	职位	任期
22	孙　军	中科院上海光机所	客座研究员	2019.1-2022.1
23	王　斌	天津市物联网开发与应用协会	副会长	2021.12.31
24	吴　强	天津市物理学会	副秘书长、常务理事、光学与光电子委员会主任	2017-
25	武　莉	国际粉末衍射数据中心	会员	2010.03-
26	武　莉	中国材料研究会青年工作委员会	理事	2014.12-2017.12
27	武　莉	中国物理学会 X 射线衍射专业委员会	委员	2019.10-
28	徐晓轩	中国仪器仪表协会近红外专业委员会	委员	2021.12.31
29	徐晓轩	中国仪器仪表协会物理光学仪器专业委员会	委员	2021.12.31
30	杨　帆	IEEE	会员	2012-
31	杨　帆	国家新材料测试评价平台稀土行业中心	理事；技术专家	2020.1-
32	杨　帆	中国材料研究会青年工作委员会	理事	2017.10-
33	杨　帆	中国材料与试验团体标准委员会光电材料及产品领域委员会光电检测标准化技术委员会	委员	2019.3-
34	张国权	美国光学学会	Senior Member	2013-
35	张国权	天津市物理学会	常务副理事长	2019-
36	张国权	中国光学学会	理事	2017-
37	张国权	中国物理学会	理事	2019-
38	张心正	天津市光学学会	常务理事	2015-
39	张心正	天津市激光技术学会	理事	2015-
40	陈树琪	天津市优秀创新创业导师人才库	创新导师	2018-

国内外期刊任职/Service to the Journals

序号	姓名	任职机构	职位	任期
1	陈树琪	American Journal of Optics and Photonics	Editorial Board	2017-
2	陈树琪	Scientific Reports	Editorial Board	2018-
3	陈树琪	光学学报	编委	2019-2021
4	陈树琪	光学学报	Topic Editor	2017-
5	陈树琪	红外与激光工程	青年编委	2020-
6	陈树琪	物理	编委	2020-2023
7	陈树琪	中国激光杂志社	青年编委常务委员	2017-
8	陈志刚	Advances in Physics: X	Founding Editorial	2015-

序号	姓名	任职机构	职位	任期
			Board/ Editor	
9	陈志刚	Frontiers in Photonics	Founding Editorial Board/Associate Editor	2020-
10	陈志刚	Light Science & Applications	Guest Editor	2019-2020
11	陈志刚	Optics Letters	Topical Editor	2014-2020
12	陈志刚	Scientific Reports	Editorial Board Member	2015-
13	胡　毅	Frontiers Photonics	Review Editor	2020.10-
14	孔勇发	激光技术	编委	2019－2022
15	孔勇发	人工晶体学报	编委	2019-2023
16	李宝会	Europhysics Letters	Co-Editor	2015-
17	宋　峰	大学物理	副主编	五年
18	宋　峰	光电技术应用	编委	五年
19	宋　峰	激光杂志	编委	五年
20	宋　峰	物理与工程	编委	五年
21	孙　军	人工晶体学报编委会	委员	2019.4-2022.3
22	孙　军	现代电子技术	编委	2017.07-
23	孙　军	中国稀土学会稀土晶体专委会	委员	2019.4-
24	吴　强	Scientific Reports	Member of Editorial Board	2013-
25	吴　强	激光与光电子进展	编委	2019-
26	吴　强	中国激光杂志社	青年编委	2017-
27	杨　帆	人工晶体学报	青年编委	2019.11-
28	张国权	激光技术	编委	2006-
29	张心正	激光技术	编委	2015-

博士后情况

序号	姓名	性别	年龄	合作导师	在站时间
1	李占成	男	29	陈树琪	2018.7.23-
2	朱俊达	男	28	薄　方	2018.7.23-
3	Sudipta Kumar Bera	男	34	陈志刚	2019.4.2-
4	郝振中	男	29	薄　方	2019.7.16-
5	谢博阳	男	28	陈树琪	2019.7.16-
6	张　博	男	33	刘智波	2019.7.27-
7	Bongiovanni Domenico	男	39	陈志刚	2019.8.26-
8	Marouen	男	32	张心正	2019.9.29-
9	张路	女	31	张国权	2020.6-
10	张跃变	男	27	陈树琪	2020.6-
11	刘建基	男	31	张国权	2020.6-

序号	姓名	性别	年龄	合作导师	在站时间
12	吴佳坪	女	29	李宝会	2020.6-
13	苏宝旺	男	29	刘智波	2020.6-
14	邢福临	男	28	许京军	2020.7-
15	刘文玮	男	29	陈树琪	2020.7-
16	耿慧芳	女	32	付学文	2020.10-

获奖情况/Awards & Honors

获奖教师/Award for excellent teachers

天津市科学技术进步奖一等奖：

获奖名称：高温多变量复杂生产体系节能减排理论方法与关键技术应用研究
证书日期：2020.10.19
完 成 人：徐晓轩（排名第五）

2020 宝钢教育奖：

2020 宝钢优秀教师奖
获奖人：余华

获奖学生/Award for excellent students

南开大学首届唐立新奖学金：夏士齐

天津市创新创业奖学金：夏士齐

中国光学学会优秀博士学位论文提名奖：刘文玮

第十六届王大珩光学奖高校学生奖：谢博阳

研究生国家奖学金：贾鹏博 张 平 刘秀英 夏士齐 王 楠 王子范

南开大学公能一等奖学金:
刘 洋 胡晓洋 黄 松 进晓荣 马军军 陈嘉鑫 于殿强 赵大平 裴维维 夏士齐
刘秀英 燕文超 高晓莉 梁亦豪 白宇星 钟 阳 张 利 董皓天 玛地娜 王 珂

南开大学公能二等奖学金:
王佳怡 卢 瑶 李志轩 熊 浩 张令龙 张 迪 李三兵 刘甲琛 周冬旭 文虹镜
郝永鑫 何新玲

研究生公能三等奖学金:
祝志茂 王 钰 杨东浩 李晓荣 崔慧林 王 琳 张馨元 冷 荣 曹力元 张 妮
杨娓茹 樊 江 齐嘉琳 黄 荣 孙治国 靳一鸣 杨建宇 祝东兰 刘俊芳 董 浩
侯梦迪 莫旻斐 李梦羽 刘 畅 范春慧 陈相宇 张 莉 张月颖 张文杰 刘时康
牛彬雯

研究生专项奖学金:
徐西坦 周 旭 刘俊芳 杨东浩 赵大平 马军军 胡 月 杨 晨 刘甲琛 张月颖
王 敏

南开大学“三好”学生：刘俊芳 胡 月 夏士齐 刘秀英 燕文超

南开大学优秀学生干部：赵大平　徐西坦　王　敏

南开大学优秀共产党员：张煜晨　王　敏

物理学院优秀志愿者：刘甲琛

OSA (Optical Society) presentation fee grant, Conference on Lasers and Electro-Optics (CLEO 2020)：卢瑶

第四届超快激光精密加工技术及应用研讨会学术报告奖：刘瑶瑶

第二届人工晶体材料青年学术会议“优秀研究生论文”奖：王烁琳　颜欣龙

学位论文/Dissertations

1. 博士学位论文 Dissertation for Doctoral Degree

[1] 陈慧敏，具备自还原性质的磷酸盐基力致发光材料的研究；导师：武莉

[2] 付钰婷，镱铥共掺的氟氧化物玻璃陶瓷上转换荧光和非接触式光学温度传感特性的研究；导师：赵丽娟

[3] 高晓梅，基于光学微腔的矢量光场发射器研究；导师：薄方

[4] 郭宇翱，Er^{3+}/Yb^{3+}共掺氟氧化物玻璃陶瓷上转换荧光热敏特性中若干关键问题研究；导师：赵丽娟

[5] 贾子熙，飞秒激光过饱和掺杂硅及其光电探测器的研究；导师：吴强

[6] 焦跃健，铌酸锂纳米畴结构的制备及其性能研究；导师：张国权

[7] 李丽，铝表面等离激元共振腔的阴极荧光光谱研究；导师：蔡卫

[8] 李文灿，基于 Si 衬底的铌酸锂薄膜及其整流特性研究；导师：孔勇发

[9] 李小宽，二维材料异质结及其掺杂研究；导师：臧维平、刘智波

[10] 李致力，自加速脉冲的非线性传输调控与应用；导师：胡毅

[11] 李智，超表面线性和非线性光场调控研究；导师：田建国、陈树琪

[12] 刘芳，二维过渡金属硫族化合物的超快光学非线性和载流子弛豫过程的研究；导师：陈璟、鄢小卿

[13] 刘建基，基于腔增强自发参量下转换制备超窄线宽纠缠光子源；导师：张国权

[14] 马继娜，Kagome 光子晶格中非传统平带态和锥形衍射的研究；导师：宋道红

[15] 裴雨苗，光子晶格中负质量驱动的学类比研究；导师：陈志刚、胡毅

[16] 齐文荣，光子轨道角动量和几何相位在量子光学中的应用；导师：王慧田、李勇男

[17] 苏宝旺，二维材料半导体异质结构光电性质的研究；导师：田建国、刘智波

[18] 王海平，光束整形及其在光镊中的应用；导师：陈志刚

[19] 王日德，基于铌酸锂集成平台的太赫兹功能器件研究；导师；姚江宏、吴强

[20] 王维维，铌酸锂缺陷结构的第一性原理研究；导师：孔勇发

[21] 王周祥，阶跃型少模光纤中轨道角动量传输特性及其在螺旋成像中的应用；导师：王慧田，李勇男

[22] 吴佳坪，不同链拓扑结构的嵌段共聚物在熔体/溶液中的自组装行为的模拟研究；导师：李宝会

[23] 邢福临，基于光刻图案化技术的细胞间通讯研究；导师：许京军、潘雷霆

[24] 徐晓丹，基于二维材料的光电器件制备与特性研究；导师：张心正

[25] 张景雪，链结构对受限于两平行板间的对称嵌段共聚物的相行为以及均聚物溶液在界面上的贫化现象的影响；导师：李宝会

[26] 张路，基于经典光场的空域超聚束效应及其应用；导师：张国权

[27] 张跃变，基于人工微结构的平面光学研究及应用；导师：田建国、陈树琪

[28] 赵梦丹，矢量光场与分形及其在信息传输中的应用；导师：王慧田、涂成厚

2. 硕士学位论文 DissertationforMasterDegree

[1] 安亚文，基于二阶姜-泰勒效应的新型无机化合物晶体的制备、结构与表征；导师：孙同庆

[2] 薄莹雷，不同晶面 Bi2WO6 和 BiOBr 光催化还原 CO_2 生成 CO 的研究；导师：曹亚安

[3] 边达民，均聚物链在溶液中的构象转变行为模拟研究；导师：李宝会

[4] 曹博弢，光纤矢量模式耦合微腔回音廊模式的调控及应用；导师：高峰

[5] 曹翰，$LaMnO_3$ 和 $NaNbO_3$ 基光催化剂能带结构的调控和光还原 CO_2 的活性研究；导师：孔勇发

[6] 车颖，基于硅纳米结构的饱和非线性散射应用于 STED 超分辨成像研究；导师：徐晓轩

[7] 陈桂林，铝/硼酸盐基发光材料的缺陷调控及性能优化；导师：武莉

[8] 董瑞，磷酸盐基光致、力致复合功能晶态材料的制备及性质；导师：武莉

[9] 范友静，锌锆双掺铌酸锂晶体的室温倍频性能研究；导师：孔勇发、刘宏德

[10] 弓楠，基于二维材料范德瓦尔斯异质结的研究；导师：禹宣伊、张心正

[11] 郭丽娟，基于铌酸锂微环腔孤子频梳的研究；导师：李勇男

[12] 何慧霞，钒酸盐(XVO_4, X = Bi、Gd、Ce、Y 和 In)光催化剂的制备和光还原 CO_2 生成 CH_4 的研究；导师：曹亚安

[13] 胡慧敏，Zn/Ca 离子掺杂 $Na(Y/Lu)F_4$ 上转换发光材料的制备、发光和温度特性研究；导师：宋峰

[14] 胡梦媛，掺钒铌酸锂晶体的第一性原理研究；导师：孔勇发

[15] 化梦梦，三英寸 X 轴铌酸锂晶体生长的研究；导师：孙军、张玲

[16] 黄露露，基于各向异性克尔介质的飞秒矢量光场可控成丝研究；导师：涂成厚

[17] 康倩倩，光子晶格中的非线性拍频研究；导师：张玲、胡毅

[18] 李彩芬，超声波调制光纤布拉格光栅的光谱及应用；导师：高峰

[19] 李金泽，时域整形飞秒激光微纳加工晶体材料的研究；导师：吴强

[20] 李羽，艾里等离激元调制电子波前的研究；导师：蔡卫

[21] 梁丹丹，铌酸锂晶体的平放肩生长研究；导师：张玲、孙军

[22] 梁菁，MXene（Ti_3C_2）二维材料的制备、表征及应用；导师：徐晓轩

[23] 刘锦锦，温度诱导多相态 $KGdF_4$ 晶体形成机制分析；导师：余华

[24] 刘雪婷，对称星型两亲三嵌段共聚物薄膜自组装行为的模拟退火研究；导师：李宝会

[25] 邵震，铌酸锂晶体薄膜中铁电畴的稳定性研究；导师：张国权

[26] 宋筱，二维液晶图案的制备及应用；导师：张心正

[27] 孙文倩，双嵌段共聚物与均聚物三元共混体系自组装行为以及硬球链均聚物的模拟研究；导师：李宝会

[28] 台玉可，钠硼化合物的结构预测及实验合成；导师：周向锋

[29] 汪海军，新型无机硝酸盐、亚硒酸盐化合物晶体的制备、结构与表征；导师：孙同

庆

[30] 王楠，两种光子晶格中拓扑相关物理现象的研究；导师：陈志刚

[31] 王晓，基于位移相位的偏振调控超表面研究；导师：程化

[32] 王俞萱，飞秒激光改性宽禁带半导体氧化锌的研究；导师：吴强

[33] 蔚莹琪，基于铌酸锂微腔的中红外光学频率梳研究；导师：李勇男

[34] 吴佳琦，动态及可重构超表面光场调控；导师：陈树琪

[35] 武兵，面向生物应用的稀土掺杂纳米晶上转换发光温度传感特性研究；导师：赵丽娟

[36] 谢俊芳，基于椭偏仪测量的 $PtSe_2$ 光学性质研究；导师：田建国、鄢小卿

[37] 谢语晨，少模光纤的声致光栅传感器研究；导师：李勇男

[38] 张海涵，飞秒激光极化铌酸锂晶体的研究；导师：李勇男

[39] 张洪爽，基于二氧化钛超表面的偏振态调控研究；导师：涂成厚

[40] 张平，基于超分辨成像技术的巨噬细胞伪足小体基质降解功能及调控的研究；导师：潘雷霆、李任植

[41] 赵雅丽，基于 STORM 超分辨成像技术的乳腺癌细胞膜蛋白 PD-L1 组织分布特性及其调控的研究；导师：潘雷霆

[42] 赵艺，两嵌段共聚物薄膜自组装多孔形态的模拟研究；导师：李宝会

[43] 郑忠忠，锗酸盐基力致发光材料的探索；导师：武莉

[44] 朱梦红，二维富硼磁性材料的第一性原理研究；导师：周向锋

[45] 朱砚涵，基于 STORM 超分辨成像技术的 Hela 细胞膜蛋白 CD47 组织分布特性及调控的研究；导师：潘雷霆